COMPUTATIONAL AND EXPERIMENTAL MODELING OF FLUID FLOW AND HEAT TRANSFER PROCESSES IN COMPLEX GEOMETRIES
Sylvana Verónica Varela Ballesta

Dipòsit Legal: T. 284-2012

Sylvana Verónica Varela Ballesta

Computational and Experimental Modeling of Fluid Flow and Heat Transfer Processes in Complex Geometries

Doctoral Thesis

Supervised by

Dr. Anton Vernet
Dr. Josep Anton Ferrè

Department of Mechanical Engineering

UNIVERSITAT ROVIRA I VIRGILI

Tarragona, 2012

Departament d'Enginyeria Mecànica
Escola Tècnica Superior d'Enginyeria Química
Universitat Rovira i Virgili
Av. Països Catalans, 26
43007 Tarragona
Tel. 977 55 96 02
Fax 977 55 96 91

Dr. J.A. Ferrè and Dr. Anton Vernet, respectively Professor and Associate Professor in the Mechanical Engineering Department of Universitat Rovira i Virgili,

CERTIFY :

That the present study, entitled :

Computational and Experimental Modeling of Fluid Flow and Heat Transfer Processes in Complex Geometries

presented by MSc. Sylvana Varela for the award of the degree of Doctor, has been developed under our supervision at the Department of Mechanical Engineering of this university and it is fully adequate in scope and quality as a dissertation for the degree of Doctor of Philosophy.

And, to inform you of that and in order for it to have the needed effects, we sign this certification.

Tarragona, February 2012

Dr. Josep Anton Ferrè   Dr. Anton Vernet

A mi familia,
a Juan y a Pili
y a todos aquellos que me han ayudado a ser quien soy.

ii

Abstract

The main objective of this work is the numerical and experimental study of the velocity and temperature fields in complex domains like those encountered in computers or other electronic refrigerated systems with printed circuit board (PCB). Cooling is one of the main challenges these devices have to deal with. Heat removal from the electronic circuit devices has become an important issue to take into account during their design. PCB's are electronic circuits that generate heat by Joule effect and need to be cooled down. They are becoming smaller and therefore some warming problems appear that lowers their efficiency and lifespan. The study of the velocity and temperature fields is closely connected with the analysis of the spatial and temporal evolution of the flow structures found in PCB enclosed cavities and with the understanding of the influence of the geometry, the inlet fluid velocity and plate temperature in the cooling process of the PCB.

In this work all this items have been analyzed by means of numerical simulation and experimental analysis. The first has been done employing the numerical method *caffa3d* [1] that uses, a spatial discretization based on block-structured, non-orthogonal body fitted grids solves the $3D$ incompressible Navier-Stokes equation inside PCB enclosures. Numerical simulations for two different PCB geometry configurations are analyzed using Reynolds numbers from 100 to 10000.

The experimental part of the work has been done with Particle Image Velocimetry (PIV). This technique is used to acquire the experimental velocity field in a simplified model of a PCB. Experimental results have been obtained for three Reynolds numbers, considering three different plate temperature configurations (no temperature difference between the plate and the fluid, a temperature differences of $\Delta T = 10°$ C and $\Delta T = 30°$ C). In order to simultaneously analyze two parallel planes in the PCB, a method to generate and record at the same time two polarized light planes has been implemented. PIV analysis technique is applied separately to each plane to obtain two simultaneous velocity fields. Consecutive measurements, in which only the distance between laser sheets is

changed, allow to observe space and time evolution of the dynamic structures of the flow.

In the top sections for both geometrical configurations, the dynamic field shows flow structures such as a pair of quasi-symmetric counter-rotating vortices while at the bottom sections the flow behavior depends on the geometry. In the closed geometry the pair of quasi-symmetric counter-rotating vortices remains instead in the open geometry those structures disappear giving way to smaller ones. Being these results verified for both experimental and numerically techniques. The existence of a recirculation region beneath the plate at the entrance of the bottom channel obtained previously [1] for the open geometry was verified.

The temperature field is practically the same above the plate encasing the PCB, differences appear below the plate. While analyzing the plane just below for the open geometry the main consideration is the presence of a hot zone. The results obtained indicate that the cooling of the PCB is more efficient for the closed geometry. Small changes in the PCB geometry modify the velocity flow field allowing the formation of new vortical structures in the bottom channel of the PCB that enhance the heat transfer between the fluid and the plate. A deeper knowledge of the behavior of these structures can lead to a better enclosure design that can perform more effective heat dissipation in the PCBs.

Agradecimientos

La presente tesis doctoral ha sido llevada a cabo en el grupo de investigación Experiments, Computation and Modelization in Fluid Mechanics and Turbulence (ECoMMFiT), de la Escola Técnica Superior d'Enginyeria Química, de la Universitat Rovira i Virgili de Tarragona, bajo la dirección conjunta de los Drs. Anton Vernet y Josep Anton Ferrè.

A Anton Vernet por su comprensión, su ayuda, sus comentarios y consejos enriquecedores a nivel académico y personal. Por su paciencia y su siempre presente buen humor.

A Josep Anton Ferrè por su confianza, por sus siempre acertados comentarios y su buen humor.

A Gabriel Usera por haberme dado la posibilidad de acercarme a la simulación numérica, por su infinita paciencia y contención.

A mis compañeros de departamento, tanto veteranos como noveles, Roland Blanch, Salvatore Cito, Manuel Martí, Guillaume Novelli, Sylvana Tourn, Yolanda Cuenca, George Abdelmassih, Irene Sancho, David Santiago, Javier Burgos, Albert Puig.

A Jordi Polo le agradezco especialemente todo el apoyo técnico que me a brindado durante estos años y las horas compartidas en el laboratorio.

A mis amigos, los de toda la vida y los nuevos, a Jimena Guirado, Nicolás Casaballe, Jovana Vilches, Carlos Bergero, Itala Arias y Julia Perez, a todos muchas gracias de corazón, saben que los amo.

A Juan por acompañarme en este viaje y lo que es más importante, por acompañarme en la vida. A Pili por todas sus sonrisas y los juegos compartidos.

A mi madre, a mi abuela y a todos los que estan ausentes transitória o definitivamente porque es increíble hasta donde se puede llegar cuando existen personas que creen en uno de forma incondicional. A todos los que no confían y dudan siempre de mí por hacer que me cuestione más profundamente mis objetivos.

la Dirección General de Investigación del Ministerio de Ciencia e Innovación y fondos FEDER.

Por último, quiero agradecer a los miembros del tribunal, los Drs. Roberto Castilla, Josep Ramón Gonzáles e Ildefonso Cuesta, y a todos aquellos que directa o indirectamente han contibuído en la relización de esta tesis.

List of Publications and Contributions to Conferences

Journal papers

- S. Varela, G. Usera, A. Vernet , J.A. Ferré. "Numerical simulation of flow structures and temperature distribution in a Printed Circuit Board enclosure model at moderate Reynolds numbers". In press in International Journal of Thermal Sciences.
DOI: http://dx.doi.org/10.1016/j.ijthermalsci.2011.09.011

International congress presentations

- S. Varela, G. Usera, A. Vernet, J.A. Ferre. "Enfriamiento en modelos de cavidades que contienen PCB: Estudio numérico", Oral Presentation, XI Reunión sobre Recientes Avances en Física de Fluidos y sus Aplicaciones, Fluidos 2010, November 2010, Colonia , Uruguay.

- S. Varela, A. Vernet, J.A. Ferre. "Flow structures in PCB enclose model: Experimental study", Oral Presentation, 5th Workshop on Research in Turbulence and Transition, ERCOFTAC, October 2010, Tarragona, Spain.

- S. Varela, G. Usera, A. Vernet, J.A. Ferre. "Numerical Simulation of the Flow Structures in a Print Circuit Board enclosure model", Oral Presentation, 7th International Conference on Heat Transfer, Fluid Mechanics and Thermodynamics, HEFAT, July 2010, Antalya, Turkey.

- S. Varela, G. Usera, A. Vernet, J.A. Ferre. "Cooling of Print Circuit Board enclosure model: Numerical study", Oral Presentation, 6th International Conference on Diffusion in Solids and Liquids: Mass Transfer, Heat Transfer and Microstructure and Properties, DSL2010, July 2010, Paris, France.

- S. Varela, G. Usera, A. Vernet, J.A. Ferre. "Velocity and temperature evolution in PCB enclosure model", Oral Presentation, European Research Community On Flow, Turbulence And Combustion, ERCOFTAC, October 2009, Lisbon, Portugal.

- S. Varela, G. Usera, A. Vernet, J.A. Ferre. "Structural models of PCB-containing cavities: temporal and spatial evolution," Oral Presentation, Congress of Numerical Methods in Engineering 2009, July 2009. Barcelona, Spain.

- S. Varela, A. Vernet, J.A. Ferre. "Flow structures in PCB enclose model: Time and spatial evolution", Oral Presentation, 14th International Symposium on Applications of Laser Techniques to Fluid Mechanics, July 2008, Lisbon, Portugal.

General Index

GENERAL INDEX

Figure Index

FIGURE INDEX

FIGURE INDEX

FIGURE INDEX

Tables Index

TABLES INDEX

Chapter 1

Introduction

Nowadays, electronic circuit devices can be found everywhere around us. Print-ed circuit boards (PCB) are an essential part of computers, audio and video devices, automobiles or airplanes, and also in less common applications as diverse elements of spacecrafts and telecommunication satellites. Cooling is one of the main challenges these devices have to deal with. Heat removal from the electronic circuit devices has become an important issue to take into account during their design. PCB's are electronic circuits that generate heat by Joule effect and need to be cooled down, usually done by air (Fig. 1.1). This is a problem of fluid flow in complex domain where we can find the coexistence of laminar and turbulent fluid regions and heat transfer effects by natural/forced convection, conduction and radiation. A good review of the available convection options for cooling electronic equipment can be found in Incropera [2]. Difficulty grows by the fact that there is a trend to reduce the size of the PCB enclosures to fit the needs of the manufacturers. This increases the warming problems and is the cause of a reduction of the PCB's efficiency and lifespan. Several studies can be found among literature dealing with the analysis of heat transfer characteristics of 2D and 3D arrays of regular heated blocks as the ones developed by Asako et al. [3], Fushinobu et al. [4] or Jubran et al. [5]. There is also a lot of work done on conjugate heat transfer problems where convection and conduction occurs simultaneously (i.e. Heindel et al. [6]). In general, a large number of experimental and numerical fluid flow analysis in complex domains can be found in the literature. One example is Chiang et al. [7] that made the heat transfer analysis taking into consideration heat-generating components like a central processing unit (CPU), hard disk (HDD) and adaptive cards in different locations in a 3D desktop computer with two side-wall fans. They used the CFD program PHOENICS to simulate the thermal behavior inside an enclosure at three Reynolds numbers for four different cooling fans placements. Concluding that, the thermal behavior of the ventilated enclosure depended on the geometric configuration of the heat sources and the cooling fans.
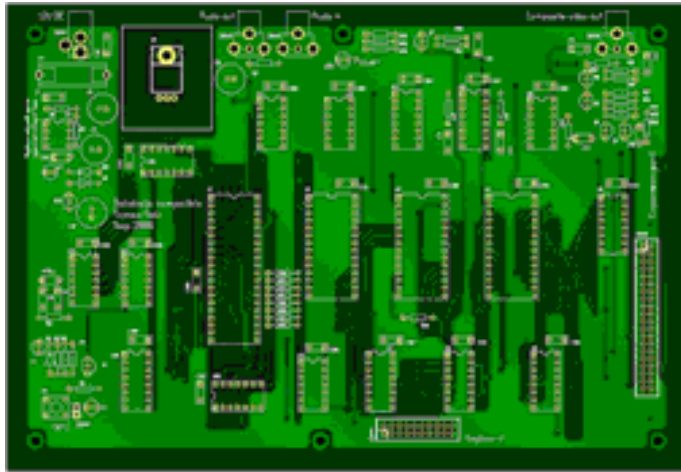
Figure 1.1: Computer motherboard is an example of Print Circuit Boards. (PCB)

On the other hand, it is possible to find specific software to design the cavities for PCBs. Protocase Designer [8] is commercial software that specifically deals with the cavity design. ESTIMA [9] is another software package developed for numerical prediction of the coupled electrical and thermal fields in a PCB with active electrical or electronic components. It includes the modeling of the conduction heat transfer through an heterogeneous solid (board and tracks) with temperature dependent physical properties, the modeling of the electrical field, submitted to local differences in resistivity and also to heterogeneities (tracks, solders and jumpers), and the thermal modeling of electrical (fuses, relays) and electronic (solid state relays) components.

Despite all these works, very few are focused in the relationship between the fluid flow structures inside the housing and their effect in the heat transfer process needed for the cooling of PCB's. Usera et al. [1] have used both experimental and numerical techniques for determining the velocity field in a cavity with PCB's. They analyze a model of PCB enclosure with a single entrance of refrigeration fluid and one fluid out in an opposite location. PCB is modeled as a single plate located in the plane of symmetry of the housing. These studies show the existence of an alternate vortex shedding that can be considered important for the heat transfer process. The main objective of this work is to analyze the spatial and temporal evolution of the flow structures found in PCB enclosed cavities to understand the influence of the geometry in the cooling process. The large scale structures present will affect the heat transfer between the PCB and the fluid and can be responsible of the production of "hot spots" which generate local mechanical wear. The overall aim of the ongoing research is to investigate how small changes in the shape of the PCB can modify the

2

velocity field and in consequence the temperature distribution on its surface. In this work the results at different Reynolds numbers will be analyzed and compared for two PCB configurations for constant physical properties. Cases with temperature dependent physical properties were checked too. A deeper understanding of flow structures and temperature field distribution can lead to a better enclosure design, improving heat dissipation of the PCBs.

1.1 Backgrounds

This work could be considered a continuation of two previous works on PCB made in ECOMMFIT group. Initially the concern for solving problems of heat removal from electronic circuit devices was addressed through software ESTIMA. The numerical prediction of the coupled electrical and thermal fields in a PCB with active electrical or electronic is made by this software.
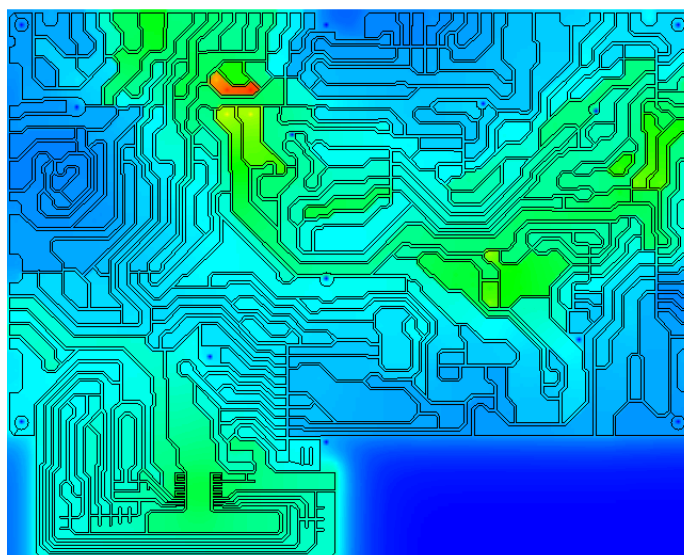
Figure 1.2: Visualization of thermal field [9].

The conduction heat transfer through an heterogeneous solid with temperature dependent physical properties, the electrical and the thermal field (Fig. 1.2) of electrical (fuses, relays) and electronic (solid state relays) components are modeled with this software. In ESTIMA the electric field is computed on a uniform 2D mesh while the thermal field is computed in a 3D mesh, using finite-diffenrence/finite-volume approaches respectively. Different interfaces have been considered, like the substrate-track, the substrate-pin and the substrate-hole and can simulate single or double-sided PCB's with pins or variable length jumpers. ESTIMA has also a specific user-friendly interface that

allows the user to perform the operations involved in the definition of the board and the computation of the resulting fields. The predictable capability of ES-TIMA have been evaluated by Lear R&D department and the tendencies and quantitative values shown fairly good agreement even for extreme operating conditions. It is important to note that ESTIMA's predicted fields are local and the PCB, in many cases, are located in a junction box [9]. In the automotive industry high power PCB's coexist with electronic boards in progressively smaller junction boxes (Fig. 1.3).
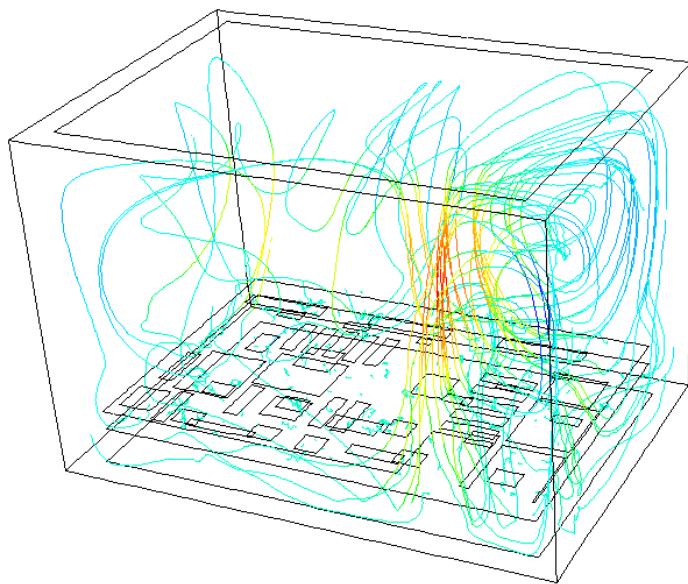
Figure 1.3: Example of 3D streamlines in a junction box.

In this sense, the next step was to study the temperature distribution and flow field in a junction box. These step have been done by Usera et al. [1]. Large-structures of the turbulent flow have been analyzed experimental and numerically. One of the most common methods to measure the velocity field of fluids using digital image processing is the digital particle image velocimetry (DPIV). This method has the advantage of being non-intrusive, indirect and very accurate determining the flow velocity field. Experimental DPIV data have been used to validated the in house flow solver caffa3d.MB. The PCB enclosure is a rectangular box with a single entrance of refrigeration fluid an one fluid out in an opposite location. The PCB is modeled as a single homogenous plate shorter than the box length. Tracks, solder and jumpers are not considered. Experimental data was compared with numerical data obtained with a grid made of five regular blocks of resolution $h/40$. A single value of Reynolds number was chose to make the comparisons.

1.2   Problem Statement

A schematic representation of the PCB system considered in this study is shown in Fig. 1.4**a**. The system consists of a rectangular box with two square section openings of side $h = 0.024$ m working as inlet and outlet for the circulating fluid.
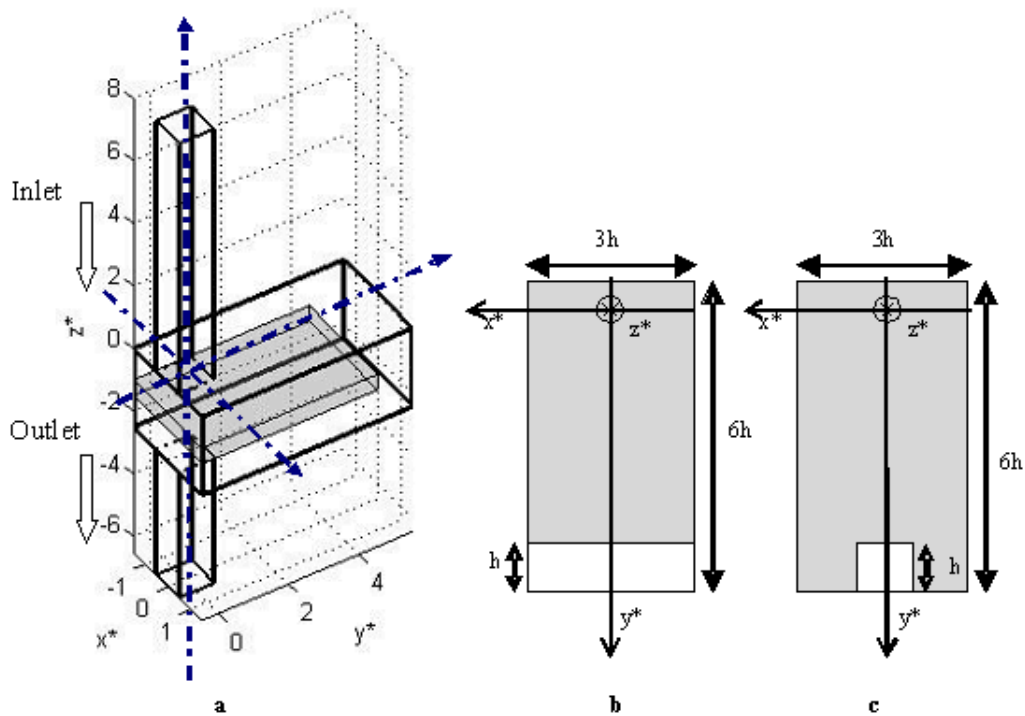
Figure 1.4: Model's sketch, **a** three dimensional view, **b** and **c** Top view of the two studied models.

The flow entrance's cavity is carried out trough a square base block of $h \times h$ and $8h$ long, outlet block has the same base dimensions and $4h$ long. The inlet block is longer than the outlet one to minimize perturbations. The size of the housing is $6h \times 3h \times 2.5h$ with a central plate simulating the PCB placed in the plane of symmetry of the box. Two different geometries of this central plate are analyzed. The first one is a rectangular prism $3h$ wide, $0.5h$ high and $5h$ long that was studied before by [1]. The second case corresponds to a rectangular prism $3h$ wide, $0.5h$ high and $6h$ long with an $h \times h$ opening. In this configuration, the junction box model can be considered as the sum of two channels, the top and the bottom ones with size of $6h$ long, $3h$ wide and h tall. To help differentiate among configurations we refer to the first one (Fig. 1.4**b**) as the open geometry and the second (Fig. 1.4**c**) as the closed geometry.

The PCB system has been studied experimentally using PIV techniques and numerical using the solver *caffa3d.MB* [1]. In the following chapters, the

5

experimental setup and domain-based numerical scheme presented 1.4**a** will be explained.

1.3   Objectives

The main objective of this work is to analyze the spatial and temporal evolution of the flow structures found in PCB enclosed cavities to understand the influence of the geometry, the inlet fluid velocity and plate temperature in the cooling process of the PCB. To accomplish this objective the listed task bellow need to be followed:

- Analyze the flow structures in a printed circuit box enclosure model

- Establish the effect of the variation in the fluid velocity at the entrance of the enclosure in the flow structures

- Study the impact of the variation on the PCB geometry in the flow structures present in the enclosure

- Analysis the influence of the PCB's temperature in the flow structures

- Investigation of how the flow structures affect the refrigeration process of a heated PCB model, including changes in velocity and geometry.

- Adjustment of the existing experimental enclosure model for its use with a heated PCB model.

- Design of the experimental setup to work with heated PCB model

- Improvements of the PIV software to analyze the images obtained

- Development of post-processing software to analyze the velocity and temperature fields obtained form experimental and numerical simulations.

- Implementation of a PIV multi plane method to generate and record two parallel planes with polarized light in order to estimate the space and time correlation of the flow structures

- Use of the caffa3d software to simulate the flow in the PCB enclosure.

- Generate the numerical grids and specify the initial and contour conditions for the simulations

- Analyze the effect of considering constant/non constant physical properties in the caffa3d software

- Comparing numerical and experimental results for equal working conditions

Chapter 2

Fundamentals of Digital Particle Image Velocimetry

In recent years several methods have been developed to measure the velocity field of fluids using digital image processing. One of the most common methods is the digital particle image velocimetry (DPIV). This method has the advantage of being non-intrusive, indirect and very accurate determining the flow velocity field. The method was developed by Adrian in 1988 [17] and generalized in the following years, among others, by Westerweel [18], [19], [21]. The experimental set-up of a DPIV system consists in illumining the fluid region to be studied with a thin laser sheet and capturing two consecutive images by a digital camera.

In order to allow the fluid visualization, particles with similar density have to be added to the flow, these particles called tracers follow the movement of the fluid without disturbing it. Tracers have a random distribution, generating what is called a tracer's pattern. The light scattered by the particles is recorded on a camera, thus generating a set of images separated by an interval of time Δt. As it is shown in the schematical arrangement present in Fig. 2.1. An important condition for achieving optimal implementation of the technique is that the time between two successive images have to be short enough so that the tracers appearing in an image also appear in the next, and long enough, to appreciate the particles movement.

The implementation of DPIV standard algorithms are based on statistical methods [20], either autocorrelation or cross correlation between two consecutive images, allowing to estimate the relative displacement of the particles. For this purpose each image is divided into subdivisions called interrogation windows (W) and assume that all particles within W move uniformly during the period of time between each image.

The essential problem of the standard algorithm arises from the cross-correlation of two interrogation windows with the fixed size and position. The standard algorithm provides relatively reasonable velocity vectors; however,
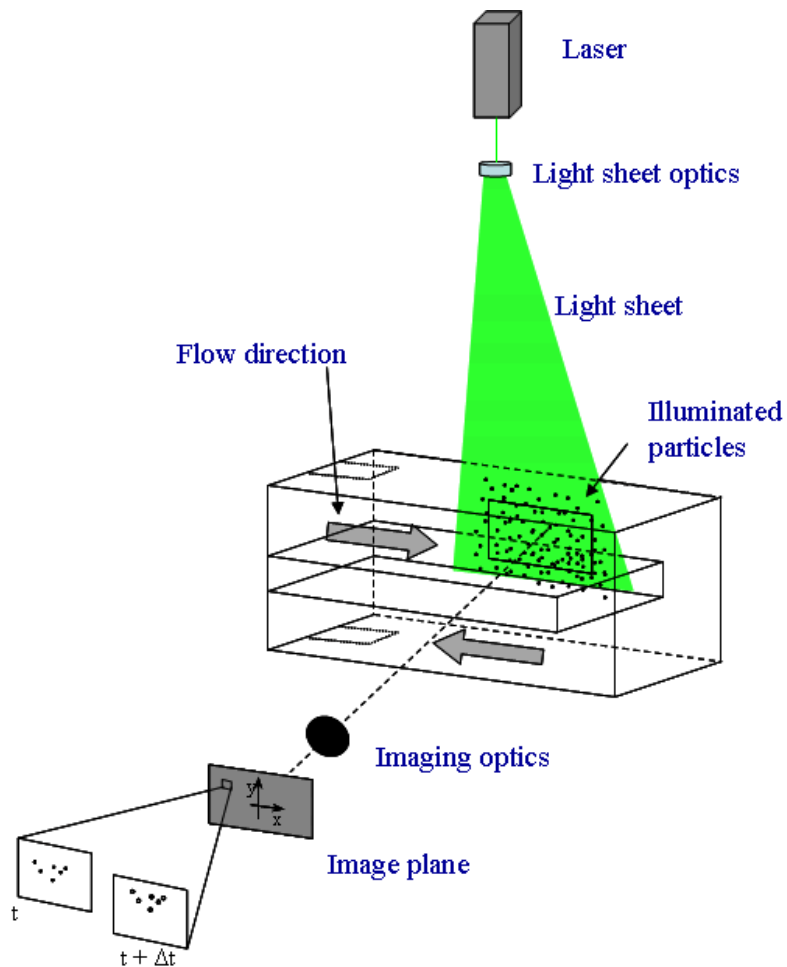
Figure 2.1: Schematic arrangement for particle image velocimetry.

its accuracy becomes deteriorated and sometimes produces error vectors due to the losses of many particle pairs in a complex flow region.

To resolve flow structures much smaller than the interrogation windows the Local Field Correction Particle Image Velocimetry (LFCPIV) has been employed [22]. This method has a remarkable capability for accurately resolving small scale structures in the flow, down to a few times the mean distance between particles.

2.1   PIV basic principles

Before introducing the cross-correlation method in the evaluation of a PIV image, the task should be defined from the point of view of image processing. First of all, a pair of images containing particle images has been recorded from a light sheet. The second image is recorded a short time later, during which the particles will have moved according to the underlying flow. Given this pair of images, the objective is to measure the straight-line displacement of the particles. The image pair can yield a field of linear displacement vectors where each vector is formed by analyzing the movement of localized groups of particles. In practice this is accomplished by extracting small samples or interrogation windows and analyzing them statistically (Fig. 2.2).
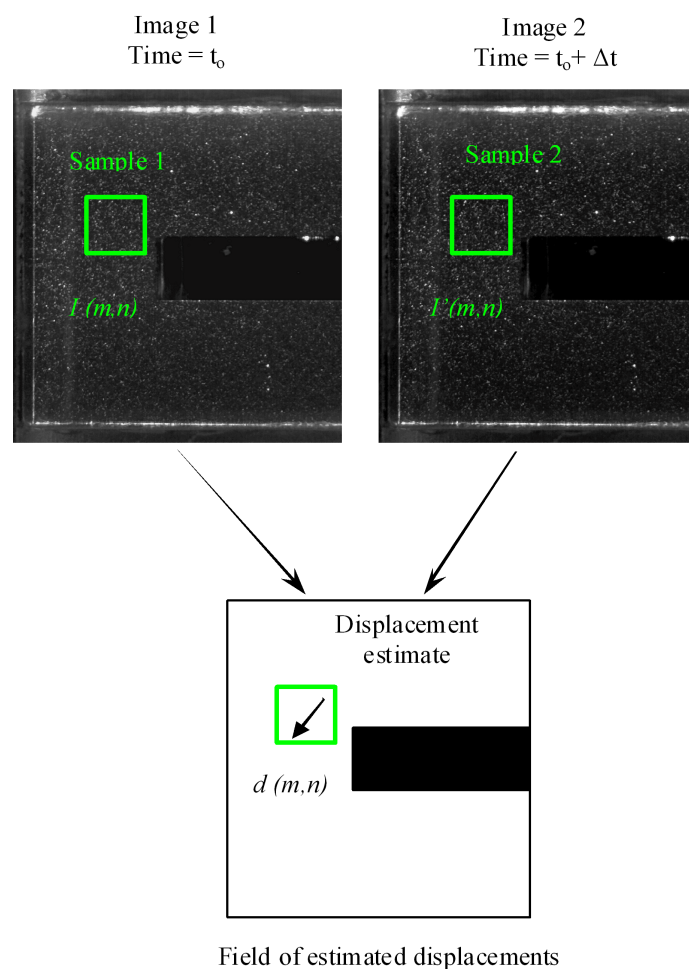
Figure 2.2: Conceptual arrangement of frame-to-frame image sampling associated with double frame/single exposure PIV.

With both images I and I' known the aim is to estimate the displacement field. The fact that the images are not continuous, the dark background cannot provide any displacement information, makes it necessary to estimate the displacement function using a statistical approach base on interrogation windows. Rather than estimating the displacement function analytically the methods of choice is to locally find the best match between the images in a statistical sense. This is accomplished through the use of the discrete cross-correlation function,

$$R_{II}(x,y) = \sum_{i=-K}^{K} \sum_{j=-L}^{L} I(i,j)I'(i+x,j+y) \qquad (2.1.1)$$

The variables I and I' are the samples as extracted from the images where I' is larger than the template I. For each choice of sample shift (x,y), the sum of the products of all overlapping pixel intensities produces one cross-correlation value $R_{II}(x,y)$, by applying this operation for the range shifts $(-M \leqq x \leqq M, -N \leqq y \leqq N)$ a correlation plane with size $(2M+1) \times (2N+1)$ is obtained. Where M and N are limits of the window shift, in general M and N are choose equal and base-2 even though mathematically there is no restriction.

Essentially the cross-correlation function statistically measures the degree of match between the two samples for a given shift. The highest value in the correlation plane can be use as a direct estimate of the particle image displacement. Upon examination of this direct implementation of the cross-correlation function two things are evident: the number of multiplications per correlation value increases in proportion to the interrogation window area and the cross-correlation method inherently recovers linear shifts only. The direct implementation of the cross correlation function is not efficient because in a typical PIV interrogation sampling windows cover on the several thousand pixels. Thus, millions of multiplications an summations have been performed to obtain only one correlation plane. A more efficient alternative to compute the cross-correlation function is the use of the correlation theorem which states that the cross-correlation of two functions is equivalent to a complex conjugate multiplication of their Fourier transforms:

$$R_{II} \iff \hat{I} \cdot \hat{I'}^{*} \qquad (2.1.2)$$

where $\hat{I}$ and $\hat{I'}$ are the Fourier transforms of the functions I and I', respectively. The tedious two-dimensional cross-correlation process of eq. 2.1.1 can be reduced to computing two two-dimensional Fast Fourier Transforms (FFT) on equal sized samples of the image followed by a complex-conjugate multiplication of the resulting Fourier coefficients.

These are inversely Fourier transformed to produce the actual cross-correlation plane which has the same spatial dimensions, $N \times N$ as the two input sam-

10
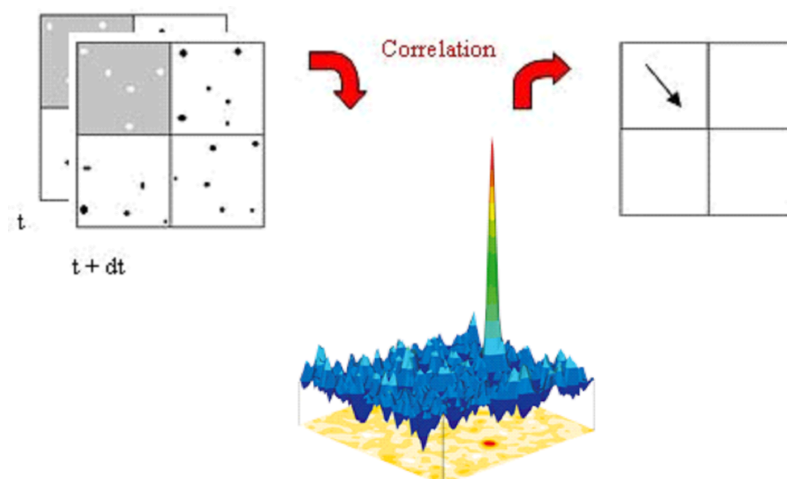
Figure 2.3: Schematic representation of the formation of the correlation plane.

ples (Fig. 2.3). The computational efficiency of this implementation can be increased further using the symmetry properties between real valued functions and their Fourier transforms. The process used in schematic representations is shown in Fig. 2.4. The FFT's computational efficiency is incremented
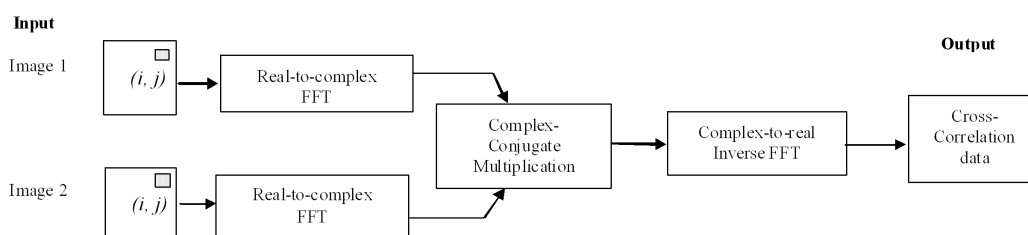
Figure 2.4: Implementation of cross-correlation using Fast Fourier Transform.

by recursively implementing a symmetry property between the even and odd coefficients of the FFT. The most common implementations require the input data have a base-2 dimension (i.e. 32×32 pixels or 64×64 pixel sample). For these reason typically interrogation window sizes range from 8 to 128 pixels depending on the size of the digital image, the seed particle size and seeding density. The subdivisions are determined by the grid spacing and interrogation window size. The grid spacing is the space between measurements in the image. For example, a grid spacing of 4 pixels means that the final output will have a velocity every 4 pixels in the image, or a 64×64 grid of velocity measurements for an image size of 256 pixels.

2.2 Advanced techniques

In this work the image processing has been made through a Matlab Program set of routines by means of simple algorithms. In brief, the program consists of one main Matlab file and several external files; all programs have been written as functions and are interdependent. This PIV Matlab package has been developed by several members of ECOMMFIT group. The main file allows obtaining the velocity field of the flow and contains many options which can be changed for the necessary conditions of the flow and the image properties. The program is open and allows new options to be added to obtain a velocity field as desired. Some of these options are related with higher methods that improve the performance and accuracy of the PIV technique. Most important methods will be explained in detail in the following sections.

2.2.1 Use of clean up mask

From the time series of PIV images the time history of the illumination at each image location or pixel is available, and its statistical properties can be analyzed. For instance, the median value of the illumination at each point provides information regarding the permanent background illumination which reveals the existence of spurious reflections, or stick to the wall particles that adversely affect the detection of the actual displacement of the particles [23]. The use of the median rather than the mean makes the procedure more robust although more costly. Figure 2.5 present a typical image which has reflections on the corners.
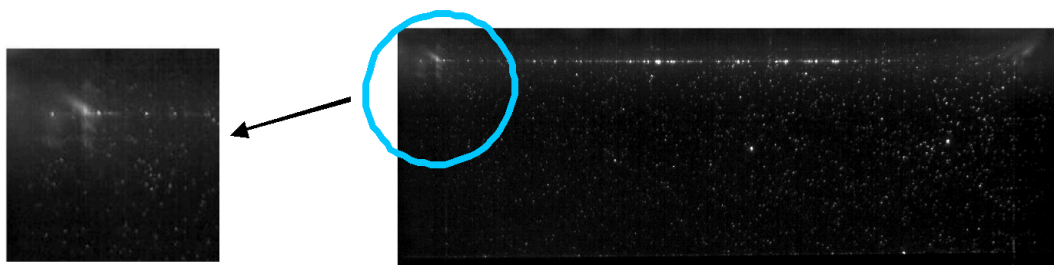
Figure 2.5: Image with reflections.

The main advantage of the procedure is to avoid spurious correlation peaks due to the presence of permanent bright spots. Rather small, distributed, permanent spots as those appearing along the upper edge are especially important to remove, since they tend to 'lock' the correlation to null displacement. Figure 2.6**a** presents a 64×64 pixels close up region of the field of view, near a corner, for one single instantaneous image. Figure 2.6**b** shows the median image from a time series of 512 images, while Figure 2.6**c** displays the difference between

Figures 2.6a and 2.6b. It can be clearly observed that the large reflection on the upper left corner has been removed.
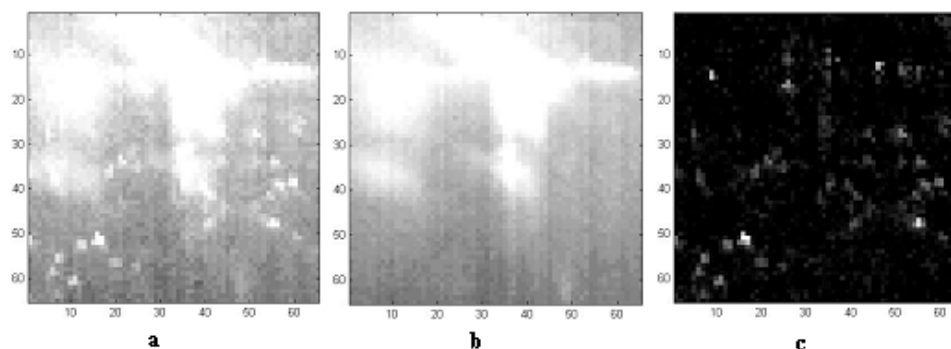
Figure 2.6: Reflections removal by median estimator across time series. **a** Original image, **b** median image, **c** difference image.

In many cases large reflections cause the saturation of areas involving several pixels, so that particle image information can not be recovered there. However, in the case where 'mild' reflections occur, not reaching the saturation level, image particle information can still be recovered by proper treatment of the local brightness histogram.

2.2.2 Triple image correlation

The loss of correlation due to out of plane displacement or other problems that operate spurious vectors can also be mitigated when dealing with well resolved time series of PIV images [23]. A time series of PIV images will be considered to be "time resolved" if the time step between measurements is smaller than the Taylor micro scale of the turbulent flow under study. Since this scale governs the initial decay of the auto-correlation, the condition implies that significant correlation exists between consecutive measurements [23].

Any given image can in principle be paired with either the next or previous image in the time series. As long as the out of plane displacement is kept smaller than half the laser sheet thickness, every particle present in one image will have its counterpart in either the next or previous image of the time series. A correlation algorithm involving the three images should prove more robust to out of plane motion than the usual single pair correlation algorithm. The algorithm used here implements this strategy by multiplying both correlation planes in order to improve the peak detection. This leads to the attenuation of the spurious correlation peaks appearing in only one of the correlation planes, while increasing the absolute height of the valid peak. The scheme for the proposed 'triple image' correlation is illustrated in Fig. 2.7.

For the image frame corresponding to time t_i in the time series, two correlation planes are obtained from the image pairs (t_{i-1}, t_i) and (t_i, t_{i+1}). These correlation planes are combined (multiplying them) into the lower correlation plane showed in Fig. 2.7, which exhibits an enhanced correlation peak. As
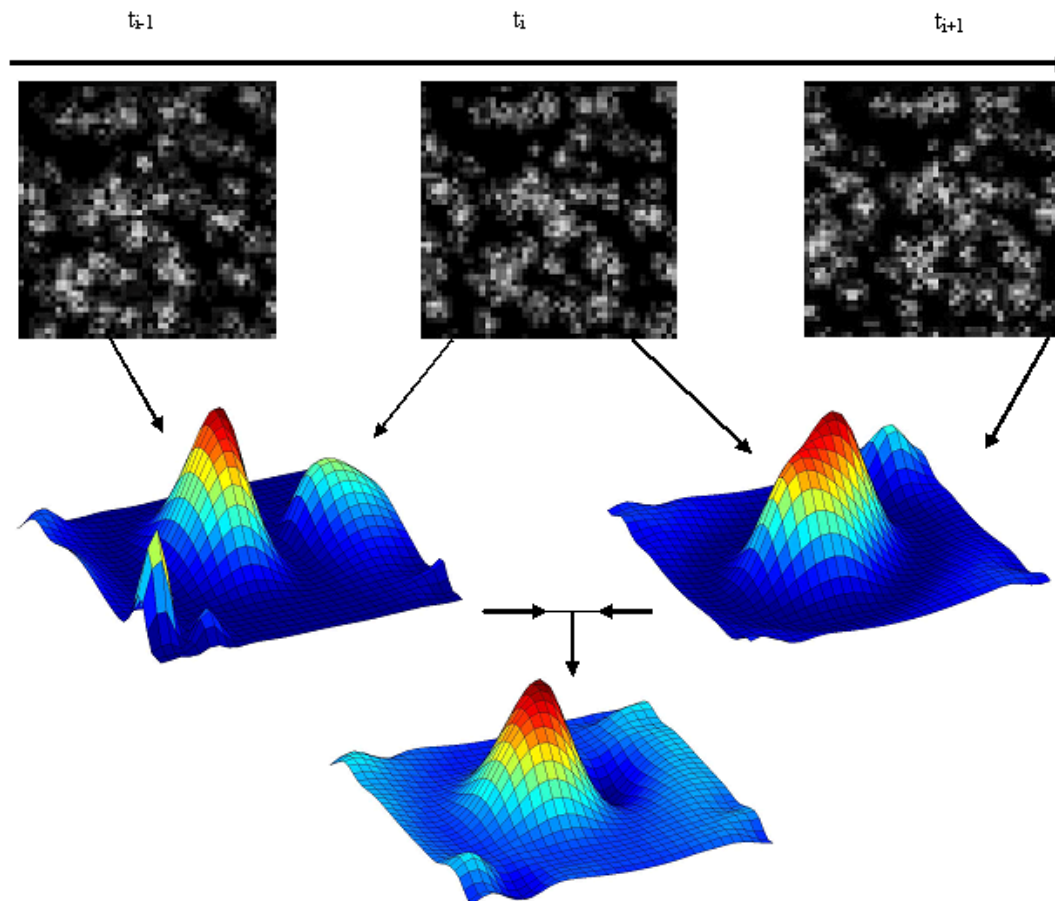
Figure 2.7: Scheme of triple image correlation and sample of correlation peak improvement.

the Fig. 2.7 shows the peak obtained from the triple correlation approach is more clearly detectable than the corresponding peaks on the standard (double) correlation planes. This is the result of the cancelation of those spurious peaks than appear in only one of the two correlation peaks, which can occasionally attain higher values leading to the erroneous estimation of the displacement of the particles.

2.2.3 Window interrogation near wall boundaries and LCF method

Another implementation used is the PIV Local Field Correction method (LFC-PIV)[22]. This method improves the final resolution and is able to resolve flow structures smaller than the interrogation window. PIV processing is done by the usual cross-correlation procedure that takes two consecutive images to compute velocity vectors at the grid nodes furthermore the triple image correlation method is applicable too. The process is iterative and the values obtained in the first iteration are corrected in consecutive step, thus, the image is redefined through compensation of the particle pattern deformation caused by the velocity gradients in the flow field.

To improve the resolution near the wall domain, a interrogation window, partially outside the domain could be selected (Fig 2.8). In this case the resulting velocity vector estimation from the interrogation process should be assigned to a point inside the PIV image, since the only valid information is provided by those pixels covered by the interrogation area that also lay within the image boundary.
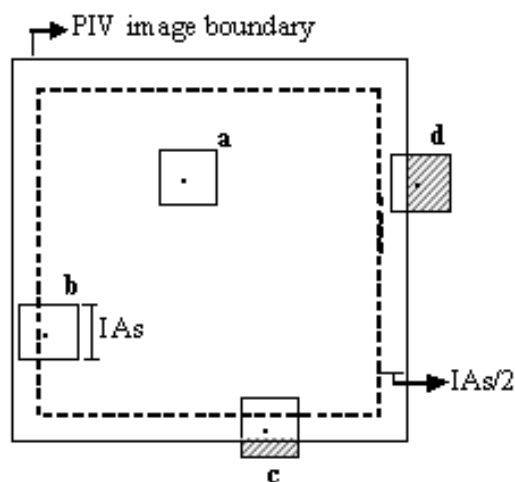
Figure 2.8: Sketch of a PIV image boundaries, and samples of inner interrogation areas (**a**, **b**) and boundary affected interrogation areas (**c**, **d**).

The geometric centre of the interrogation area is not the correct placement for the obtained velocity vector estimation. Caution must be exercised in order to correctly determine the actual location of the velocity vector estimation delivered by the interrogation process. This issue is performed using a given weighting function [25]. For inner locations, separated from the image boundary, by more than half of the interrogation area size ($IAs/2$), the
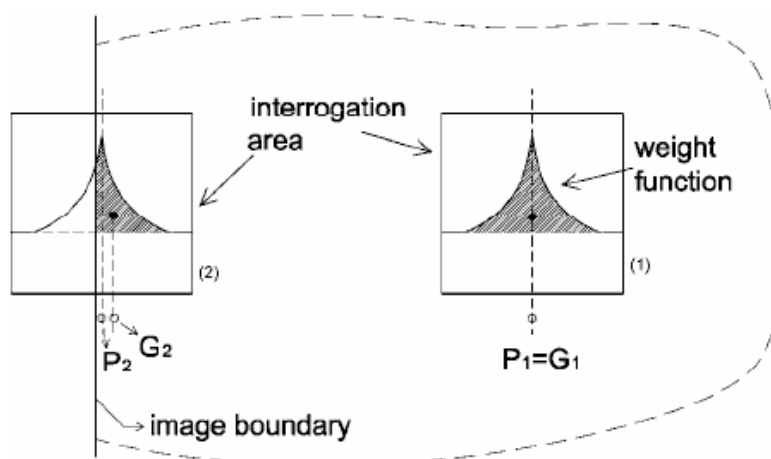
Figure 2.9: Sketch of the interrogation location displacement due to boundary cropping of the interrogation area. Figure extracted from [23].

velocity vector estimation is correctly placed at the geometric centre of the interrogation area (sections **a** and **b** in Fig. 2.8).

From Fig 2.8, the cases of interrogation areas **c** and **d** differ from the previous ones however, since they lay only partially within the image boundaries, with the shaded parts of each area being outside the image boundaries. In the case of interrogation area **d** the geometric centre has even been placed outside the PIV image. It is clear however than, even in this last case, the resulting velocity vector estimation form the interrogation process should be assigned to a point inside the PIV image, since the only valid information is provided by those pixels covered by the interrogation area that also lay within the image boundary. The geometric centre of the interrogation area is not the correct placement for the obtained velocity vector estimation in situations as those represented by cases **c** and **d**.

Thus, when the described situation occurs, caution must be exercised in order to correctly determine the actual location of the velocity vector estimation delivered by the interrogation process. The sketch of Fig. 2.9 illustrates this issue, for a given weighting function. For inner locations, separated from the image boundary, by more than half of the interrogation area size, the velocity vector estimation is correctly placed at the geometric center of the interrogation area [24]. Accordingly, the geometric center P_1 of the interrogation area coincides with the center of mass G_1 of the weighting function. However, at locations near the image boundary, the velocity vector estimation will be offset inwards due to the truncation of the weighted window. This effect can be approximated (at least at first order) by the actual placement of the center of mass G_2 of the truncated weighted window, which would be the correct placement for a simple weighted mean estimator.

16

In Fig. 2.10, result of this computation is presented for weighting function

$$\upsilon^2(\xi, \eta) = 9\left(4\left|\frac{\xi}{F}\right|^2 - 4\left|\frac{\xi}{F}\right| + 1\right)\left(4\left|\frac{\eta}{F}\right|^2 - 4\left|\frac{\eta}{F}\right| + 1\right) \qquad (2.2.1)$$

where ξ and η are coordinates with their origins at the centre of the interrogation window and F is the length of its side, proposed by Nogueira et. al [25].

The figure is referred to as 'LFC-PIV' window, and is the one for their Local Field Correction PIV method. All coordinates are given relative to the boundary, positive values corresponding to locations inside the image, while negative values correspond to points outside the image. In Fig. 2.11 a sample
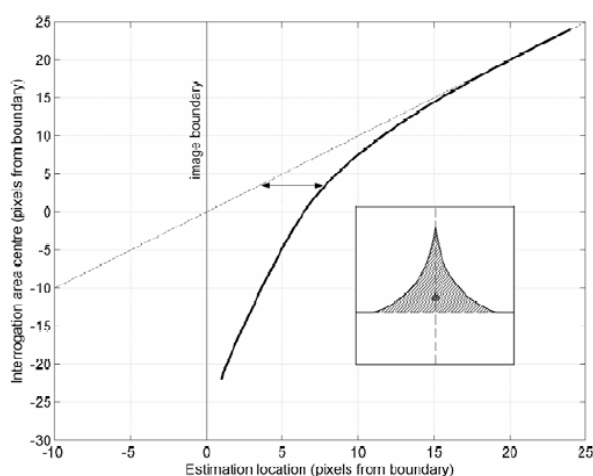
Figure 2.10: Velocity vector estimation location displacement due to boundary cropping of interrogation area. 'LFC-PIV' 48 pixels wide weighting function. Figure extracted from [24].

velocity profile is presented, with both the raw measurement and the profile compensated for the described effect, being pictured. The profile presented corresponds to a boundary layer, the wall being placed at the image boundary, and coincident with the abscissa origin. The image was processed with a 48 pixels wide 'LFC-PIV' weighting function, with an 8 pixels grid spacing. Results from a non iterative run are presented. The 'circles' line $(-o-)$ corresponds to the raw measured profile, while the 'squares' line $(-\square-)$ corresponds to the profile compensated for the estimation location displacement due to boundary cropping of the weighting function, following Fig. 2.10. The arrows indicate the corresponding points in the raw and compensated profiles, where was deemed necessary for added clarity. The first aspect to be noticed in Fig. 2.11, is that compensated estimation locations lay within the flow domain, even if the interrogation area center lies outside the flow domain, in this case to the left of the image boundary or wall at negative pixel co-ordinates.

Also, it can be seen that negligible compensation is produced for points whose distance to the wall is greater than half the weighting function width, with the interrogation area cropping due to the image boundary affecting only the points closer to the image boundary.
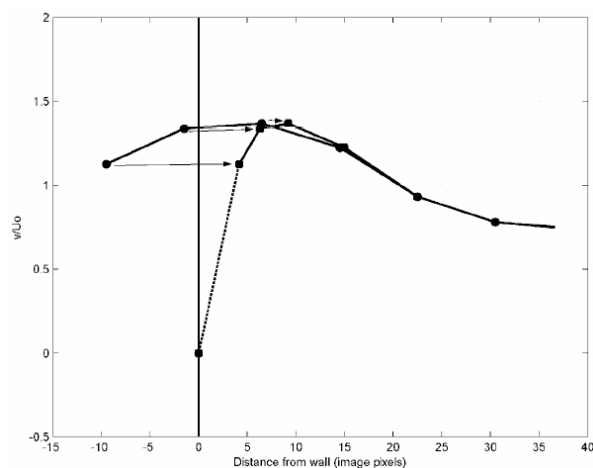
Figure 2.11: Representative profile compensation due to estimation location displacement. Raw measured profile $(-o-)$, and boundary compensated profile $(-\square-)$. Figure extracted from [24].

2.3   Multi plane measurements

In order to simultaneously analyze two parallel planes in the PCB, a method to generate and record these two planes has been implemented (Lobera et al. [26]). PIV analysis technique is applied separately to each plane to obtain two simultaneous velocity fields. Consecutive measurements, in which only the distance between laser sheets is changed, allow to observe space and time evolution of the dynamic structures of the flow.

The configuration utilized for this study consist of a single pulsed laser delivering linear polarized light, a pair of high speed cameras, three right angle prims an a pair of polarizing beam-splitter cubes (Fig. 2.12). The polarizing beam-splitter separates the incident wave in two parts. The light which passes straight forward through the cube emerges linearly polarized with the plane of the electrical field vector parallel to the plane of incidence (p- polarized). The light emerging from the cube at right angles to the incident wave front is orthogonal to the plane of incidence (s-polarized). The separation base on polarization works as long as the radius of the particles is comparable with the wavelength (Mie's Theory) [32] and the observation is properly selected to the propagation direction of the light sheet. The s-polarized light coming from the
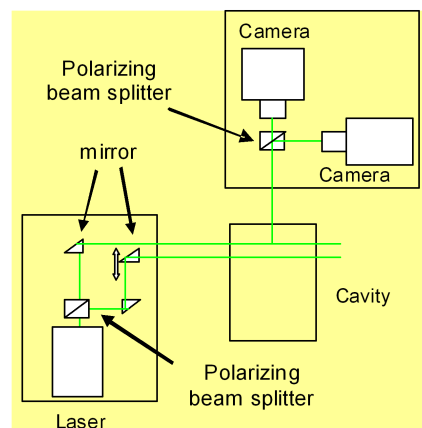
Figure 2.12: Optical set-up.

polarizing beam splitter cube pass through two right angle prims, one of them is fixed and the other can be move while the p-polarized light pass through only one prim. With is arrange two orthogonally polarized parallel laser sheet are obtained. Finally the another polarizing beam splitter is used before the light reaches the camera thus ensuring that one camera records the s-polarized light whereas the other records the p-polarized light. Multi plane PIV systems configurations using polarized light have been used by authors like Kähler and Kompenhans [33].

Chapter 3

Experimental Setup

A model of PCB enclosure (Fig. 3.1**a**) is made of in transparent plexiglas to allow optical access for the PIV measurements.

a   b
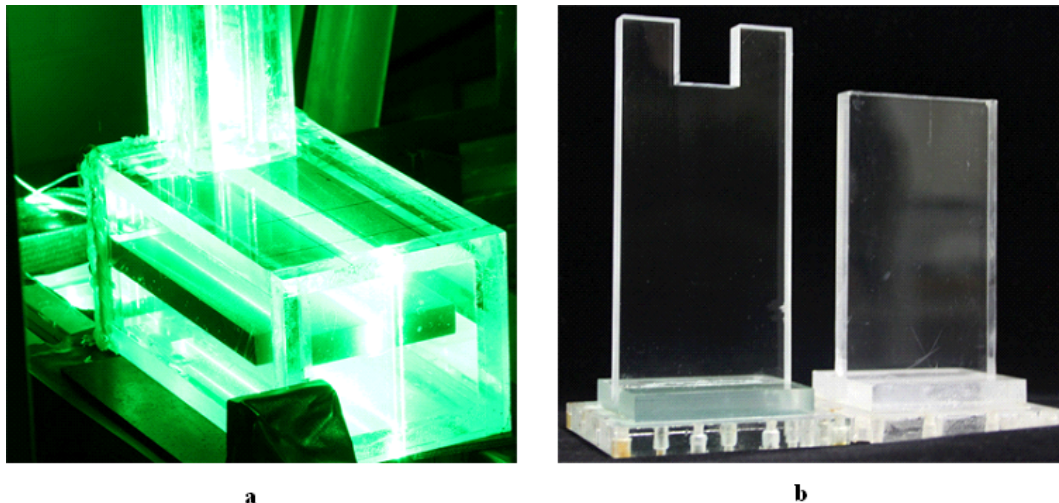
Figure 3.1: Model's photograph, **a** Cavity, **b** Geometries of this central plate.

The central plate is interchangeable, transparent methacrylate models for both geometries have been used for measurements without temperature (Fig. 3.1**b** and **c**). Temperature measurements have been made for the open geometry with a perforated aluminum plate which incorporates 3 thermocouples.

The model was operated with water as working fluid. The water circuit is gravity driven. Input fluid comes from an elevated deposit at constant height (Fig. 3.2) to minimize perturbations and ensure constant input pressure. The output is connected to a large deposit (50 l approximately) where a submerged pump drives the fluid until the elevated deposit. The system can operate at flow rates ranged within $10-2300\,l/h$. Controlling the flow rate has been done

21
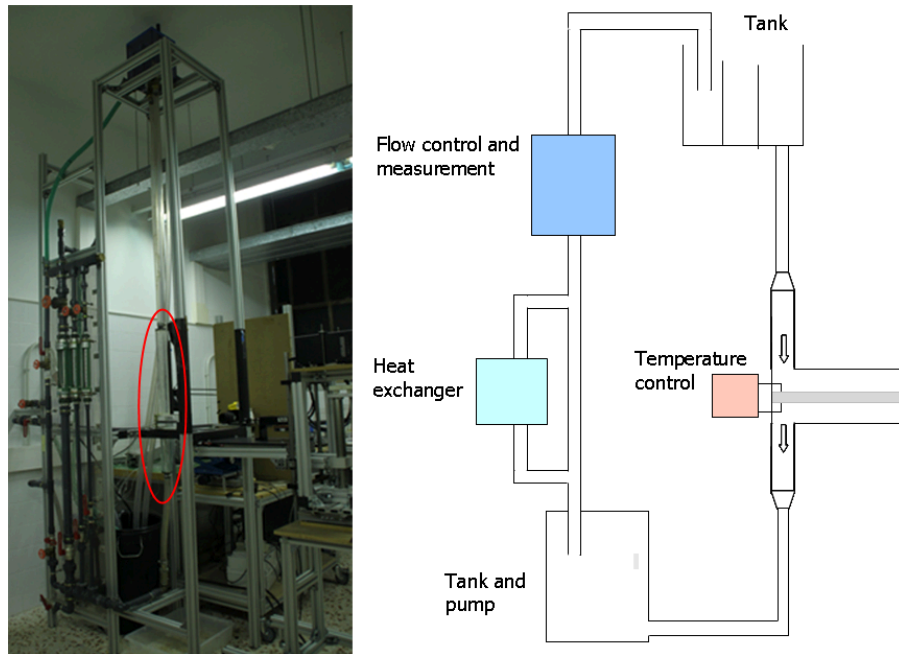
Figure 3.2: Experimental set-up, photograph and schematic representation.

by adjusting 3 rotameters of different calibers (Fig. 3.3), or the same thing, of different scales ($500 - 6000 \ l/h$, $60 - 640 \ l/h$ and $10 - 100 \ l/h$)

Figure 3.3: Rotametres to control the flow rate.

3.1 Light source and image acquisition

Two different laser models were used for illumination purposes. The use of one or the other depended on the they availability. Both are Nd: Yag semiconductor lasers, linearly polarized with 532nm wavelength.

A Monocrom DPPSL 532 pulsed with a cylindrical lens was used to generate the illumination sheet, the average power is shown in Table 3.1.

Pulse length (μs)	31	87	136	180	220
Frequency (Hz)					
10	4	5	6	9	9
100	13	29	44	54	69
150	16	39	50	66	81
200	19	50	73	115	144

Table 3.1: Average power (mW).

When this laser has been used the measures have been made at the maximum allowed power of the laser source (144 mW).

The other laser is the Monocrom MP532-3W (Fig. 3.4, it was used in continuous mode at 250 Hz. The optical system mounted on the MP532-3W
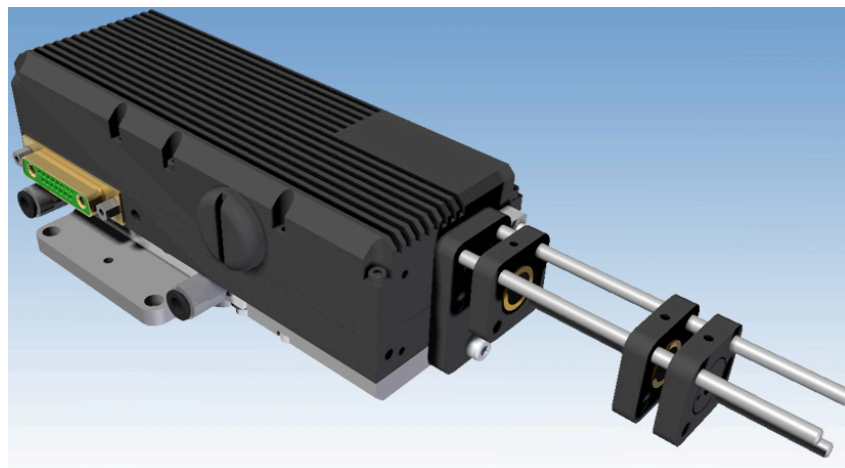
Figure 3.4: Laser sketch.

module is composed of 2 lenses beamforming and another one to generates the sheet. The laser beam before optics is in the x-axis 12 mm and y-axis 0.7 mm at output, after optics the laser beam is in the x-axis 120 mm and y-axis 0.7 mm at output. The focus length of the 2 lenses of the focus group were 10

23

mm and 25 mm while the generating sheet lens have a focus length of 5 mm. Tables 3.2 and 3.3 shows the beam and sheet characterization. The light sheet has been $1mm$ thick.

Distance(mm)	100	500	100	2000
Size (mm)	< 1	< 1	< 1	1.2

Table 3.2: Beam characterization.

Distance(mm)	100	500	100	2000
Opening (mm)	—	135	400	1000

Table 3.3: Sheet characterization.

Optical setup PIV recordings were obtained using MotionPro digital cameras, model X3 Plus and model HS.Both cameras are equipped with a 1" CMOS sensor with 1280×1024 pixels resolution with square pixels $12\mu m$. The sensitivity range is from 350 to 1000 nm (Fig. 3.5). In each camera has been placed a zoom Sigma, 28-300mm F3.5-6.3 DG Macro, which allowed us to increase specific regions.

When Monocrom DPPSL 532 has been used, both cameras were synchronized. Measurements were taken for 1684 images strips. The size of each image strip was limited by the internal memory of the cameras (4Gb) and the sampling frequency was constrained by the maximum allowed power of the laser source.

Verifying the light sheet perpendicularity with the cavity wall is very important. When light is incident on a surface, part of it is refracted and part transmitted, in our case we need to maximize the transmitted light, this will depend on the angle of incidence and refractive indices of each medium through which light travels. The transmission angle could be calculated by Snell's law:

$$n_1 sen(\theta_1) = n_2 sen(\theta_2) \tag{3.1.1}$$

where n_1 and n_2 were the refractive indices of the mediums involved, θ_1 is the angle of incidence to the surface of medium 2 when the light travels through the medium 1 and θ_2 is the angle between the beam transmitted in medium 2 with the perpendicular to the surface.

When the incidence is not normal to the surface $\theta_2 \neq 0$ then the values of the refractive indices of each media begin to take greater relevance.

The refractive indices are the system are: $n_{air} \cong 1.0$, $n_{methacrylate} \cong 1.49$, $n_{water} \cong 1.33$, where $\frac{n_{air}}{n_{methacrylate}} \cong 0.67$ y $\frac{n_{methacrylate}}{n_{water}} \cong 1.12$, in this way we
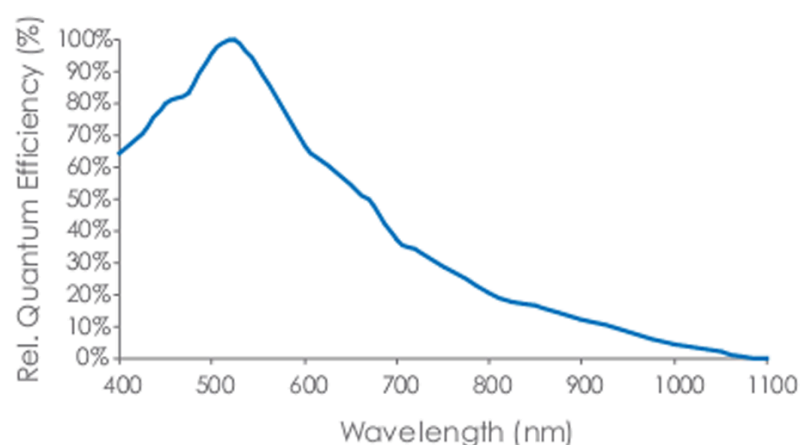
Figure 3.5: Relative spectral response.

can see that the most important interface is between air and acrylic because it's in which the angle of refraction varies more.
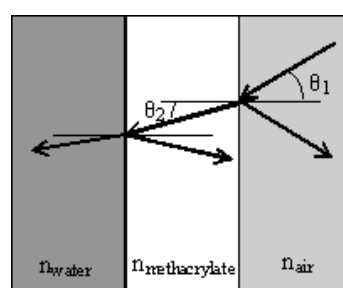
Figure 3.6: Snell law representation.

The angle θ_2 established, influence the angles in the following interfaces, hence the importance of controlling the beam interaction with the first surface.

3.2 Tracer Particles

Flow visualization techniques like PIV, needs to add some kind of tracers in order to act as markers. When these tracers are introduce in the fluid the fluid is be "seeding". Depending on the fluid solid particles, oil drops or air bubbles can used. A lot of descriptions about seeding particles and their characteristics are describe in many scientific publications but little information can be found on how to practically supply the particles into the flow. Some times the natural

seeding of the fluid is enough to apply PIV technique, for example, air bubbles presents in oil but in many cases it is desirable to add tracers in order to achieve sufficient image contrast and to control particle size. For most liquid flows this is be done by suspending solid particles into the fluid and mixing them in order to get a homogeneous distribution. Some examples of seeding particles used for the visualization in liquids flows, particularly for PIV are listed in Table 3.4, [10].

Type	Material	Mean diameter in μm
Solids	Polystyrene	10-100
	Aluminum	2-7
	Glass spheres	10-100
	Granules for synthetic coatings	10-500
Liquid	Different oils	50-500
Gaseous	Oxygen bubbles	50-1000

Table 3.4: Seeding materials for liquid flows.

In our experiments we used spores of *Lycopodium clavatum* which is a fairly common plant, especially in Europe's northern regions, characterized by low rainfall forests.

Figure 3.7: Lycopodium clavatum.

Lycopodium clavatum is a perennial climbing plant, characterized by a variable length stem covered with smooth elongated evergreen leaves (Fig. 3.7). The spores have a mean diameter around 30 μm. The are light yellow, very mobile, odorless, tasteless and buoyancy only slightly greater than water [15]. Since 1953, thanks to the austrian A. Mayr, these spores have also been used as tracers [15]. They are used in hydrography due to the characteristics before referred and also can be easily colored with food colorants [16].

In our case, the seed particles preparation was performed by mixing approximately 6 grams of particles with about 350 cc of water, and used a mixer

at $800 - 1000 rpm$ for 15 minutes. At this time floating particles were retired and mixing was continued for another 15 minutes getting a homogeneous solution. It was left to stand for 30 minutes, the smaller particles decanted, excess water was removed and the concentrate obtained was used for seeding of the 50 l water used in the experiments.

Licopodiun calvatum spores are hydrophobic so the method of particles preparation is essentially a hydration. Differences between dry and "wet" particles are shown in Fig. 3.8.
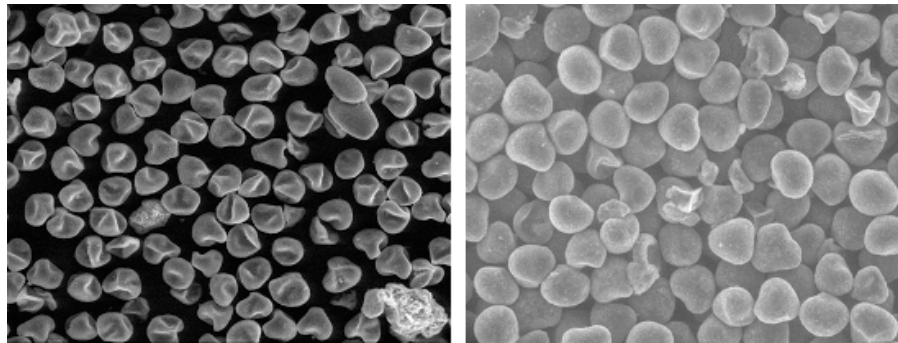
Figure 3.8: ESEM view of **a** dry (Magnification 313), **b** in solution (magnification 375) Lycopodium spores.

Figure 3.9 shows a ESEM (environmental scanning electron microscope) view of spores sample with diameters measures.
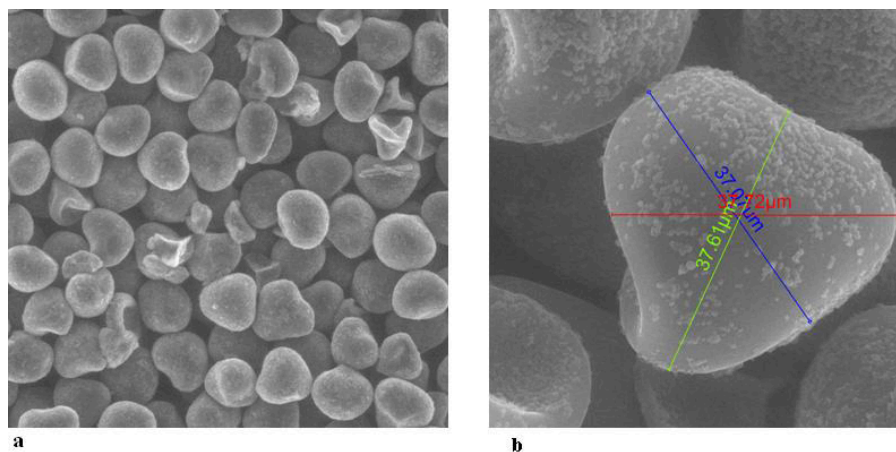
Figure 3.9: ESEM view of Lycopodium spores in solution at T = 20° and P = 5 Torr. **a** Magnification 375, **b** Magnification 2264.

3.3 Temperature control

In the experimental system, temperature control has become necessary in different senses. It was necessary to maintain water temperature at a fixed value to have certainty of the Re value. Since physical properties are involved in the determination of Re and they depends on the temperature. A submerged electric pump is used to produce the water flow in the experimental system, this is the reason because the water temperature can not be achieved only by the laboratory's temperature control. Like any mechanical engine, the pump generates heat which is transferred to the water, rising the water temperature in about 5°C when the pump is turned on for about 3 hours. To avoid this problem, a closed circuit chiller has been used (Fig. 3.10), specifically the PolyScience 6106 whose temperature range is from -10° C to 40°C [14].
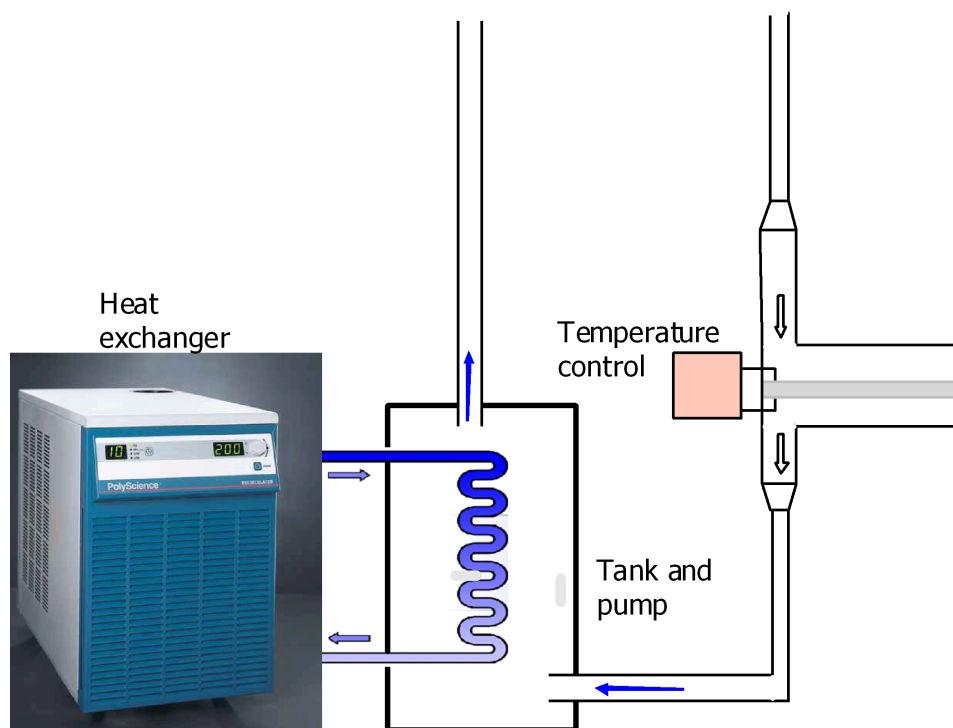
Figure 3.10: Schematic representation of the temperature control system.

A typical experimental session takes about 3 hours since measurements are made in at least four different planes in the top and bottom sections of the cavity, giving eight configurations for each flow rate. In every configurations should be align or the lighting system or the optical system. For example, for each measure plane, the laser must be aligned, verifying both upright beam position and its perpendicularity with the cavity wall. Next, the optical system has to be adjusted, placing a scale on the beam position for setting the zoom

and the focus. For finally it is necessary to positioning the optical system to visualize the desired section of the cavity.

As a some percentage of the particles used as tracers decanted when the fluid is at rest is advisable to keep the pump on during the entire experimental session thus ensuring that the images have a similar particle density. So while the image acquisition takes only a few seconds the process of system's adjustment and alignment takes several minutes for each configuration.
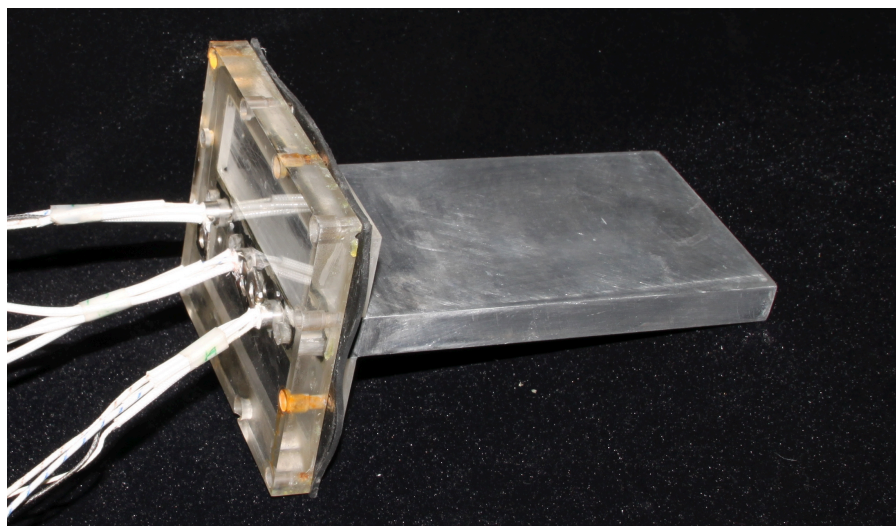
Figure 3.11: Aluminium central plate and J-type thermocouples.

Another situation in which it has been essential to use the chiller is the case when we consider the hot plate (Fig. 3.11). In this case the plate is maintained at $(30 \pm 1)°$ C by 3 J-type (iron / copper-nickel) thermocouples located longitudinally in the aluminum plate (Fig. 3.11). The thermocouples are equally spaced to ensure that the surface temperature of the plate is relatively homogeneous. Thermocouples can be used to measure the temperature as a thermometer or to generate heat when connected to a voltage source. The J-type thermocouples were used in the last sense.

In order to maintain plate temperature constant the voltage must vary when the water flow rate change. The J-type thermocouples were calibrated in air with a constant laboratory temperature of 20° C (Fig. 3.12). The monitoring of air temperature in the calibration of J-type thermocouples, and the water tank containing the pump, has been implemented by a K-type thermocouple. Both types of thermocouples have an appreciation of 0.1° C (Data Acquisition / Switch unit 34 970 HP).
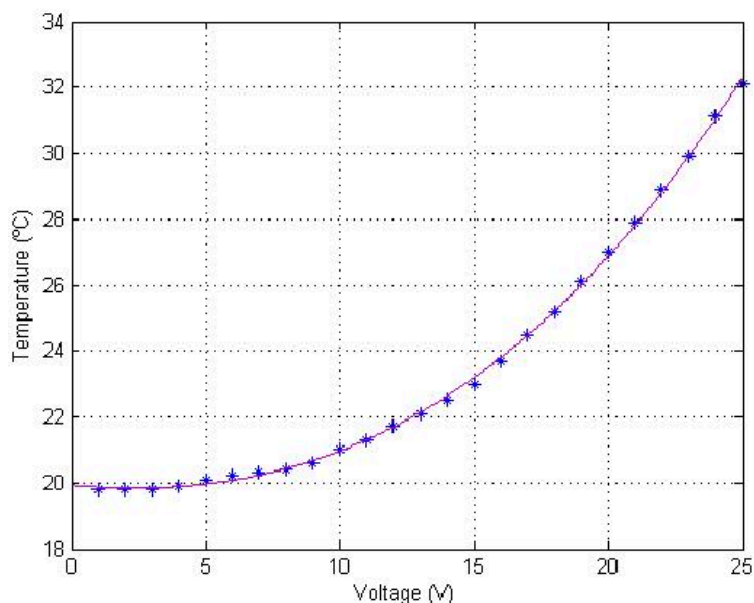
Figure 3.12: J-type thermocouple calibration in air.

3.4 Measurement planes

The choice of the planes in which experimental measurements have been made depends if working with multi plane system or with a single plane.

In the multi plane experiments, Fig. 3.13 shows the location of the (x^*, z^*) measurements planes. One of them remains fixed for all the measurement series while the position of the second is changed. Fixed plane was located at $y^* = 4$ and the mobile plane was located at $y^* = 3.5$, 3 and 2. The specific plane locations have been select depend on the physical distance available in the setup shown in section 2.3, Fig. 2.12.

A total of three series of experiments were performed. In each series a measure of the velocity field at $y^* = 4$ was taken. Selected (x^*, z^*) planes (Fig. 3.14a, 3.14b) were choose to visualize the flow structures inside the PCBs enclosure in experiments of a single plane. The first plane corresponds to $y^* = 0$, that is both, the midplane of the input and output channel. The second and third planes are located at $y^* = 1.5$ and $y^* = 3.5$ respectively. These two positions were selected since they are located at only 1 y^* units from the edge of the inlet and outlet channels. Coinciding with the midplane of the passage channel is the fourth plane at $y^* = 5$. In such way, the locations selected on the top region of the model, the fluid flow is symmetric with respect to those in the bottom region. Measurements have been made in (y^*, z^*) planes (Fig. 3.14c) located at $x^* = -0.75$, $x^* = 0$ and $x^* = +0.75$ too.

30
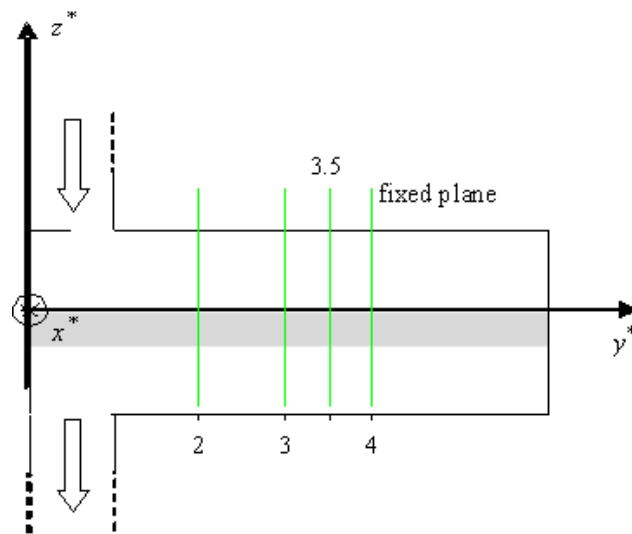
Figure 3.13: Setup sketch. Side view showing the location of measurements planes (x^*, z^*).
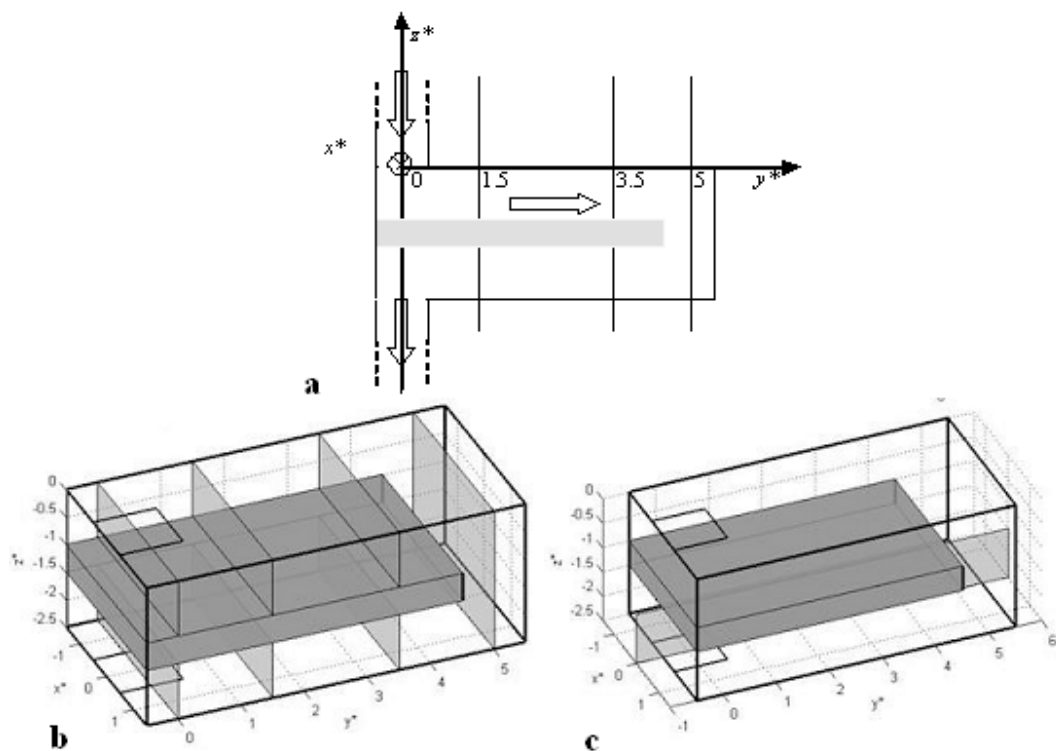
Figure 3.14: Location of relevant planes, **a** Side view showing the (x^*, z^*) planes. Three dimensional representation of **b** (x^*, z^*), **c** (y^*, z^*) planes.

31

Chapter 4

Numerical Method

Fluids and their associated phenomena are usually described in terms of partial differential equations, and there are no analytical solutions except in very specific cases. This is the reason why numerical solutions are needed. To obtain these solutions we use discretization methods approximating the differential equations with algebraic equations systems and the physical space (domain) with a discrete space (mesh). The objective is to solve the algebraic systems for these meshes in a computational form.

An important idea to remember is that there are differences between the physical phenomenon that we want to study, the mathematical model used to represent it (differential equations with appropriated initial and boundary conditions) and the numerical model to be solved (systems of algebraic equations). It is expected that these differences be reflected when comparing the results obtained by the numerical model with the experimental results .

Numerical simulations of the dynamic field in the PCB model have been obtained using caffa3d.MB. This software is an in-house flow solver, developed by Gabriel Usera as part of his PhD studies in the ECOMMFIT group [11]. It is an original Fortran 95 implementation of a fully finite volume method for solving the 3D incompressible Navier-Stokes equations in complex geometry. This 3D solver is based on a 2D solver described by Ferziger and Pèric [12]. Spatial discretization is based on block-structured, non-orthogonal, body fitted; collocated grids with first order (UDS) and second order (CDS) schemes for the convective term. Improved linear interpolation schemes for non-orthogonal grids are also included following Lehnhauser's work [13]. For the time discretization, fully implicit two-level first order (implicit backward Euler) and three-level second order schemes are available. Different interfaces between grids blocks are currently supported, among which only one-to-one interfaces are used here. Domain decomposition on the basis of grid blocks is applied through OpenMP, with current simulation running on dual processor machines.

4.1   Numerical model

In this section the numerical model is explained in detail and the specific features used to simulate our problem are presented.

4.1.1   The mesh

Meshes are a discrete representation of the domain geometry and define the location of the calculating points of variables. In addition meshes determine in which way the discrete approximations of differential equations are constructed. A structured mesh consists in families of mesh lines with the property that the family members do not cut with one another. This allows to number the lines of a given set consecutively. The position of any domain point (or volume control) is identified by a unique set of three indices (3D). When working with different blocks (which can be used to give different levels of mesh refinement in the places that the problem requires it) the mesh is named structured in blocks. At the moment that the mesh is defined the coordinate system used to perform the discretization have to be specified. In this work the rectangular coordinates are used with a unit vector base $(\widehat{e}_1, \widehat{e}_2, \widehat{e}_3)$ and where the velocity field will be represented by (u, v, w).

4.1.2   Mathematical model

The mathematical model comprises the mass (4.1.1) and momentum (4.1.2) balance equations for an incompressible Newtonian fluid with constant properties and the Boussinesq approximation for buoyancy effects due to temperature induced small density variations:

$$\int_S \left(\vec{v} \cdot \hat{\boldsymbol{n}}_s \right) dS = 0 \tag{4.1.1}$$

$$\int_\Omega \rho \frac{\partial u}{\partial t} d\Omega + \int_S \rho u \left(\vec{v} \cdot \hat{\boldsymbol{n}}_S \right) dS = \int_\Omega \rho \beta \left(T - T_{ref} \right) \overrightarrow{g} \cdot \hat{\boldsymbol{e}}_1 d\Omega$$
$$+ \int_S -p \hat{\boldsymbol{n}}_s \cdot \hat{\boldsymbol{e}}_1 dS \tag{4.1.2}$$
$$+ \int_S \left(2\mu \boldsymbol{D} \cdot \hat{\boldsymbol{n}}_S \right) \cdot \hat{\boldsymbol{e}}_1 dS$$

Those equations hold in any portion Ω of the domain, being S the boundary of Ω and $\hat{\boldsymbol{n}}_S$ the outward normal vector at the boundary S. The momentum balance equation (4.1.2) has been expressed for the first component u of the velocity vector $\vec{v} = (u, v, w)$, with similar expressions holding for the other components. The buoyancy term in equation (4.1.2) involves the density ρ, thermal expansion coefficient β and temperature T of the fluid, a reference temperature T_{ref} and gravity $\overrightarrow{g}$. The dynamic viscosity μ of the fluid and the

symmetric deformation tensor $\boldsymbol{D}$ were used for the viscous term. Where the symmetric deformation tensor was defined as:

$$\mathbf{D} = \begin{pmatrix} u_x & (u_y + v_x)/2 \\ (u_y + v_x)/2 & v_y \end{pmatrix} \tag{4.1.3}$$

where u_x represents the partial derivation of u respect x. In our case the heat equation was introduced in the model by the conservation law (4.1.4) for a generic passive scalar ϕ:

$$\int\limits_{\Omega} \rho \frac{\partial \phi}{\partial t} d\Omega + \int\limits_{S} \rho \phi \left(\vec{v} \cdot \hat{\boldsymbol{n}}_s \right) dS = \int\limits_{S} \Gamma (\nabla \phi \cdot \hat{\boldsymbol{n}}_s) dS \tag{4.1.4}$$

The discretized equations will be obtained by applying equations (4.1.1, 4.1.2 and 4.1.4) to each volume element.

The SIMPLE (Semi-Implicit Method Pressure Linked Equations) algorithm is implemented for the coupling between velocity and pressure [12]. Because the velocity field obtained from the discretized approximations to the momentum balance equation (4.1.2) is not subject to the incompressibility condition and thus it must be corrected to fulfil the mass balance equation (4.1.1). An equation to update the pressure field is also needed. The current estimates for the velocity and pressure fields $(\vec{v}^*, p^*)$ will be modified by adding velocity and pressure corrections $(\vec{v}', p')$ to obtain new current estimations $(\vec{v}, p)$:

$$\vec{v} = \vec{v}^* + \vec{v}' \qquad\qquad p = p^* + p' \tag{4.1.5}$$

A full description of the flow solver can be found in [11]. Validation of the flow solver against experimental data and benchmark simulations for different cases can be found also in [11, 27, 28], and for the present geometry in greater detail in [1].

4.2   Application of numerical model

4.2.1   The grid

The grid was made of six blocks where the inlet and outlet duct blocks were used to minimize the effect of boundary conditions on the region of interest of the flow.

In order to determine the degree of mesh refinement needed to achieve a proper fit to resolve the momentum and temperature boundary layer, simulations were performed for five different degrees of refinement. In this work the grid is homogeneous whose spatial resolutions were $h/20$ ($60 \times 120 \times 20$ bottom
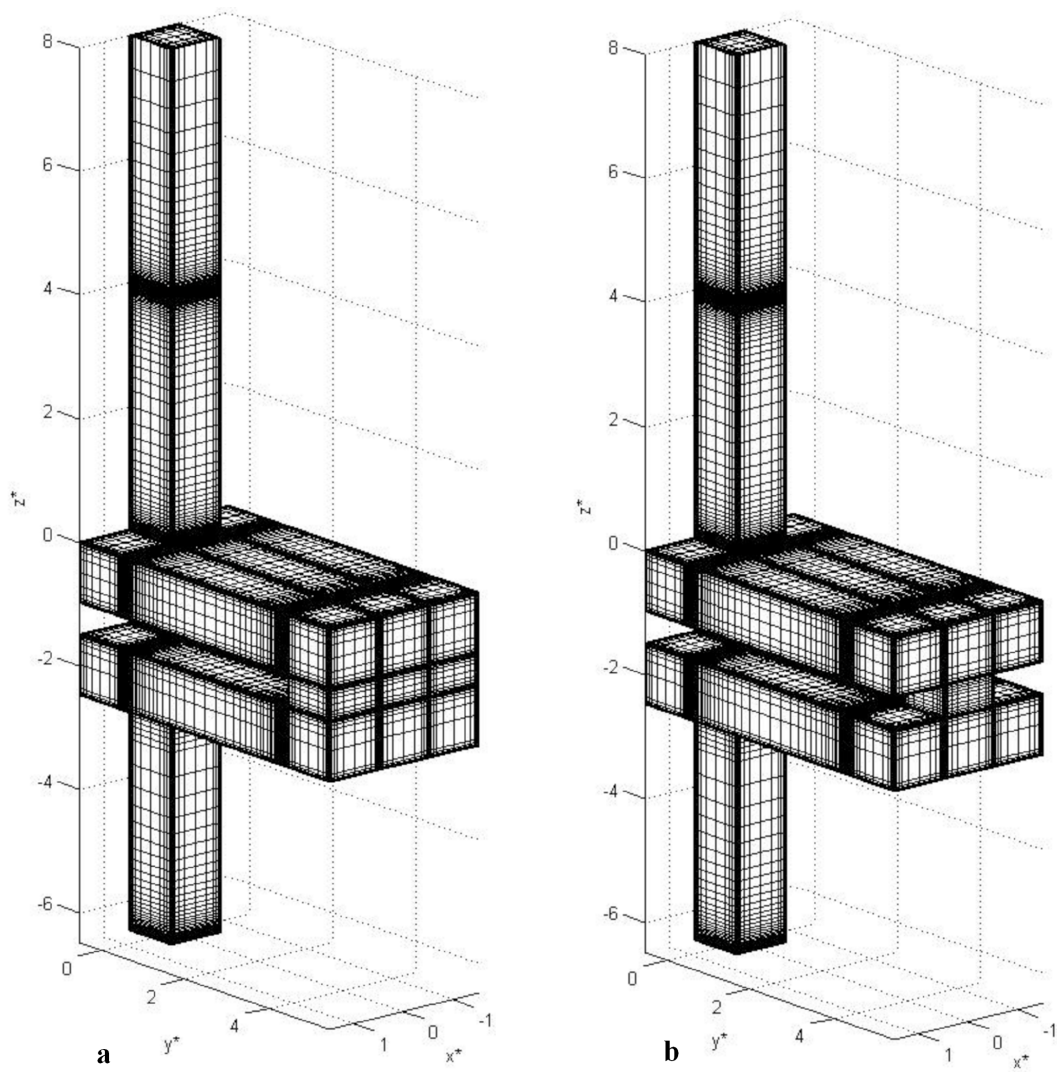
Figure 4.1: Numerical grid composed of six matching grid blocks. Shown at h/10 resolution near the walls, **a** closed, **b** open geometry.
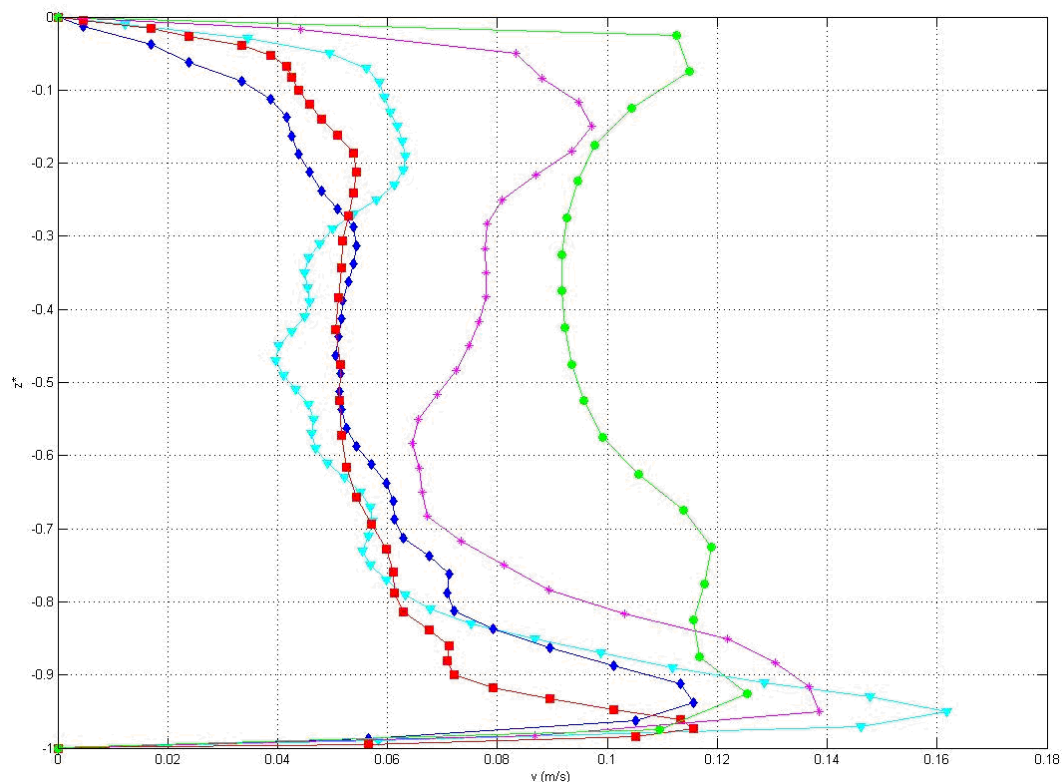
Figure 4.2: Closed geometry, $\text{Re} = 5.79 \times 10^3$, v component vs. z^* at $y^* = 3.5$ and $x^* = -0.75$ at the top channel of PCB model, homogenous grid spatial resolution: $h/20$ (circle), $h/30$ (star), $h/40$ (diamond), $h/50$ (triangle) and wall refined grid $h/65$ near the walls and about $h/40$ at the core (square).

and top section block dimensions), $h/30$ $(90 \times 180 \times 30)$, $h/40$ $(120 \times 240 \times 40)$ and $h/50$ $(150 \times 3000 \times 50)$. It is also considered a refined grid with a spatial resolution set to $h/65$ near the walls and about $h/40$ at the core (Fig. 4.1), using stretched grid blocks. Figure 4.2 shows the v component profile of the mean velocity field as function of height z^* in the top channel at $y^* = 3.5$ and $x^* = -0.75$. Where we can distinguish the differences between the grids with which we work. We can see that the profiles for homogeneous grids with spatial resolution $h/40$, $h/50$ and the refined grid are closer that the grids with resolutions $h/20$ and $h/30$. The computational cost of working with the finest homogeneous grid is very high because the number of cells for the open geometry is about 7×10^6 million (value close to the maximum allowed on the model) while with the $h/40$ spatial resolution we have about 3×10^6 cells.

Fig. 4.3 shows the temperature profiles at the bottom channel where is easy to see that the refined grid near the walls allows us to resolve the area near $z^* = -1.5$ better than the $h/50$ grid and in turn keep the number of cells approximately equal to the grid spatial resolution $h/40$. Taking this in

37
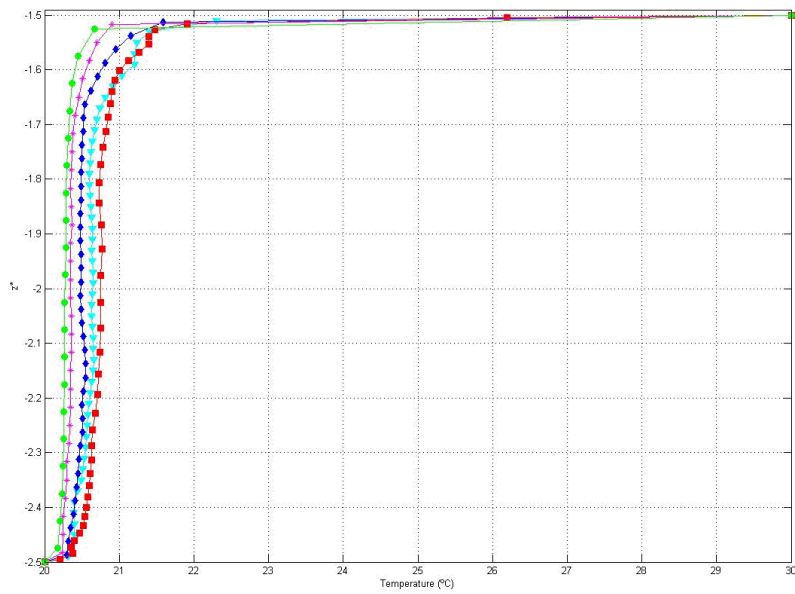
Figure 4.3: Closed geometry, $Re = 5.79 \times 10^3$, Temperature ($°C$) component vs. z^* at $y^* = 3.5$ and $x^* = 0$ at the bottom channel of PCB model, homogenous grid spatial resolution: $h/20$ (circle), $h/30$ (star), $h/40$ (diamond), $h/50$ (triangle) and wall refined grid $h/65$ near the walls and about $h/40$ at the core (square).
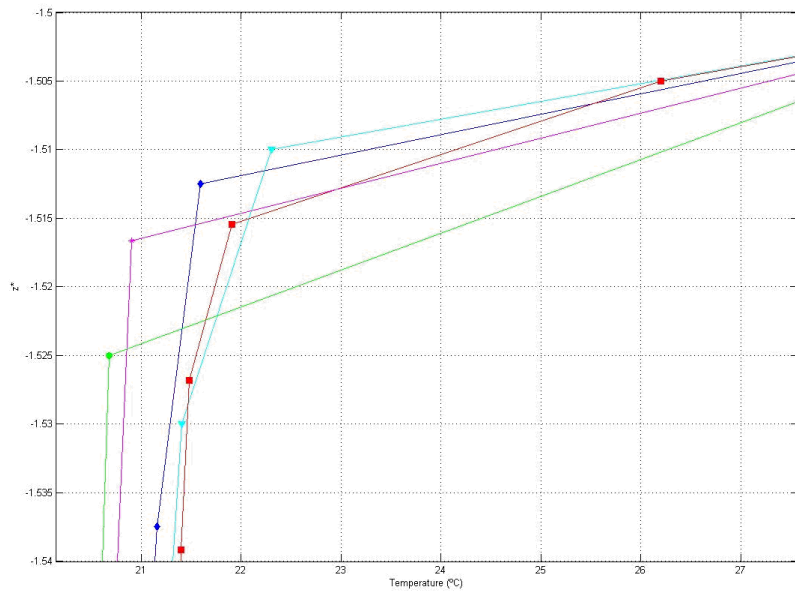
Figure 4.4: Zoom of Fig. 4.3.

account, the grid used in all cases presented in this work is the refined grid with $h/65$ near the walls and about $h/40$ in the center, representing 3.45×10^6 calculation points for the open geometry and 3.38×10^6 cells for the close one.

With the refined grid temperature boundary layer is best resolved with homogeneous grids the Fig. 4.4 shows. This can be seen in the fact that the calculated temperature in the second cell (from the wall) of the refined grid is the same order $(21.9°C)$ that the temperature obtained in the first cell of the homogeneous grids with resolutions $h/40$ $(21.6°C)$ and $h/50$ $(22.3°C)$.

4.2.2 Initial conditions and regime state

Reynolds number defined by Re$= U_0 h\rho/\mu$ was set ranging from Re $= 300$ to Re $= 10000$. The Table 4.1 shows the select Re number, corresponding to mean velocity at the inlet region, respectively.

Re	U_0 (m/s)
300	1.218×10^{-2}
600	2.436×10^{-2}
1160	4.8×10^{-2}
3000	1.218×10^{-1}
5790	2.4×10^{-1}
8000	3.245×10^{-1}
10000	4.060×10^{-1}

Table 4.1: Different Reynolds numbers corresponding to mean velocity at the inlet region.

The Large Eddy Simulation (LES) turbulence model has been used for Re higher than 5000. This model is based on the Smagorinsky model for subgrid scale. In our case,a "top hat" filter kernel is considered to obtain the filtered velocity containing the large scale components of the total velocity field. The dimensionless time step was $dt/(h/U_0) = 5 \times 10^{-3}$. Simulations have been run starting from null velocity fields through 11×10^3 time steps, or about 55 s of flow time.

Relaxation coefficients were used 0.8 for the velocity field and 0.3 for the pressure field, these values are common for non stationary simulations with time steps small and orthogonal grids. As convergence parameter was monitored the total sum of the absolute values of the residues. The chosen values of the relaxation coefficients joined with a cycle of 10 outer iterations allowed to ensure a reduction of the convergence parameter in 3 orders of magnitude at each time step. These convergence levels are adequate to analyze the state of flow strongly governed by the boundary conditions.

Throughout the simulations the flow exhibits non-stationary characteristics but reaching a regime state independent of initial conditions. The figure 4.5
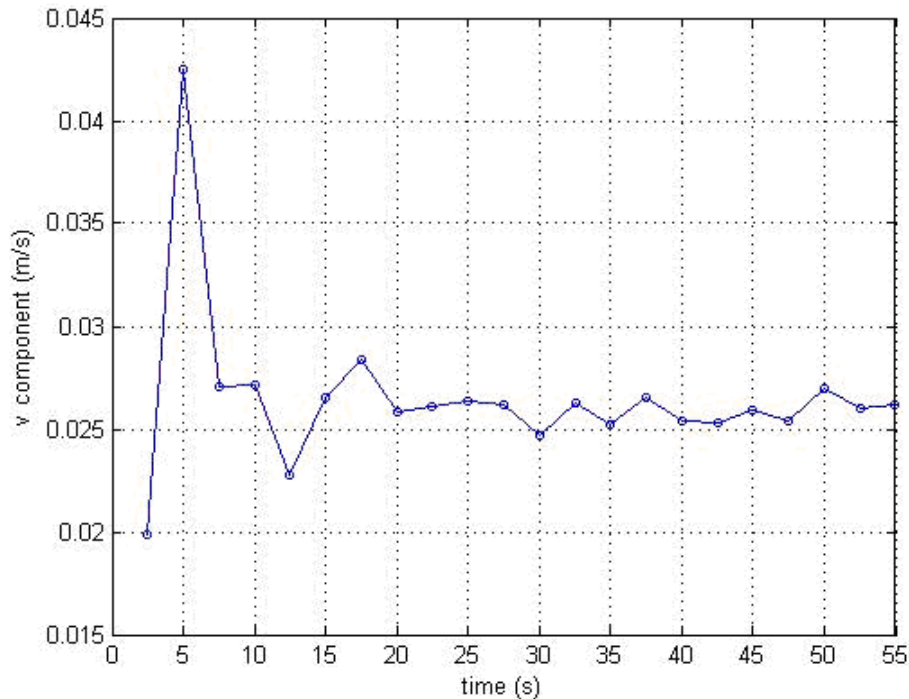
Figure 4.5: Closed geometry, Re $= 1.16 \times 10^3$, v component as function of time at $x^* = 0$, $y^* = 3.5$ and $z^* = -0.5$ (top channel of PCB model).

shows the behavior of v component at $x^* = 0$, $y^* = 3.5$ and $z^* = -0.5$ (correspond to the top channel of PCB model) as function of time. The mean fields presented in this work were averaged over a time period that did not include the start time (from $25s$ to $55s$).

4.3   LES Model

The simplest approach from the conceptual point of view of the turbulence simulation is to solve the Navier- Stokes equations without averaging or approximation other than numerical discretizations whose errors can be estimated and controlled. This approach is called direct numerical simulation (DNS). The DNS have high computational cost associated with the requirement to fully simulate the flow, even in their small scales, where viscous dissipation occurs, that it need a large number of grid points to simulated all scales.

Large Eddy Simulaion (LES) methods reduce the cost associated with the DNS method, simulating the flow only up to scales of turbulence larger than a given level.

The large scale motions are generally much more energetic than the small scale ones; their size and strength make them by far the most effective trans-

40

porters of the conserved properties. The small scales are usually much weaker and provide little transport of these properties. Large eddy simulations (LES) is an approach that treats the large eddies more exactly than the small ones.

A velocity field containing only the large scale components of the total field is needed. This is best produced by filtering the velocity field $\vec{v} = (u, v, w)$; in this approach, the large or resolved scale field, the one to be simulated, is essentially a local average of the complete field. The filtered velocity is defined by:

$$\overline{\vec{v}(P)} = \int G(|P - P'|) \cdot \vec{v}(P') \cdot dV' \qquad (4.3.1)$$

Where $G(\mathbf{r})$, the filter kernel, is a localized function. In the sense that weighs with higher weight values $\vec{v}(P')$ near P, and decreases as one moves away from P thus establishing a "width" filter Δ. In this way it retains the local information on point P, while "softens" the field, reducing the information content on scales smaller than Δ. Roughly, eddies of size larger than Δ are large eddies while those smaller than Δ are small eddies, the ones that need to be modeled.

The most common choices for the filter function $G(\mathbf{r})$ are the Gaussian and the cutoff (top hat) filters:

$$G(\mathbf{r}) = A \cdot \exp^{-\mathbf{r}^2/\Delta^2} \qquad (4.3.2)$$

$$G(\mathbf{r}) = \begin{cases} 1 & r < \Delta \\ 0 & r > \Delta \end{cases} \qquad (4.3.3)$$

The choice of the filter should be taken into account when implementing the modeling sub-grid stresses and finally to interpret the solution obtained as a solution for the filtered field and consider its relationship with the real field.

When Navier-stokes and continuity equations with constant density are filtered, equations 4.3.4 and 4.3.5 are obtained.

$$\frac{\partial \bar{u}_i}{\partial t} + \frac{\partial (\overline{u_i u_j})}{\partial x_i} = -\frac{1}{\rho}\frac{\partial \bar{p}}{\partial x_i} + \nu \frac{\partial^2 \bar{u}_i}{\partial x_i \partial x_j} \qquad (4.3.4)$$

$$\frac{\partial \bar{u}_i}{\partial x_i} = 0 \qquad (4.3.5)$$

The nonlinear advection term in equation 4.3.4 is the only one that presents difficulties. Developing the velocity field into its filtered component $\bar{u}$ and in the sub grid component u':

$$u_i = \bar{u}_i + u' \qquad (4.3.6)$$

which implicitly defined:

$$u' = u_i - \bar{u}_i \tag{4.3.7}$$

Is then obtained:

$$\overline{u_i u_j} = \overline{(\bar{u}_i \bar{u}_j)} + \overline{(\bar{u}_i u'_j)} + \overline{(u'_i \bar{u}_j)} + \overline{u'_i u'_j} \tag{4.3.8}$$

In general the filtered velocity field does not unchanged to the successive application of the filter [31]:

$$\overline{(\bar{u}_i \bar{u}_j)} \neq \bar{u}_i \bar{u}_j \tag{4.3.9}$$

An usual definition of sub grid tension terms as:

$$\tau_{ij}^s = -\rho(\overline{u_i u_j} - \bar{u}_i \bar{u}_j) \tag{4.3.10}$$

that is the difference between the term present in the equations and the component effectively resolved of larger scales.

In this context, τ_{ij}^s is called *sub-grid Reynolds stress*, and it is in fact, the large scale momentum flux caused by the action of the small or unresolved scales. Is important to keep in mind that the width of the filter, Δ, need not have anything to do with the grid size, h, other that the condition that $\Delta > h$ [12].

The sub-grid Reynolds stress are not determinable at priori from the resolved flow and should be introduced assumptions and models used to calculate them.

4.3.1   Smagorinsky model

In this work the Smagorinsky model has been used. It is a "first order" close model , since the sub grid stress are directly related to the filtered velocity field, through the tensor deformation of this and by introducing a coefficient of eddy viscosity.

$$\tau_{ij}^s = 2\mu_T S_{ij} + \frac{1}{3}\tau_{kk}^s \delta_{ij} \tag{4.3.11}$$

where μ_T is the eddy viscosity and S_{ij} is the strain rate of the large scale or resolved field. The sub-grid eddy viscosity can be calculate from the following expression:

$$\mu_T = (C.\Delta)^2 (2.S_{ij}S_{ij})^{1/2} \tag{4.3.12}$$

where C is a constant and Δ is the filter width.

The diagonal term of the sub-grid stress τ_{ij}^s, explicitly written in 4.3.11, could also be modeled. However there is no need because it can be implicitly combined with the pressures term. Therefore we model only the part of zero trace of the tensor:

$$\tau_{ij}^{SGS} = 2\mu_T S_{ij} \tag{4.3.13}$$

this term is commonly refered as sub-grid stress. The main requirement of the sub-grid stress model is to produce the kinetic energy proper dissipation, absorbing it from the resolved flow. Then, the determination of the constant C must ensure the necessary dissipation. Common values of constant C are in the range from 0.1 to 0.15 [31]. Although, the latter sometimes causes a value of excessive dissipation.

4.4 Analysis of the temperature effect

The simplest element that can be added to a flow is a scalar quantity such as temperature. In case of the presence of the scalar quantity does not affect the properties of the fluid we speak of a passive scalar. In a more complex case, the density and viscosity of the fluid may be modified by the presence of the scalar and we have an active scalar. In a simple example, the fluid properties are functions of temperature.

The variation of the transport properties with temperature can be very large (depends on the differences between the fluid temperature and the heater component temperature) and must be taken into account but are not difficult to handle numerically. The important issue is that the energy and momentum equations are now coupled and must be solved simultaneously. On each outer iteration, the momentum equations are first solved using transport properties computed from the 'old' temperature field. The temperature field is updated after the solution of the momentum equations has been obtained for the new outer iteration and the properties are updated.

Variations in density, viscosity and Prandtl number increase the non-linearity of the equations. The sequential solution method can be applied to these flows in the much the same way they are applied to flows with variable tempera-ture. One recalculates the fluid properties after each outer iteration and treats them as known during the next outer iteration. If the property variation is significant the convergence may be slowed considerably. If the temperature differences are small (around 10° C) [29], the variations of the fluid properties are not important and the temperature behaves as a passive scalar. Since the temperature is a passive scalar, it can be computed after the computation of the velocity field has been completely converged, making the task much sim-pler. The dependency of the fluid properties (ν, ρ, Pr) on temperature in the given temperature rage is computed by a 4th order polynomial function.

$$\phi_T = a_\phi T^4 + b_\phi T^3 + c_\phi T^2 + d_\phi T + e_\phi \tag{4.4.1}$$

where the constants $a_\phi, b_\phi, c_\phi, d_\phi, e_\phi$ for the particular variable $\phi = \{\mu, \rho, Pr\}$ were obtain by fitting the data found in property tables [30]. Table 4.2 shows

the 4th order polynomial function coefficients used in the fitting shown in Figures 4.6, 4.7 and 4.8.

	a	b	c	d	e
Viscosity	3.03×10^{-11}	-8.57×10^{-9}	9.48×10^{-7}	-5.42×10^{-5}	1.77×10^{-3}
Density	-1.6×10^{-7}	4.8×10^{-5}	-8.1×10^{-3}	6.6×10^{-2}	1.0×10^{3}
Prandtl	3.3×10^{-7}	-8.9×10^{-5}	9.3×10^{-3}	-4.9×10^{-1}	1.4×10^{1}

Table 4.2: Coefficients of 4th order polynomial fits to physical properties.
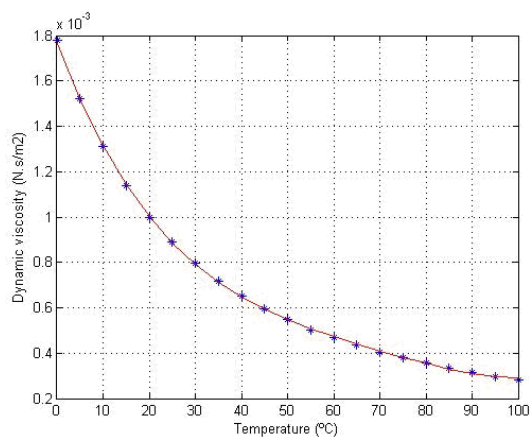
Figure 4.6: Dynamic viscosity ($N.s/m^2$) vs. Temperature ($^\circ C$), experimental data and fitting.
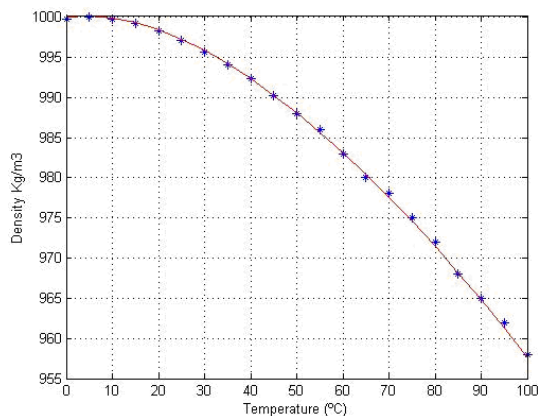
Figure 4.7: Density (Kg/m^3) vs. Temperature ($^\circ C$), experimental data and fitting.

44
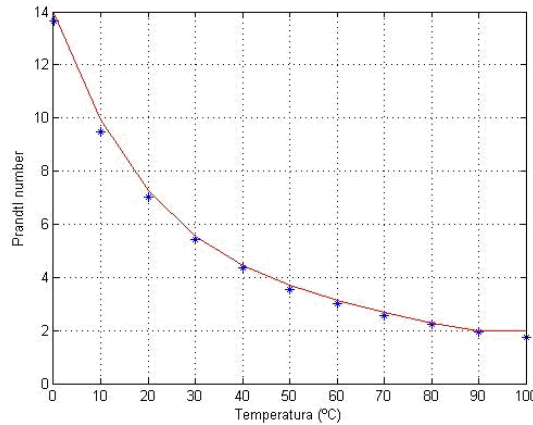
Figure 4.8: Prandtl number vs. Temperature ($°C$), experimental data and fitting.

At first, the hypothesis that if the temperature differences are small then the variations in physical properties are negligible was considered. This consideration was made for two reasons, first is, that this hypothesis is well justified in the literature ([29], [12]) and second because in this moment the numerical model did not include the ability to work with variable physical properties. Thus performing simulations with constant physical properties and a temperature difference of $\Delta T = 10°$ C. Subsequently, amendments were made in the numerical model to include the variation of physical properties due to temperature. So simulations were performed to verify that the considered hypothesis was proper and to study the system behavior for higher temperature differences.

The cold and reference temperatures (fluid temperature) were $T_c = T_{ref} = 20°$ C while hot temperature was $T_h = 30°$ C (plate temperature) in one case and $T_h = 50°$ C thus obtaining temperature differences of $\Delta T = 10°$ C and $\Delta T = 30°$ C. The select Re number for this simulation was Re $= 5.79 \times 10^3$ and the initial conditions of the physical properties were established evaluating polynomials (Table 4.2) in $\bar{T}$, defined as $\bar{T} = \frac{T_c + T_h}{2}$

A good way to study the temperature influence in the system is through the Nusselt number. The Nusselt number is one of the most important parameter in convective heat transfer problems. Convection intensity is determined by the value of Nusselt number. The average Nusselt number of plate is calculated in order to realize the heat transfer phenomenon around the heat source. As we know the heat transfer by convection is q=HAΔT, where H is convective coefficient, A is the contact area and ΔT is the difference of temperature. The heat exchange between fluid and solid boundary:

$$\frac{q}{A} = H(T_p - T_\infty) = -k_f \left(\frac{\partial T}{\partial z} \right)_{z=-1,-1.5} \tag{4.4.2}$$

45

where k_f is the conductance coefficient of fluid, T_∞ is the inlet temperature, T_p is the plate temperature, the partial derivation is evaluated in the plate's upper wall ($z = -1$) and in the plate's bottom wall ($z = -1.5$). The definition of Nusselt number:

$$Nu = \frac{Hh}{k_f} = \frac{h\left[\frac{\partial(T_p - T)}{\partial z}\right]_{z=-1,-1.5}}{(T_p - T_\infty)} \qquad (4.4.3)$$

Figure 4.9 shows the behavior of mean Nusselt number as function of y^* position for constant and variable physical properties with temperature differences of $\Delta T = 10°$ C and $\Delta T = 30°$ C.
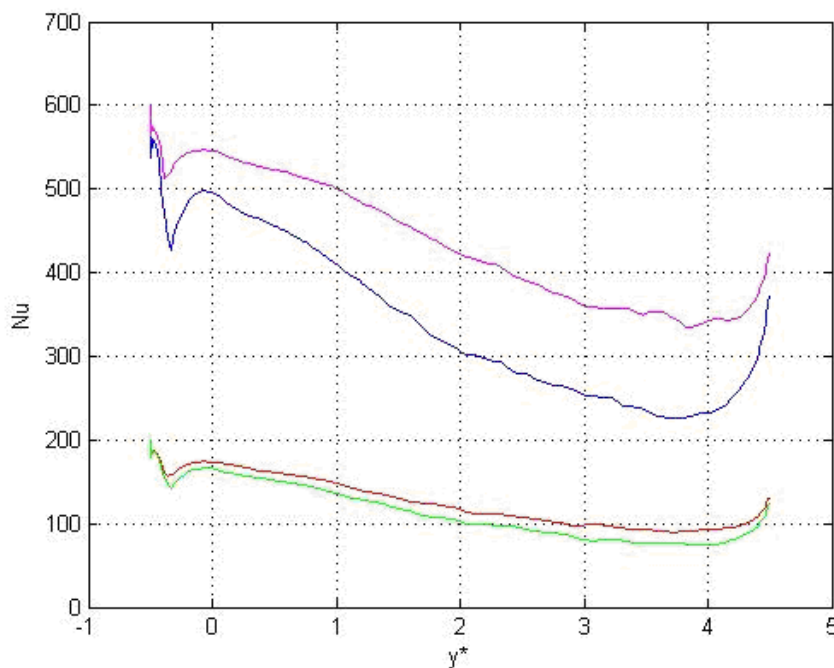
Figure 4.9: Mean Nusselt number vs. y^* in the top channel of PCB model for $\Delta T = 10°$ C with constant (green) and variable (red) physical properties. For $\Delta T = 30°$ C with constant (blue) and variable (magenta) physical properties.

Where it shows that the behavior of the Nusselt number is similar for each temperature difference, though is always greater for cases with variable physical properties. For a temperature difference of $\Delta T = 10°$ C, the difference in the values of Nusselt number between the variable and constant physical properties is less than 9% while for the difference of $\Delta T = 30°$ C the Nusselt number difference is 30%.

Based on these results we conclude that for a temperature difference of $\Delta T = 10°$ C the variations in physical properties are negligible.

46

Chapter 5

Studied cases

In order to study the spatial and temporal evolution of flow structures and heat transfer in PCB enclosed cavities several cases have been analyzed. Tables 5.1 and 5.2 shows the numerical and experimental studied cases.

Numerical simulations considered in Table 5.1 have been developed using a refined grid with a spatial resolution set to $h/65$ near the walls and $h/40$ at the core (section 4.2.1), considering constant physical properties, $\rho(20°C) = 998.3Kg/m^3$ and $\mu(20°C) = 1 \times 10^{-3}N.s/m^2$.

Re	Temperature (° C)	Experimental		Numerical	
		Open	Closed	Open	Closed
100	$\Delta T = 10$			X	X
	constant				
300	$\Delta T = 10$	X		X	X
	constant	X	X	X	X
600	$\Delta T = 10$			X	X
	constant		X		
1160	$\Delta T = 10$	X		X	X
	constant	X	X	X	X
3000	$\Delta T = 10$			X	X
	constant				
5790	$\Delta T = 10$	X		X	X
	constant	X	X	X	X
8000	$\Delta T = 10$			X	X
	constant				
10000	$\Delta T = 10$			X	X
	constant				

Table 5.1: Cases considering constant physical properties and a temperature difference of $\Delta T = 10°$ C.

47

The temperature difference between the plate and the fluid at the entrance was considered $\Delta T = 10°$ C and $\Delta T = 0°$ C (constant temperature system). To study the influence of the Re number and the PCB geometry in the plate heat transfer, numerical simulations for eight different Reynolds have been implemented, these values cover a wide range of Re from pure laminar to pure turbulent flow. The dependency of heat transfer due to the mean inlet velocity (Nusselt number vs. Reynolds number) has been studied for both plate geometries. Behavior of mean Nusselt number along the $y*$ direction for different Re and both geometries. Simulations including a temperature difference of $\Delta T = 30$ ° C have been developed considering constant and variable physical properties, the same refined grid has been used.

Re	Experimental (Open geometry)	Numerical	
		Variable	Constant
300	X		
1160	X		
5790	X	X	X

Table 5.2: Cases considering variable physical properties with temperature difference of $\Delta T = 30°$ C

During the numerical simulations data was saved every 2.75 seconds, using the last 10 data set files to calculate the mean fields.

To study the behavior of variables in function of time we have performed simulations in which 600 files were saved using same period of time, that is storing every 0.092 seconds.

Each data file has a size of 150 Mb approximately which save 600 files creating storage problems and doubles the execution time for each case. Although the mean velocity and temperature fields obtained by averaging the instant fields over time, in the same period in which the system was in regime, does not differ. For this reason we chose to save the data every 2.75 seconds.

An special case is the measurements obtained at Reynolds number of $Re = 600$. In this case the multi plane technique was used (section 2.3). Thus measurements of two simultaneous planes with the closed geometry plate was implemented to obtain two simultaneous velocity fields.

From the experimental configuration a set of 1000 instantaneous fields are obtained for each studied plane corresponding to a one second measurement generating a 810Mb data file. Thus the mean velocity fields shown the next chapters are the averages of those 1000 files, unless otherwise specified. Images quantity were limited by the cameras memory and image size. The images were acquired when the system was in regime, having lost dependency on initial conditions so that the measurement of only one second is enough for

the images to be representative for what happens in the system.

It is important point that in the experimental set-up the inlet velocities were established by adjusting the flow rate using 3 rotameters. The flow rates chosen were (500 ± 5) l/h, (100 ± 5) l/h and (26 ± 1) l/h these flow rates correspond to Reynolds numbers (5735 ± 630), (1144 ± 126) and (296 ± 33) respectively.

Chapter 6

Unheated open geometry

This chapter describes the flow behavior in the open geometry. In this case the plate that models the PCB has the same temperature as the flow. Three different values of the inlet mean velocity are studied. The results are obtained from both numerical simulations and experimental measurements. In first place the behavior of the flow for $Re = 1160$ is analyzed. A good approach to study the flow structures is plotting the $3D$ streamlines (Fig. 6.1) because its gives a global behavior of the fluid movement.

In the top channel the fluid follows a quasi symmetric double spiral path (Fig. 6.1a) but for the bottom channel the streamlines are completely different (Fig. 6.1b).
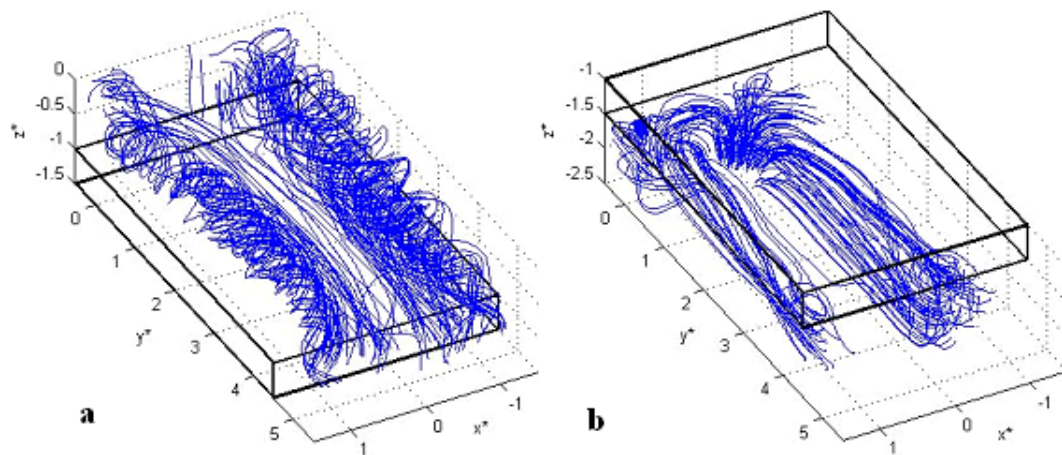
Figure 6.1: 3D streamlines , Re=1.16×10^3, a Top channel,b bottom channel, open geometry.

The spiral behavior of the flow has disappeared giving way to the existence of straight lines and several vortical structures with smaller intensity located

near the passage channel. This behavior is the one found before by Usera et al. [11]. On the other hand. a vortex core can be defined [34], in an
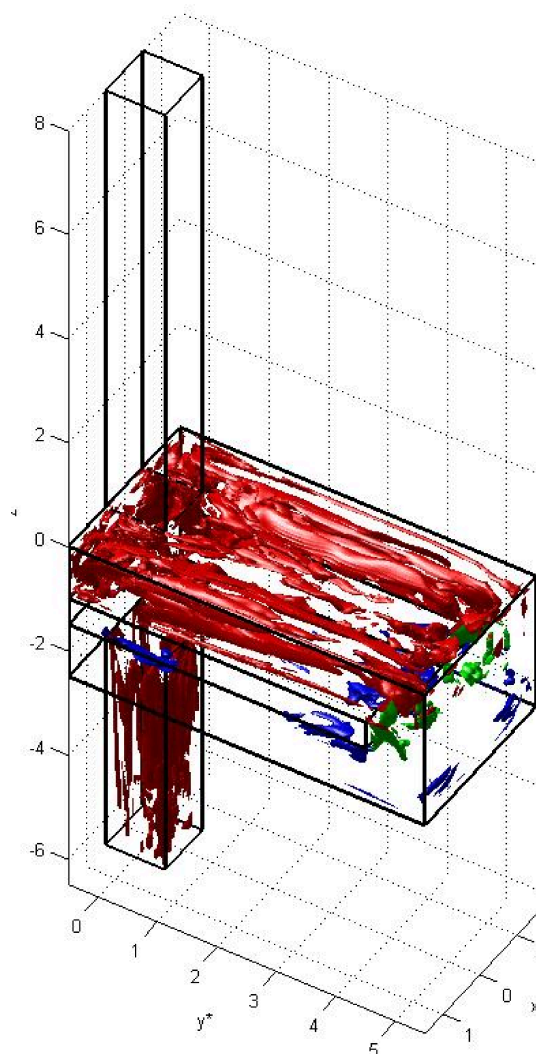
Figure 6.2: Vortical structures educed by λ_2 iso-surfaces from numerical simulation.

incompressible flow, as a connected region with two negative eigenvalues of the symmetric tensor $S^2 + \Omega^2$, where S and Ω are respectively the symmetric and antisymmetric parts of the velocity gradient tensor $\nabla \vec{u}$; i.e. $S_{ij} = \frac{1}{2}(u_{i,j} + u_{j,i})$ and $\Omega = \frac{1}{2}(u_{i,j} - u_{j,i})$. Note that since $S^2 + \Omega^2$ is symmetric, it has only real eigenvalues. If λ_1, λ_2 and λ_3 are eigenvalues and $\lambda_1 \geq \lambda_2 \geq \lambda_3$, then the definition is equivalent to the requirement that $\lambda_2 < 0$ within the vortex core. Thus a way to observe vortical structures is by means of λ_2 iso-surfaces. These iso-surfaces were obtained from the numerical data since the three components of the velocity field are available. From the experimental data is not possible
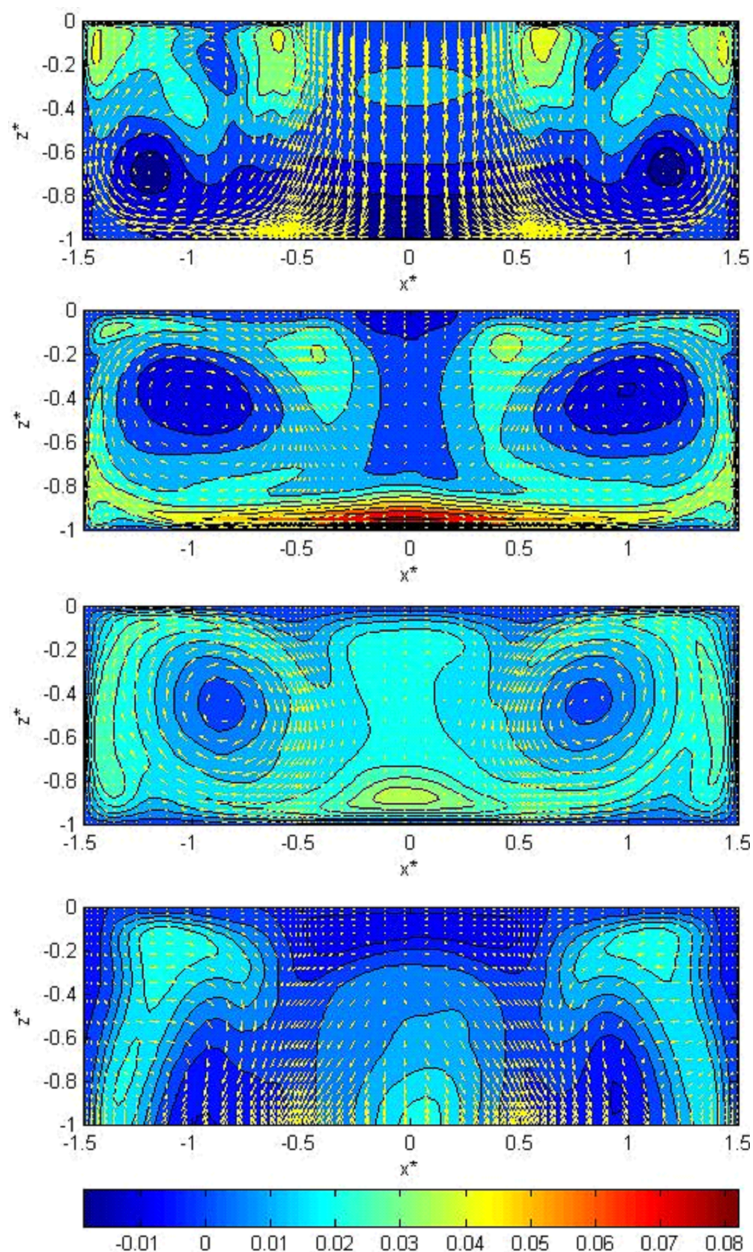
Figure 6.3: $Re = 1.16 \times 10^3$ at plane (x^*, z^*) in the top channel of PCB model. Numerical mean velocity field for (up to down) $y^* = 0$, $y^* = 1.5$, $y^* = 3.5$ and $y^* = 5$. Vectors u and w component, contours v component.

to calculate it as only two components of the velocity field are measured.

Figure 6.2 shown λ_2 iso-surfaces inside the cavity and in the outlet channel where the same iso-value was used. Clearly two vortical structures are presented in the top channel which disappear in the passage channel.

When the flow enters the cavity hits the plate which causes two counter ro-

53

tating vortical structures oriented along the y^* direction that are held throughout the top channel. Figure 6.3 shows the numerical mean velocity field in the top channel at selected (x^*, z^*) planes (see Fig. 3.14) and illustrates two quasi-symmetric counter-rotating vortices whose centers moves upwards as the flow move away from the entrance. The vector representation corresponds to the components u and w while the v component is represented by contours. As it expected, the larger velocity vectors are found in the inlet region. Outside that region, on the chosen planes, the maximum of each components of the mean velocity is found at $y^* = 1.5$ where u and w components are similar (44.3×10^{-3} m/s to the u component, 43.2×10^{-3} m/s to the w component) whilst the v component is almost double (82.0×10^{-3} m/s). As expected v is the largest component coinciding with the main flow direction. This can also be seen observing the contours of the mean velocity modulus at plane (y^*, z^*) for $x^* = 0$, Fig. 6.4. This figure also shows two vortex oriented in the x^*
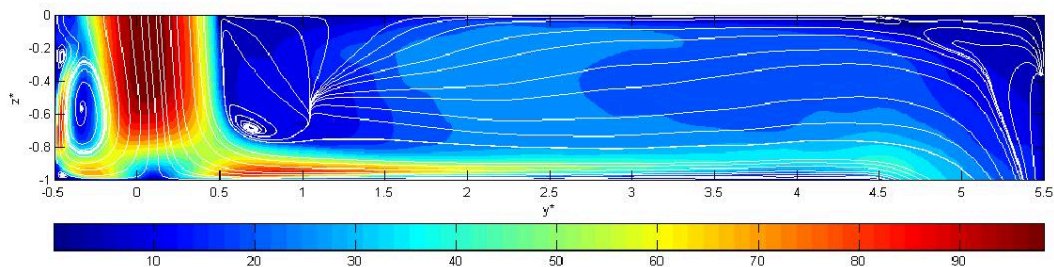
Figure 6.4: Mean velocity field (mm/s), $Re = 1.16 \times 10^3$, plane (y^*, z^*) at $x^* = 0$ in the top channel of PCB model.

direction one at $(y^*, z^*) = (-0.4, -0.6)$ and another at $(y^*, z^*) = (0.7, -0.7)$. The first one is formed by the clash of incoming fluid with the rear wall cavity and the second, smaller that the first, is produced by the jet impinging.

Experimental results at $Re = (1144 \pm 126)$ (Fig. 6.5) show that the large scale structures found in the top channel are practically the same as those obtained for the numerical simulation (Fig. 6.3).

The larger velocity vectors shown in Fig. 6.6 are of the order of 55 mm/s while the computed root mean square (rms) has a maximum value of about 24 mm/s located mainly near the boundaries, while the rms has a significant reduction near the vortex centres, showing values smaller than 5 mm/s. These values of the velocity deviation indicate that the large structures depicted in Fig. 6.6 are representative of the instantaneous flow structures of the system, and that the main difference between the mean field and the instantaneous structures are located near the borders of the system. Small differences can be observed at $y^* = 0$ and $y^* = 5$. At plane $y^* = 0$ in the experimental case two

54
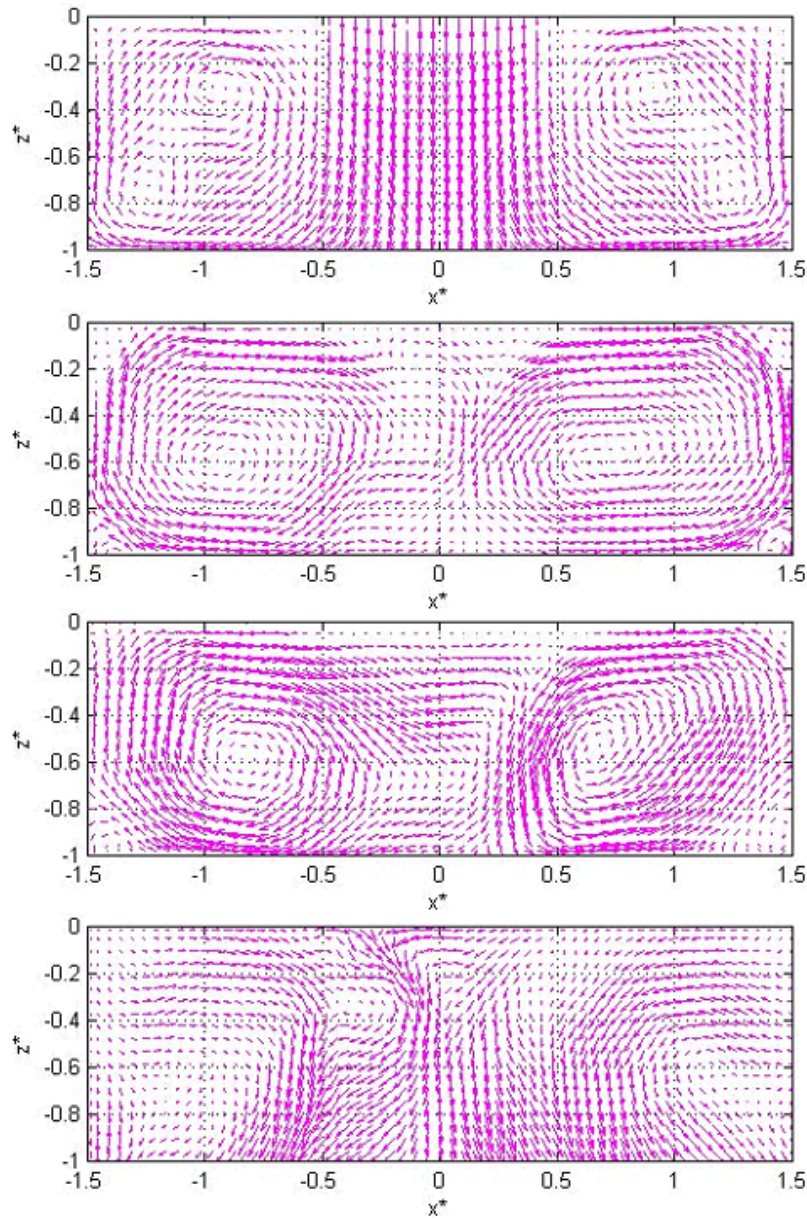
Figure 6.5: $Re = (1144 \pm 126)$ at plane (x^*, z^*) in the top channel of PCB model. Experimental mean velocity field for (up to down) $y^* = 0$, $y^* = 1.5$, $y^* = 3.5$ and $y^* = 5$.

vortices and a transition saddle point are present, the lowest vortex is located at $(x^*, z^*) = (0.92, -0.32)$, the highest one is located at $(x^*, z^*) = (1.23, -0.75)$ and the saddle point is a intimidate position in $(x^*, z^*) = (1.10, -0.49)$. Numerical simulations for the same plane show a vortex located at $(x^*, z^*) = (1.17, -0.68)$ a remnant of a vortex structure corresponds with a minimum of mean velocity field located in $(x^*, z^*) = (0.98, -0.30)$. Observing the mean velocity fields in the plane $y^* = 5$ for experimental and numerical results

55
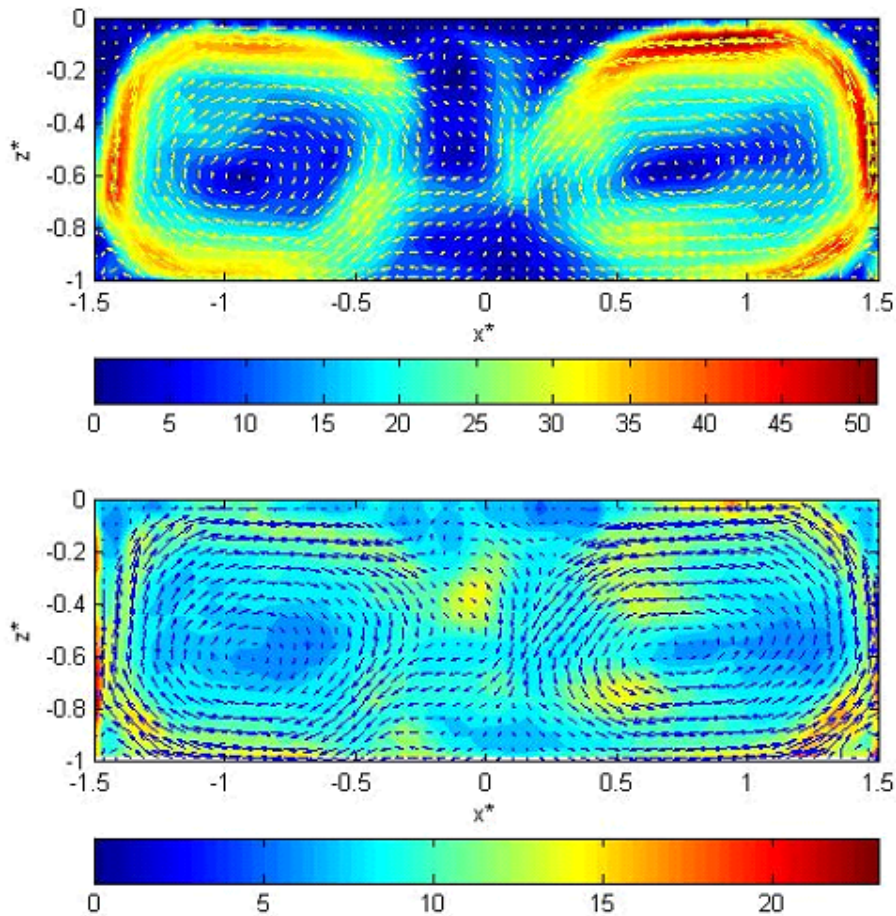
Figure 6.6: $Re = (1144 \pm 126)$ at plane (x^*, z^*), $y^* = 1.5$ in the top channel of PCB model. Experimental mean velocity modulus (up), rms (down).

(Fig. 6.7) we can see that they are quite similar though the experimental results are slightly more "disordered" especially in the center of the plane $(-0.5 > x^* > 0.5)$.

When comparing the experimental and the numerical results it should be kept in mind that in the numerical simulations the system is completely "ideal" while in experimentation some intrinsic errors can exist which can lead to small differences in obtained fields .

Vortical structures presented in the flow at $Re = 5.79 \times 10^3$ are not significantly different from that obtained at $Re = 1.16 \times 10^3$. Although some differences can be found in the structures shape mainly in plane $y^* = 1.5$ and $y^* = 3.5$ for $Re = 300$ where a smaller pair of counter-rotating vortices appear in the center as Fig. 6.8 shown. In the plane $y^* = 1.5$ a pair of small quasi symmetry counter rotating vortices located at $(x^*, z^*) = (0.15, -0.19)$ and $(x^*, z^*) = (-0.2, -0.16)$ can be observed. The rotation direction of this small
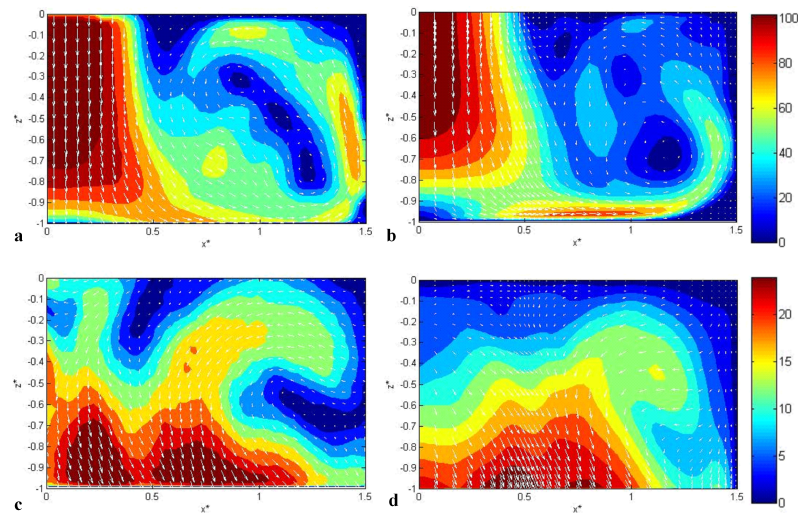
Figure 6.7: Mean velocity field modulus (mm/s), $Re = 1.16 \times 10^3$ at plane (x^*, z^*), $(0 > x^* > 1.5)$ region. Plane $y^* = 0$, **a** experimental **b** numerical. Plane $y^* = 5$, **c** experimental, **b** numerical.
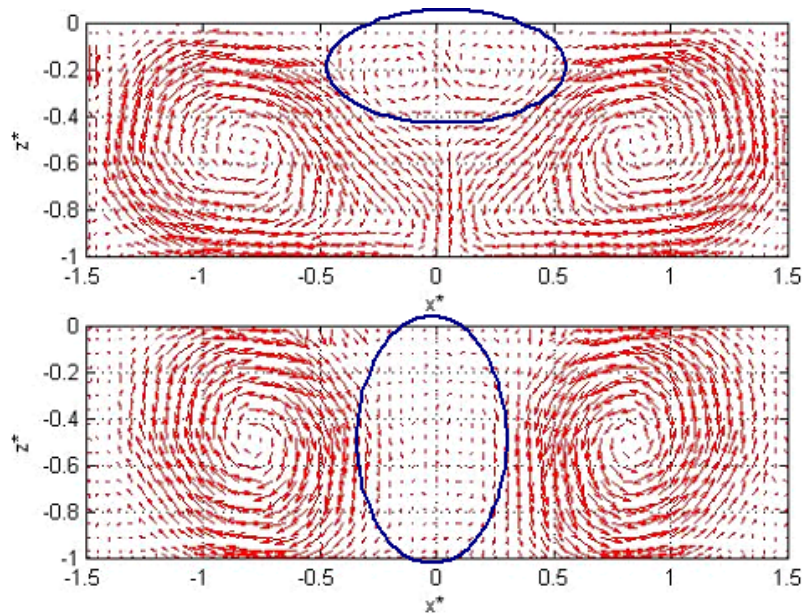
Figure 6.8: Open geometry, $Re = 300$ at plane (x^*, z^*) in the top channel of PCB model. Experimental mean velocity field for (up to down) $y^* = 1.5$ and $y^* = 3.5$.

vortices is opposite to that of large vortices that appear in Fig. 6.8. The vortex structures present in the plane $y^* = 3.5$ are less defined than in the plane $y^* = 1.5$, these are spread over the channel height and in turn concentrated in

6. UNHEATED OPEN GEOMETRY

the central area of this ($x^* = [-0.2, 0.2]$). To see what happens to the pair of
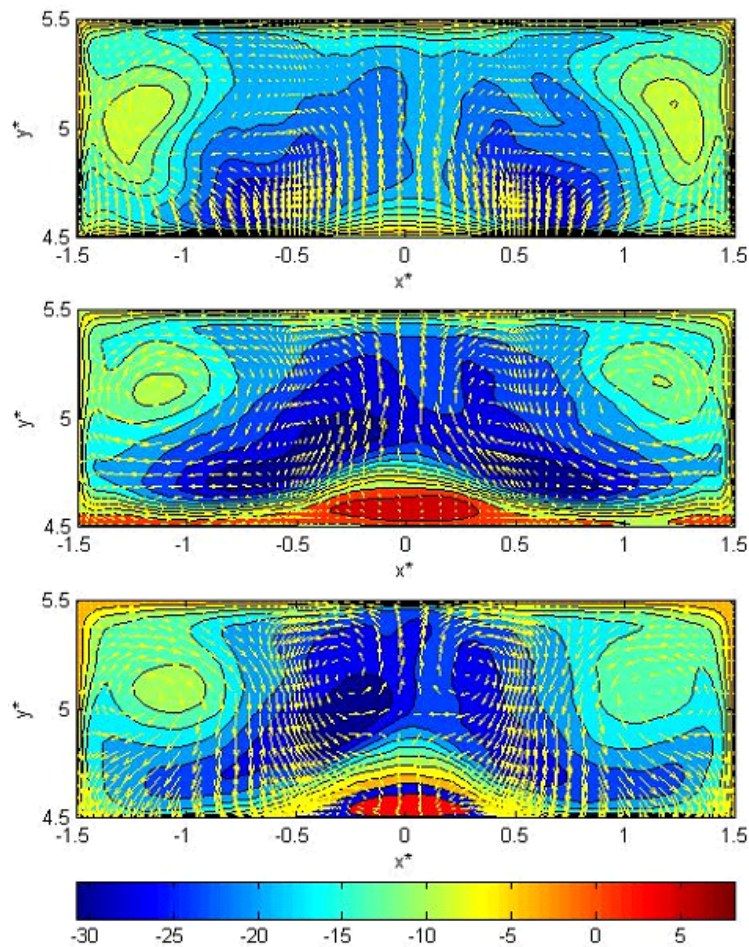
Figure 6.9: Open geometry, $Re = 1.16 \times 10^3$ at plane (x^*, y^*) in the passage channel of PCB model. Numerical mean velocity field (mm/s) for (up to down) $z^* = -1$, $z^* = -1.25$ and $z^* = -1.5$. Vectors u and v component, contours w component.

quasi symmetric counter rotating vortices of the top channel when they arrive at the passage channel the mean velocity field in the plane (x^*, y^*) for different values of z^* is analyzed (Fig. 6.9). In this case the components u and v are vectors and the contours correspond to the component w. At $z^* = -1$, large vortex structures are still well defined and the component values of w indicate that the flow drops faster in the channel central zone. At half height of the passage channel ($z^* = -1.25$) smaller vortex structures appear in the central $x^* = [-0.5, 0.5]$ and the velocity component w has a sign change, close to the plate, which implies the existence of a recirculation. At the end of the passage channel ($z^* = -1.5$) two pairs of quasi symmetric counter rotating vortices of same order, are observed. Figure 6.10 show the numerical mean velocity patterns at the bottom channel for open geometry. The vector representation

58

Figure 6.10: Open geometry, $Re = 1.16 \times 10^3$ at plane (x^*, z^*) in the bottom channel of PCB model. Numerical mean velocity field for (up to down) $y^* = 5$, $y^* = 3.5$, $y^* = 1.5$ and $y^* = 0$. Vectors u and w component, contours v component.

correspond to the components u and w while v component is represented by contours as in the top channel description. In the bottom channel, the larger value of the mean velocity modulus is found in the outlet region $(y^* = 0)$, 72.4×10^{-3} m/s, while in the other studied planes this magnitude is around

59
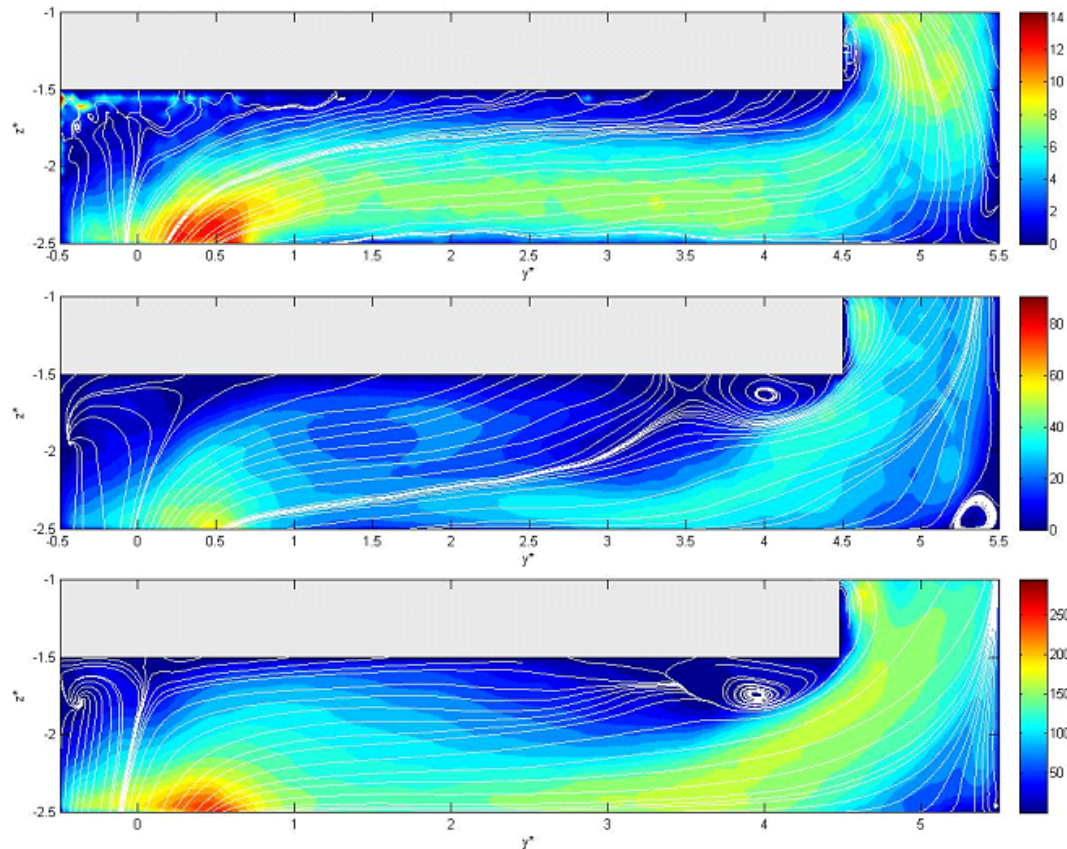
Figure 6.11: Experimental mean velocity field streamlines and modulus (mm/s) throughout the cavity, plane (y^*, z^*) at $x^* = 0$, (up to down) $Re = 300$, $Re = 1.16 \times 10^3$ and $Re = 5.79 \times 10^3$.

(30×10^{-3} m/s. At plane $y^* = 5$ the maximum of u and v components are similar (16.9×10^{-3} m/s to the u component, 13.6×10^{-3} m/s to the v component) whilst the w component is almost double (28.9×10^{-3} m/s). As expected in this plane w is the largest component coinciding with the main flow direction. For planes $y^* = 3.5$ and $y^* = 1.5$ the maximum of u and w components decrease (0.8×10^{-3} m/s to the u component, 0.7×10^{-3} m/s to the w component) while the component v increases (28.6×10^{-3} m/s). These low values of u and w components denotes that no large vortex structures prevails in the flow. The large counter rotating vortices that exist along the top channel cannot survive the change in flow direction required for the flow to go from the top to the bottom channel. In the open geometry there are no means for the flow to re-organize itself resulting on only smaller, weaker, vortical structures created at the bottom channel (Fig. 6.10).

The lack of the helical flow movement at the bottom channel generates a strong recirculation downstream from the leading edge of the plate also

60

obtained by Usera et al. [11]. The existence of this strong recirculation is conditioned by the chosen Reynolds number as Fig. 6.11 shows. For all studied Reynolds numbers, it can be observed an area that stretches from the passage channel to the output one which presents the highest values of mean velocity module. While near the plate are presented lowest values of this magnitude. For $Re = 300$ a small recirculation in the passage channel close to the plate is observed in turn no relevant structure have been found in the enclosure bottom channel. In contrast, for the other values of Re observed the presence of a strong recirculation in the lower channel located at $x^* = [3.5, 4.5]$ and attached to the plate.

Practically the same structures were obtained for all Reynolds numbers of both experimental and numerically. The greatest difference is the passage channel recirculation observed experimentally for $Re = 300$ at $(y^*, z^*) = (4.56, -1.23)$ and that is not present for larger Re, however, numerically this recirculation is present for all Reynolds numbers studied. Figure 6.12 shows
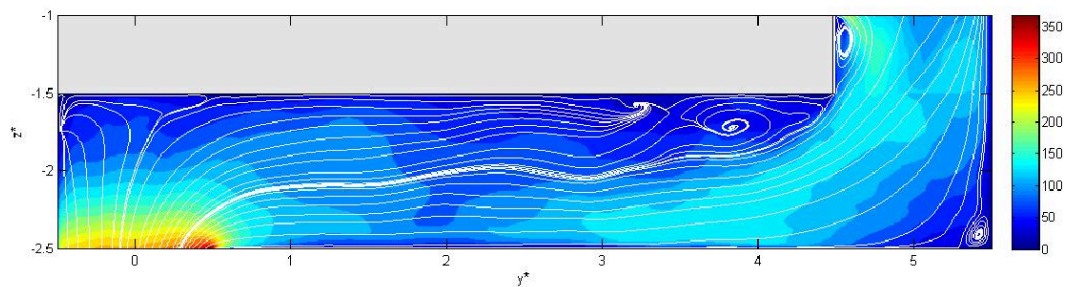
Figure 6.12: Numerical mean velocity field streamlines and modulus (mm/s) throughout the cavity, plane (y^*, z^*) at $x* = 0$ for $Re = 5.79 \times 10^3$.

the numerical mean velocity field and the streamlines for $Re = 5.79 \times 10^3$ where the structures mentioned above can be observed. Both recirculations can lower the heat transfer in those regions and they have to be avoided to prevent undesired localized mechanical wear.

Chapter 7

Unheated closed geometry

This chapter describes the flow behavior in the closed geometry. The temperature conditions and the inlet mean velocity values are de same ones used for the open geometry. That is,the plate that models the PCB has the same temperature as the flow and three different values of the inlet mean velocity are studied. The results are also obtained from both numerical simulation and experimental measurements as for the open geometry case. In this case multi plane experiments have been added in order to analyze the spatial correlation of the flow structures. Will begin by studying the flow behavior for $Re = 1160$
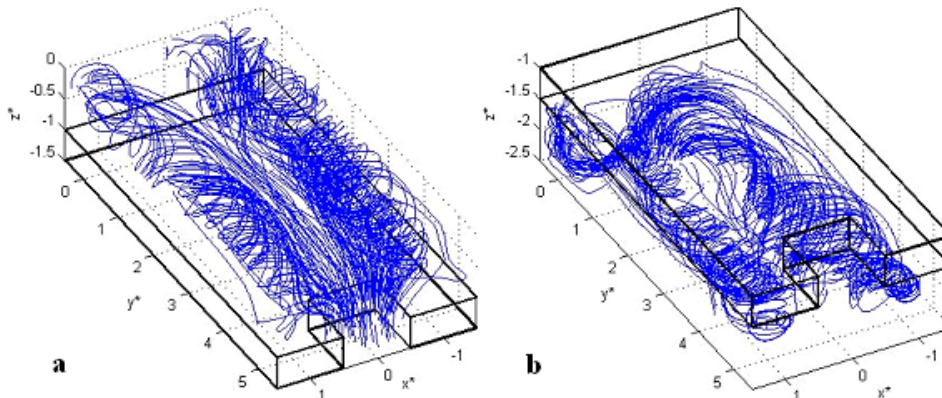
Figure 7.1: 3D streamlines , Re=1.16×10^3, $\boldsymbol{a}$ Top channel,$\boldsymbol{b}$ bottom channel, closed geometry.

by plotting the $3D$ streamlines (Fig 7.1). In the top channel the fluid follows a quasi symmetric double spiral path (Fig 7.1$\boldsymbol{a}$) as in the open geometry case (Fig. 6.1$\boldsymbol{a}$) even in this case the both spirals must come together to get through the passage channel. For the bottom channel the quasi symmetric double spiral path is still present, Fig. 7.1$\boldsymbol{b}$.

Figure 7.2 shows the numerical mean velocity field in the top channel at selected (x^*, z^*) planes (see Fig. 3.14) and illustrates two quasi-symmetric

counter-rotating vortices whose centers moves upwards as the flow move away from the entrance. The vector representation corresponds to the components
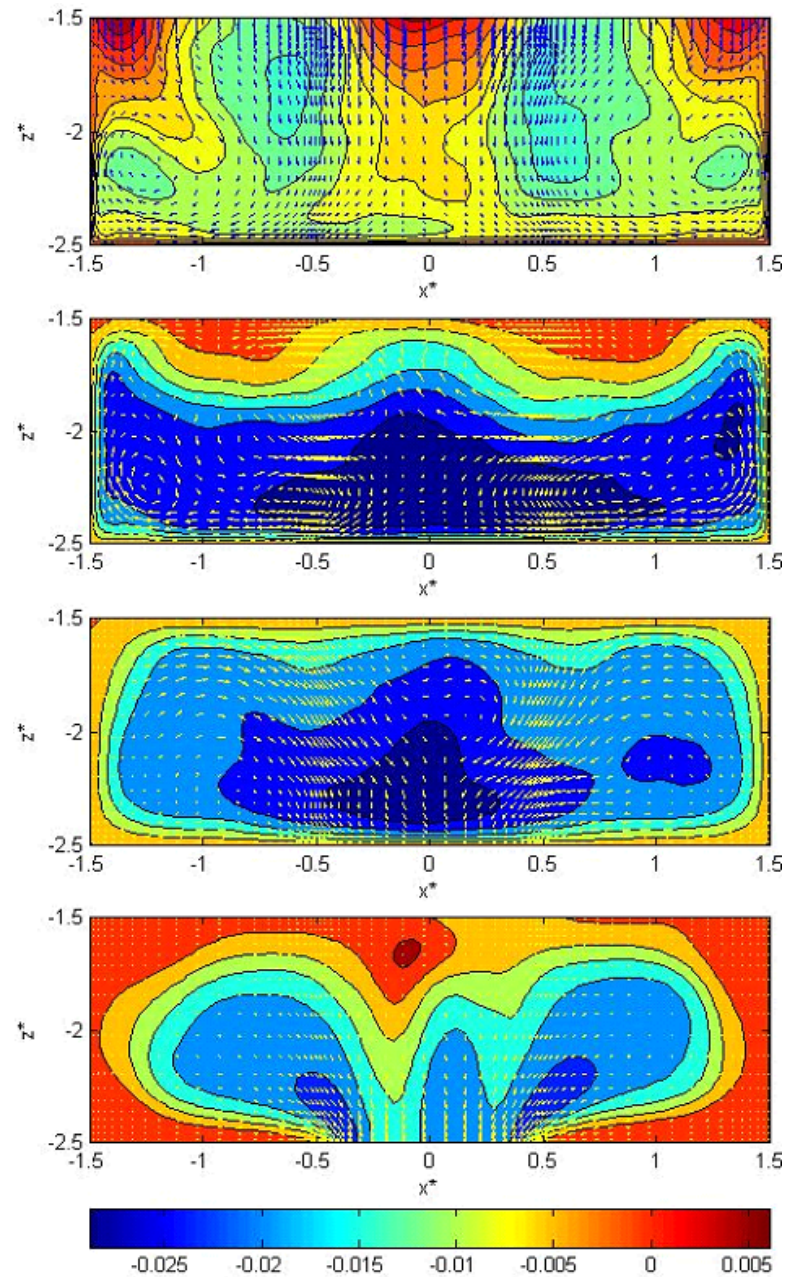

Figure 7.2: $Re = 1.16 \times 10^3$ at plane (x^*, z^*) in the top channel of PCB model. Numerical mean velocity field for (up to down) $y^* = 0$, $y^* = 1.5$, $y^* = 3.5$ and $y^* = 5$. Vectors u and w component, contours v component.

u and w while the v component is represented by contours. The behavior of the flow in the top channel is practically the same as for the open geometry (Fig. 6.3).

The larger velocity vectors are found in the inlet region. Outside that

64

region, on the chosen planes, the maximum of each components of the mean velocity is found at $y^* = 1.5$ where u and w components are similar (45.8×10^{-3} m/s to the u component, 44.8×10^{-3} m/s to the w component) whilst the v component is almost double (83.0×10^{-3} m/s). Note that these values are closed to those obtained in the open geometry. Differences occur at $y^* = 5$, where the influence of the opening is important. Upstream of this location the large scale structures obtained are practically the same. Thus, it can be stated that there is not much influence from the geometry of the PCB in the structures present in the enclosure top channel. This can also be seen observing the contours of the mean velocity modulus at plane (y^*, z^*) for $x^* = 0$, Fig. 7.3. This figure also shows the same two vortex oriented in the x^* direction in
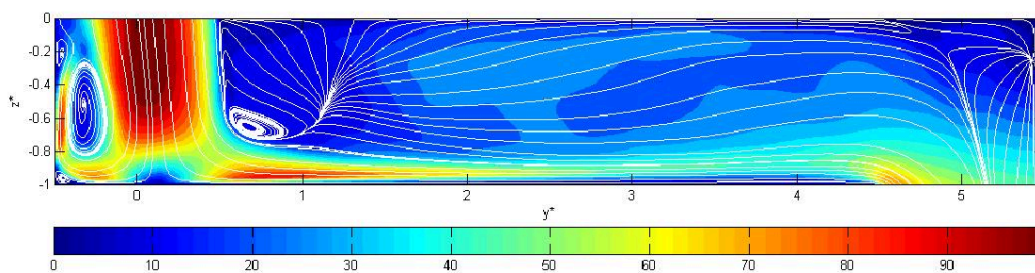
Figure 7.3: Mean velocity field (mm/s), $Re = 1.16 \times 10^3$, plane (y^*, z^*) at $x^* = 0$ in the top channel of PCB model.

the same locations obtained in the open geometry (Fig. 7.3). Some differences appears depend on the Re, for $Re = 300$ and $Re = 5.79 \times 10^3$, the vortex located at $(y^*, z^*) = (0.7, -0.7)$ is no present. For the lowest Re can be seen small additional vortices against the back wall of the cavity, they disappear for the higher Re. In turn, two new recirculations can be seen located at $(y^*, z^*) = (3.94, -0.04)$ and $(y^*, z^*) = (4.13, -0.03)$. The dependence with the Re is also observed in the open geometry.

The influence in the flow structures of the opening is not visible until $y^* = 4.5$, where the mean velocity modulus close to the plate is higher than the one obtained in the open geometry (Fig. 6.4). Experimental results at $Re = (1144 \pm 126)$ (Fig. 7.4) show that the large scale structures found in the top channel are practically the same as those obtained for the numerical simulation (Fig. 7.2). The differences observed at $y^* = 0$ are the same obtained in the open geometry. Thus, in the top channel the bulk flow behavior is not significant different from that obtained for the open geometry for all Re numbers.

To see what happens to the pair of quasi symmetric counter rotating vortices of the top channel when they arrive at the passage channel the mean velocity field in the plane (x^*, y^*) for different values of z^* is analyzed (Fig.
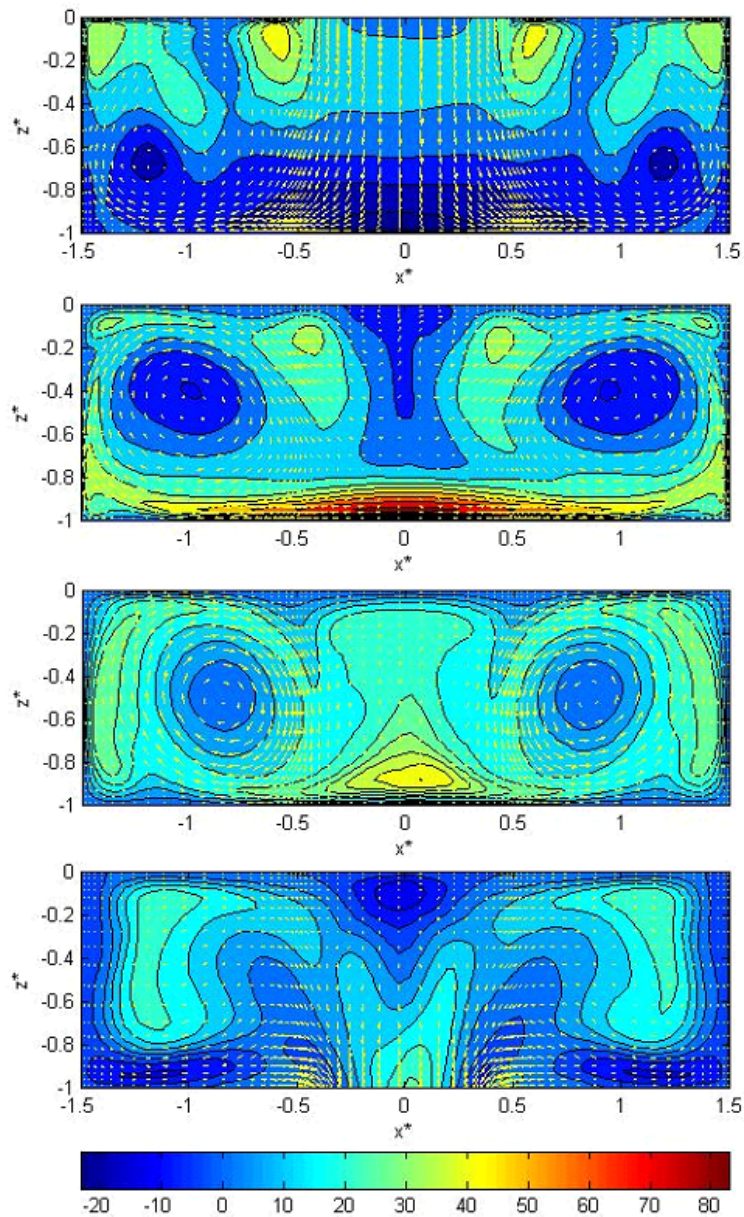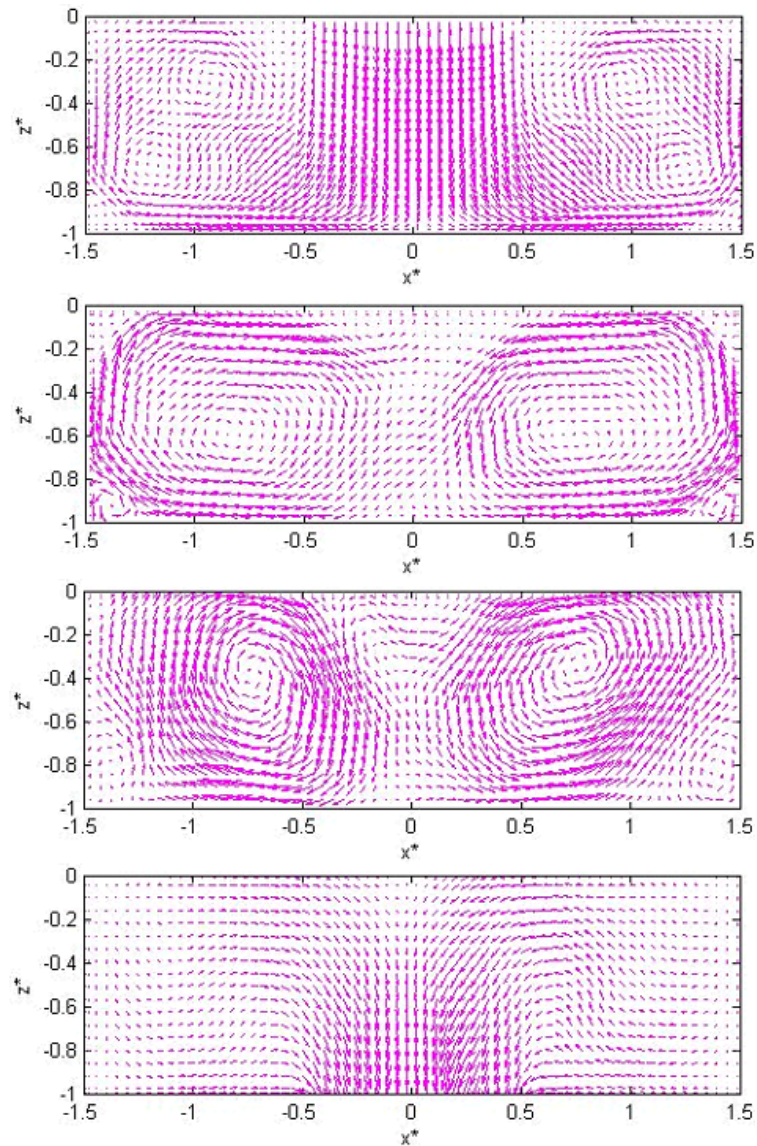
Figure 7.4: $Re = (1144 \pm 126)$ at plane (x^*, z^*) in the top channel of PCB model. Experimental mean velocity field for (up to down) $y^* = 0$, $y^* = 1.5$, $y^* = 3.5$ and $y^* = 5$.

7.5). In this case the components u and v are represented by vectors and the contours correspond to the component w. At $z^* = -1$, a stagnation point is observed located about $(x^*, y^*) = (0, 5.2)$. The component values of w indicate that the flow drops (symmetrically) faster close to the lateral sides of the passage channel. At half height of the passage channel ($z^* = -1.25$) the stagnation point is still present. In addition, a pair of small vortices appears in the corners $(x^*, y^*) = (-0.34, 5.45)$ and $(x^*, y^*) = (0.36, 5.45)$. In the passage channel left part, a pair of counter rotating vortices with centers in $(x^*, y^*) = (-0.29, 5.12)$

66
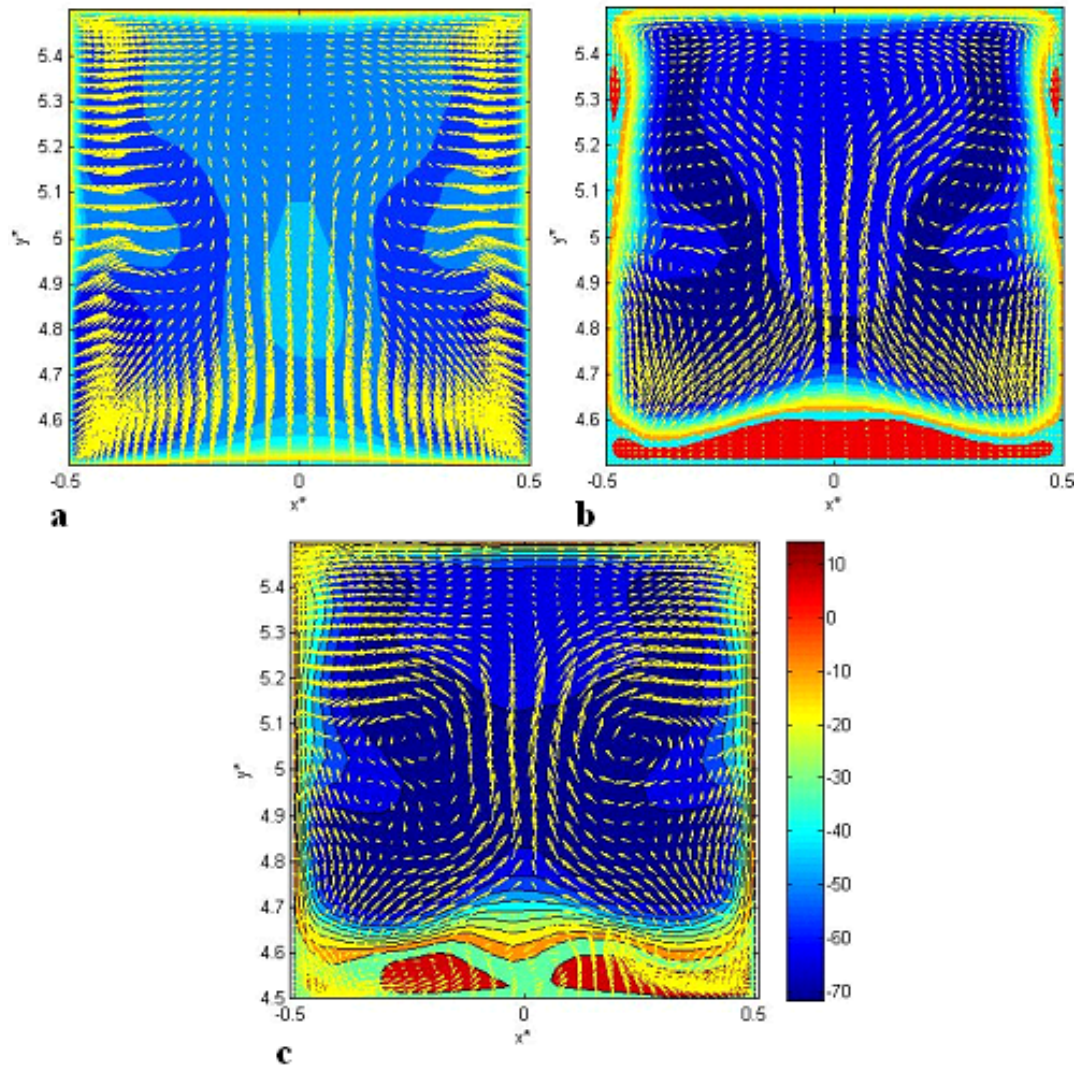
Figure 7.5: $Re = 1.16 \times 10^3$ at plane (x^*, y^*) in the passage channel of PCB model. Numerical mean velocity field (mm/s) for **a** $z^* = -1$, **b** $z^* = -1.25$ and **c** $z^* = -1.5$. Vectors u and v component, contours w component.

and $(x^*, y^*) = (-0.33, 4.91)$ appear, while at the right part only one vortex in $(x^*, y^*) = (0.26, 5.07)$ is defined. Close to the plate the velocity component w has a sign change implying that recirculation occurs as in the open geometry. Furthermore, there are two small symmetric recirculations on the side walls of the passage channel located in the region $y^* = [5.25, 5.38]$. At the end of the passage channel $(z^* = -1.5)$ the stagnation point and the upper corner vortices disappear although a new pair of vortices appears at the bottom corners, $(x^*, y^*) = (-0.33, 4.56)$ and $(x^*, y^*) = (-0.33, 4.60)$. The centers of the vortices on the left part of the passage channel are close than for $z^* = -1.25$

67

while the vortex on the right part is still present and almost in the same place $(x^*, y^*) = (0.24, 5.05)$. For $Re = 600$, the same kind of structures described
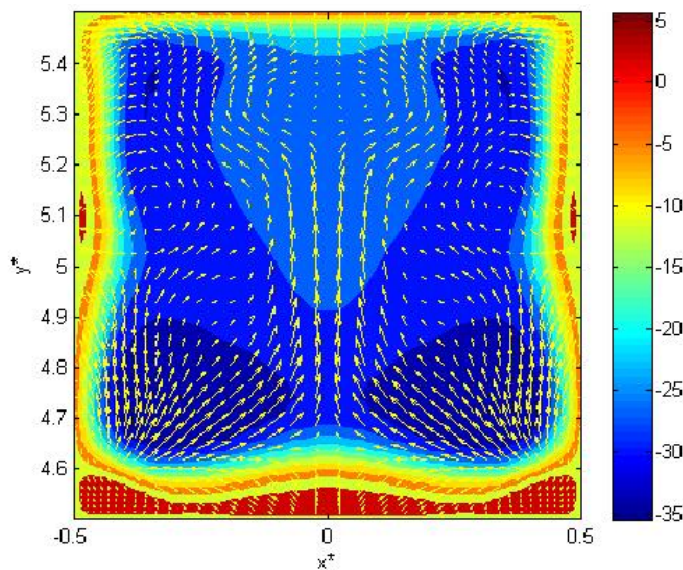
Figure 7.6: $Re = 600$ at plane (x^*, y^*) in the passage channel of PCB model. Numerical mean velocity field (mm/s) for $z^* = -1.25$. Vectors u and v component, contours w component.

above are observed for all $z*$ planes studied. For $z^* = -1.25$ the recirculations in the sidewalls of the channel passage are located in a different position than ones obtained for $Re = 1.16 \times 10^3$. In this case, they are located near the middle of the passage channel ($y^* = [5.05, 5.15]$), Fig. 7.6.

Figure 7.7 shows the numerical mean velocity patterns at the bottom channel. The vector representation corresponds to the components u and w while the v component is represented by contours as in the top channel description. For different Re numbers the large scale structures found in the top channel are practically the same as those shown in Fig. 7.7, although some differences can be found in the structures shape. All flow regimes show large scale structures with a similar general appearance but in some cases they are quasi-circular while in others cases they are oval. Instead, the larger velocity vectors, like in Fig. 6.3, are found in the input region. In this case the maximum for each components of the mean velocity is found at $y^* = 3.5$ being the u and w components are similar to those obtained in the top channel at plane $y^* = 1.5$ ($u = 45.3 \times 10^{-3}$ m/s, $w = 37.0 \times 10^{-3}$ m/s), while the v component is slightly lower ($v = 62.6 \times 10^{-3}$ m/s). As expected v is the largest component coinciding with the main flow direction.

Experimental results at $Re = (1144 \pm 126)$ (Fig. 7.8) show that the large scale structures found in the bottom channel are very closed to those obtained for the numerical simulation (Fig. 7.7). In the plane $y^* = 0$ the vortices
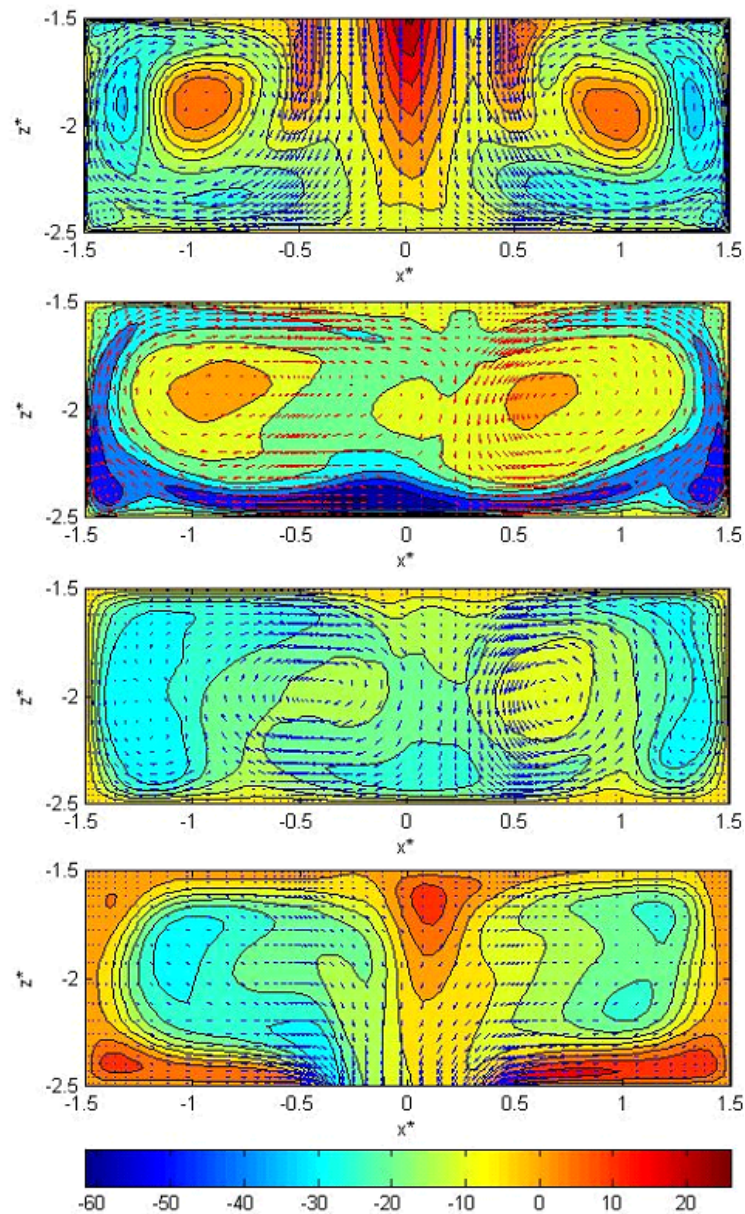
Figure 7.7: $Re = 1.16 \times 10^3$ at plane (x^*, z^*) in the bottom channel of PCB model. Numerical mean velocity field for (up to down) $y^* = 5$, $y^* = 3.5$, $y^* = 1.5$ and $y^* = 0$. Vectors u and w component, contours v component.

centers are located in similar positions, $(x^*, z^*) = (-0.88, -1.93)$ and $(x^*, z^*) = (0.84, -1.88)$ obtained by numerical simulations and $(x^*, z^*) = (-0.88, -1.84)$ and $(x^*, z^*) = (0.99, -1.80)$ for experimental results. Furthermore, a pair of small vortices can be seen in the lower corners, these vortices are maintained at planes $y^* = 3.5$ and $y^* = 1.5$, these structures are also obtained in numerical simulations.

69

Figure 7.8: $Re = (1144 \pm 126)$ at plane (x^*, z^*) in the bottom channel of PCB model. Experimental mean velocity field for (up to down) $y^* = 5$, $y^* = 3.5$, $y^* = 1.5$ and $y^* = 0$.

Some differences can be found in the structures shape in plane $y^* = 3.5$ for $Re = 300$ where a smaller pair of counter rotating vortices appear in the center as Fig. 7.9 shown. Vortices located at $(x^*, z^*) = (-0.15, -1.58)$ and $(x^*, z^*) = (-0.145, -1.58)$ can be observed, the rotation direction of these small vortices is opposite to the ones in the large vortices. Note that these small vortices are located in similar positions than the ones obtained in the

70

top channel at plane $y^* = 1.5$ in the open geometry, se Fig. 6.8.

The flow contraction at the passage channel results in a jet impinging onto the bottom channel lower surface that leads to the creation of two new large counter rotating vortices. Therefore, the strong recirculation (Fig. 6.11, at $x^* = [3.5, 4.5]$ and attached to the plate) present in the bottom channel for the open geometry is not present. Figure 7.10 shows the numerical mean velocity
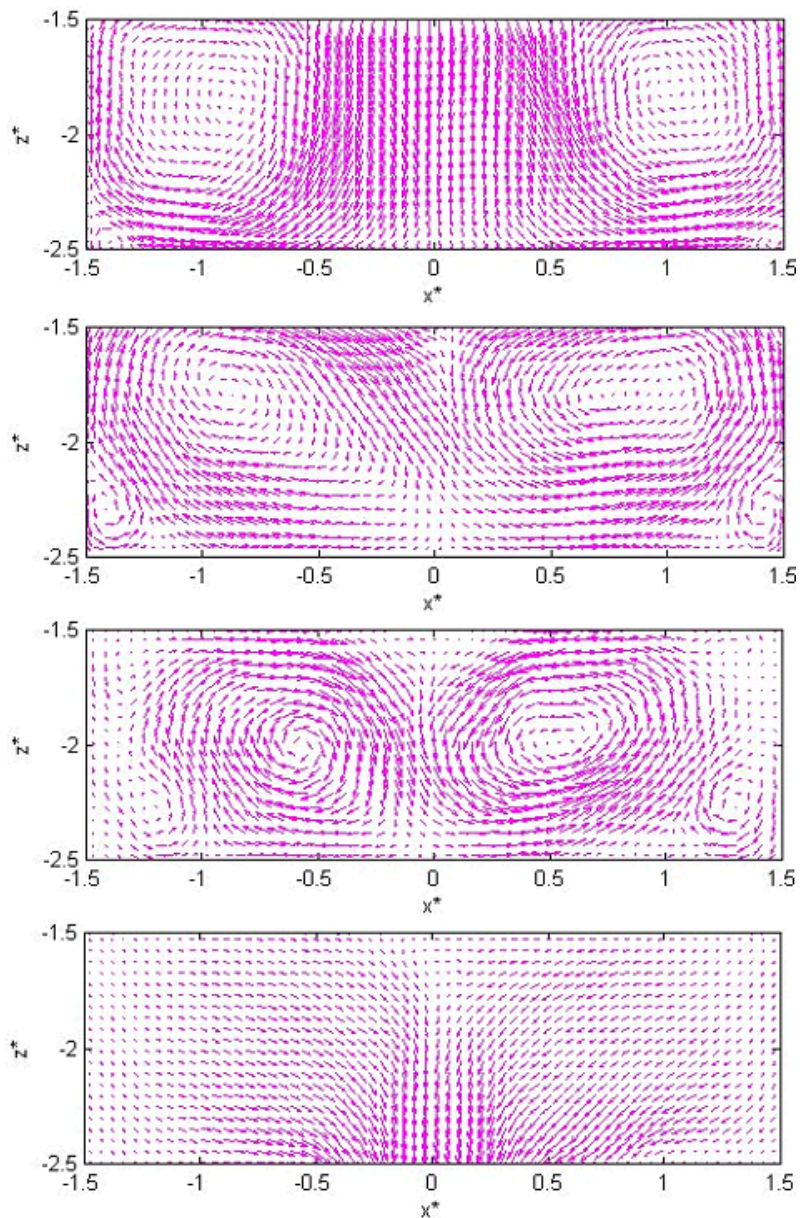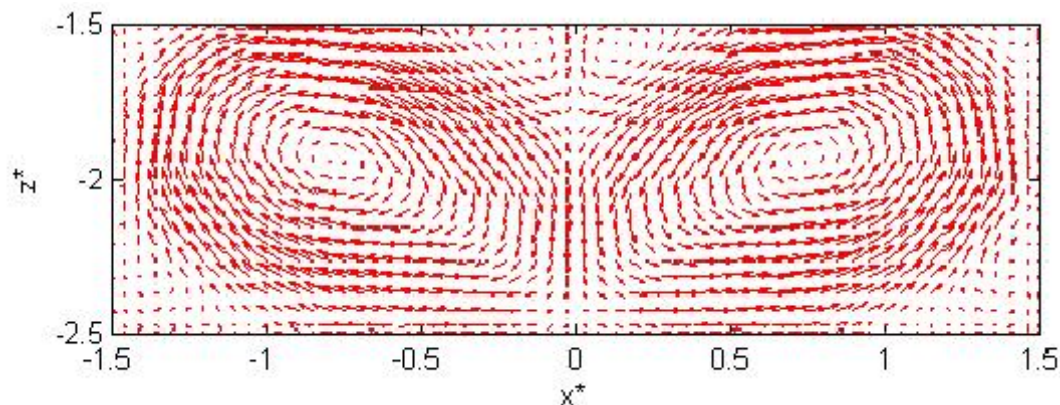

Figure 7.9: $Re = 300$ at plane (x^*, z^*) in the bottom channel of PCB model. Experimental mean velocity field for $y^* = 1.5$

field and the streamlines for $Re = 600$, $Re = 1.16 \times 10^3$ and $Re = 5.79 \times 10^3$ where a small recirculation in the passage channel close to the plate is observed as for the open geometry (Fig. 6.12). At the bottom channel, for $Re = 600$ and $Re = 5.79 \times 10^3$, a recirculation occurs in the lower right corner as the flow hits the cavity wall, being similar to the one observed at the top channel (Fig. 7.3). The corner recirculation is feeble for $Re = 1.16 \times 10^3$. The most relevant structure found in the enclosure bottom channel is the recirculation near the plate located at $(y^*, z^*) = (-0.31, -1.61)$ present for $Re = 5.79 \times 10^3$ as these recirculations close to the plate could affect the heat transfer.

Another comparison between the top and bottom behavior can be done by analyzing the mean velocity v component profiles for selected (x^*, y^*) locations. In the case of $Re = 5.79 \times 10^3$ (Fig. 7.11) the highest mean velocity values are found in the bottom of both enclosure channels. Even that similar behavior is seen at lower z^* of bottom channel where the mean velocity have the same values that the ones obtained in the same location for the top channel. Figure 7.11a and 7.11 d shows a central symmetry between the top and bottom left (right) vortex location like Fig. 7.11b and 7.11 c. This implicates that the flow behavior at the top and bottom channel entrances are similar.
It is also interesting to observe the evolution of the cores. In the numerical domain cross section for $Re = 600$, (Fig. 7.12a) one can observe that the vertical

71
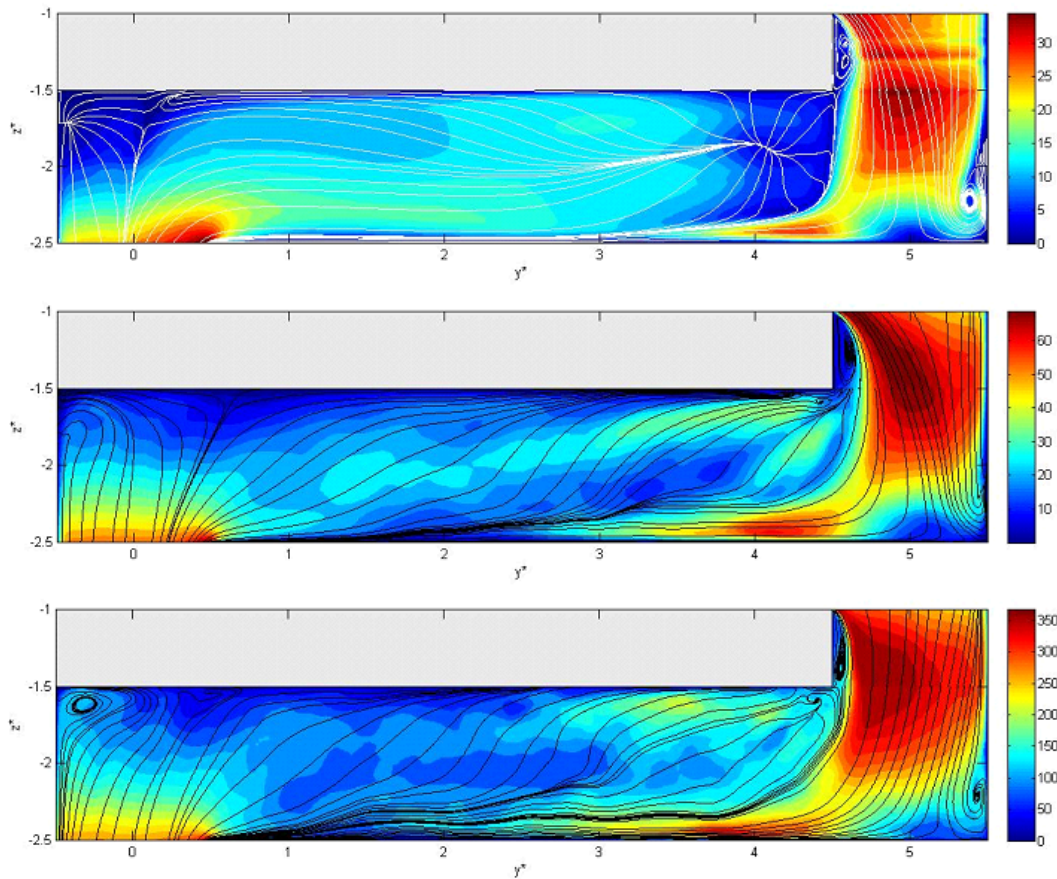
Figure 7.10: Numerical mean velocity field streamlines and modulus (mm/s) throughout the cavity, plane (y^*, z^*) at $x^* = 0$ for (up to down) $Re = 600$, $Re = 1.16 \times 10^3$ and $Re = 5.79 \times 10^3$.

location of the cores (z^*) is practically the same for the right and left vortex for both top and bottom channels. Figure 7.12**b** shows the horizontal location (x^*) of the vortex centers (right and left vortices) display mirror symmetry with respect to $x^* = 0$ in each channel. In the top channel, the centers of the vortices tend to go towards the cavity walls and then go to the center, staying almost in the same position along the channel. In the bottom channel, the horizontal position of the centers is initially at x = 0.93, reaching the value $x^* = 0.66$ (at $y^* = 2$) remaining constant to the end of the channel.

To observe space and time evolution of the dynamic structures of the flow the PIV multi plane was implemented (section 2.3). The measurements were obtained at Reynolds number of Re = 613 based on the input section mean velocity, corresponding to $U_0 = 2.5 \times 10^{-2}$ m/s with the closed geometry plate. Fig.3.13 shows the location of the measurements planes. One of them remains fixed for all the measurement series while the position of the second is changed.

72
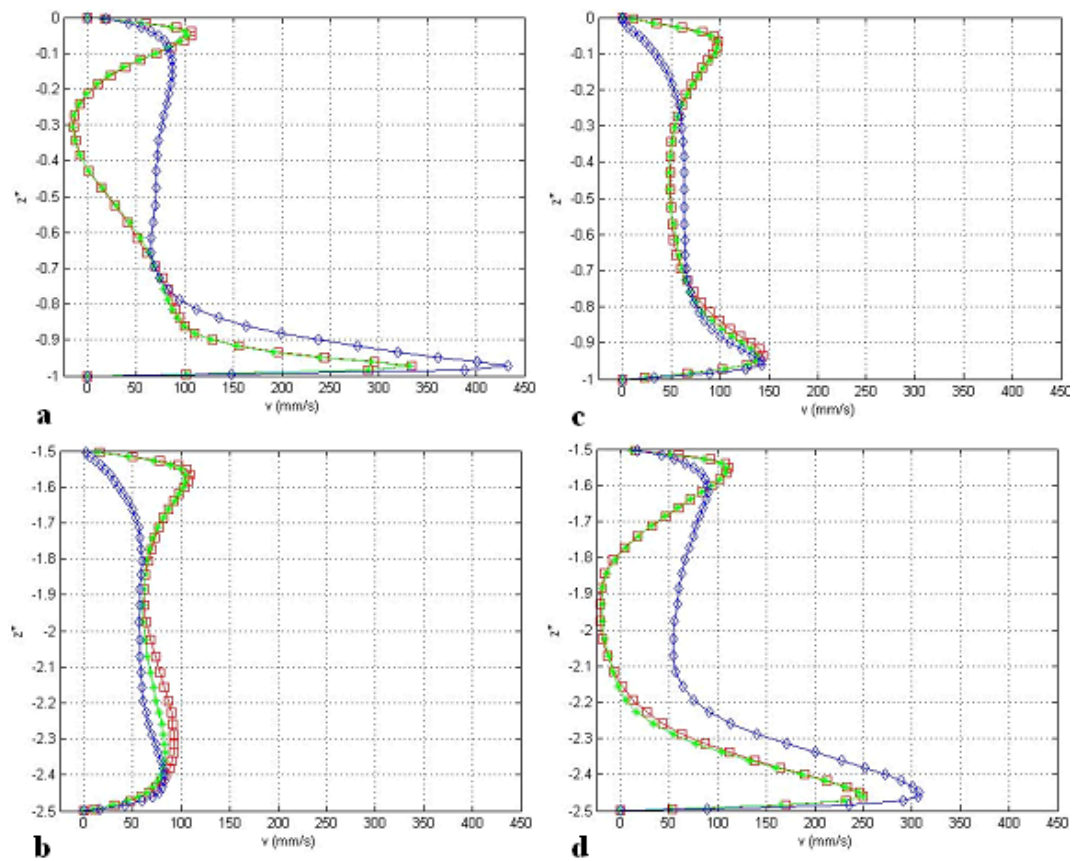
Figure 7.11: Closed geometry, Re=5.79×10^3, v component vs. z^* at $y^* = 1.5$, **a** Top channel, **b** bottom channel, at $y^* = 3.5$, **c** Top channel, **d** bottom channel of PCB model and $x^* = -0.75$ (red squares), $x^* = 0$ (blue diamonds), $x^* = 0.75$ (green stars).
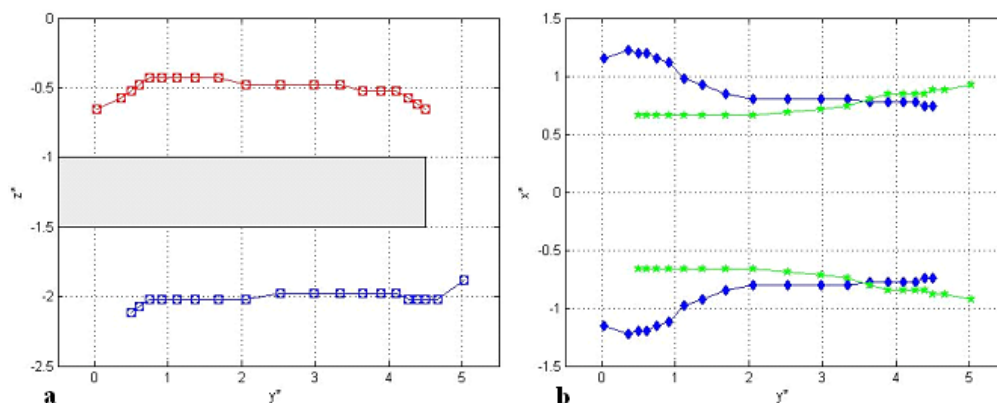
Figure 7.12: Closed geometry, Re=600. Centers position, **b** Vertical, right vortex (squares), left vortex (circles), **b** Horizontal, top channel (blue diamonds), bottom channel (green stars).

The fixed plane was located at $y^* = 4$ and the mobile plane was located at $y^* = 3.5, 3$ and 2. A total of three series of experiments were performed. In each series a measure of the velocity field at $y^* = 4$ was taken.

The mean velocity fields for both fixed and mobile planes were equivalent to those obtained experimental and numerically for the top channel shown in Fig. 7.4 and 7.2. The biggest difference among the three averages was the location of the two vortex centers, moving upwards as the flow moves away from the entrance. It was observed that the horizontal (x) location of the vortex centers do not change significantly as Fig. 7.13 shows. Thus, the large scale flow structure present in the upper part of the PCB model must be a symmetric double counter-rotating vortex tube. The fact that two different planes were recorded simultaneously in time allows a more detailed analysis of the temporal-spatial evolution of the flow structures.

Fig. 7.14 and 7.15 shows the temporal correlation for the experimental series measuring at $y^* = 2$ and $y^* = 4$. Auto-correlation (Fig. 7.14) of the velocity data obtained at both positions indicated the existence of some periodicity in flow structures and that the difference among the instantaneous patterns is small, since the correlation coefficients are of the order of 0.8 for $y^* = 2$ and larger than 0.7 for $y^* = 4$. Fig. 7.15 also gives evidence of the temporal relation between flow structures in the two spatial locations analyzed. Correlation coefficients are still large (about 0.6 for small times) but are slightly reduced with time. The periodic behavior shown in Fig. 7.14 is also present in the Fig. 7.15. This could be explained thinking that the periodical structures passing through the $y^* = 2$ plane travels to the plane $y^* = 4$, although the individual flow structure has small changes as it travels causing a reduction on the correlation coefficients.

74
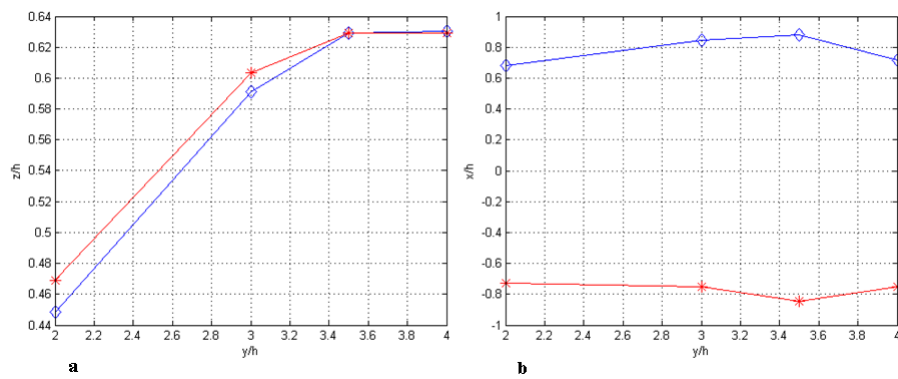
Figure 7.13: Location of the vortex center **a** vertical **b** horizontal.
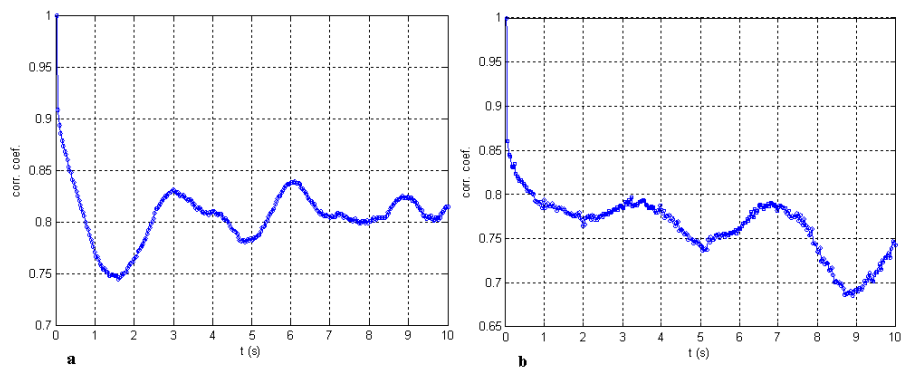
Figure 7.14: Auto-correlation function **a** $y^* = 2$, **b** $y^* = 4$.
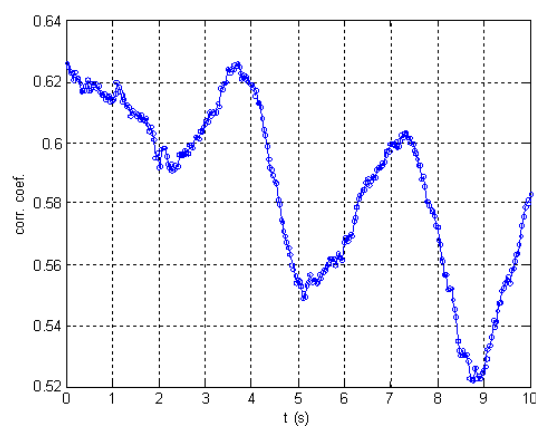
Figure 7.15: Cross-correlation function between flow structures at $y^* = 2$ and $y^* = 4$.

Chapter 8

Temperature influence in the system

In all results presented in this section shall be considered that the plate that models the PCB is heated and the fluid is maintained at a constant temperature.

In numerical simulations the results presented in section 4.4 were taken into account, so for a temperature difference of $\Delta T = 10°$ C the variations in physical properties are negligible.

The fluid temperature was set at $T_c = 20°$ C while the plate temperature was $T_h = 30°$ C in one case and $T_h = 50°$ C in other, thus obtaining temperature differences of $\Delta T = 10°$ C and $\Delta T = 30°$ C.

Experimental results were obtained for $Re = 300$, $Re = 1.16 \times 10^3$ and $Re = 5.79 \times 10^3$ only for the open geometry considering both temperature differences. In turn, the numerical results were obtained for the same Reynolds numbers for both open and closed geometry. The temperature difference was considered $\Delta T = 10°$ C. Only for the higher Re, numerical results were obtained considering a temperature difference $\Delta T = 30°$ C, which involves considering the physical properties dependent on temperature.

8.1 Flow behavior

8.1.1 Open geometry

Figure 8.1 shows the numerical mean velocity field in the top channel at selected (x^*, z^*) planes at $Re = 5.79 \times 10^3$ and $\Delta T = 10°$ C. The figure shows that the large scale structures found in the top channel are practically the same as those obtained for the numerical simulations for the open and closed geometries when the plate that models the PCB not heated (Figs. 6.3 and 7.2). The vector representation corresponds to the components u and w while the v component of the mean velocity is represented by contours.

77

Experimental results at $Re = (5735 \pm 630)$ (Fig. 8.2) show that the large scale structures found in the top channel are mostly the same as those obtained for the numerical simulation (Fig. 8.1). At planes $y^* = 3.5$ and $y^* = 1.5$ a

Figure 8.1: $Re = 5.79 \times 10^3$ and $\Delta T = 10°$ C at plane (x^*, z^*) in the top channel of PCB model. Numerical mean velocity field for (up to down) $y^* = 0$, $y^* = 1.5$, $y^* = 3.5$ and $y^* = 5$. Vectors u and w component, contours v component.

pair of small vortices can be seen in the lower corners, these structures are obtained experimental and numerically. Observing the mean velocity fields in the plane $y^* = 5$ for experimental and numerical results we can see that they

78

are quite similar although the experimental results are slightly more "disordered" especially in the center of the plane ($-0.5 > x^* > 0.5$), as happened when no temperature difference between the plate and the fluid was considered (Fig. 6.7). Nevertheless, some differences between numerical and experimen-
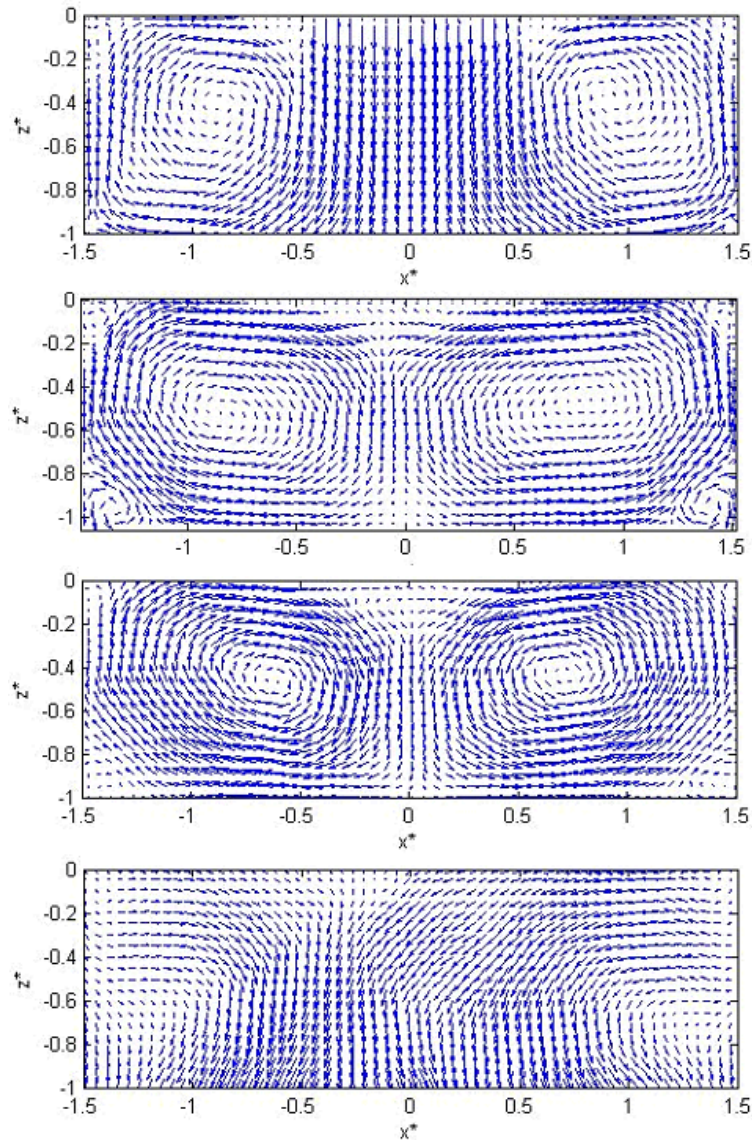
Figure 8.2: $Re = 5.79 \times 10^3$ and $\Delta T = 10°$ C at plane (x^*, z^*) in the top channel of PCB model. Experimental mean velocity field for (up to down) $y^* = 0$, $y^* = 1.5$, $y^* = 3.5$ and $y^* = 5$. Vectors u and w component.

tal results can be observed at $y^* = 0$, which show that the vortices centers obtained numerically are located closer to the cavity lateral walls and to the plate, $(x^*, z^*) = (-1.05, -0.60)$ and $(x^*, z^*) = (1.1, -0.64)$, than those obtained experimentally $(x^*, z^*) = (-0.89, -0.40)$ and $(x^*, z^*) = (0.89, -0.35)$.

8. TEMPERATURE INFLUENCE IN THE SYSTEM

Vortical structures presented at $Re = 5.79 \times 10^3$ are not significantly different from that obtained at $Re = 1.16 \times 10^3$.
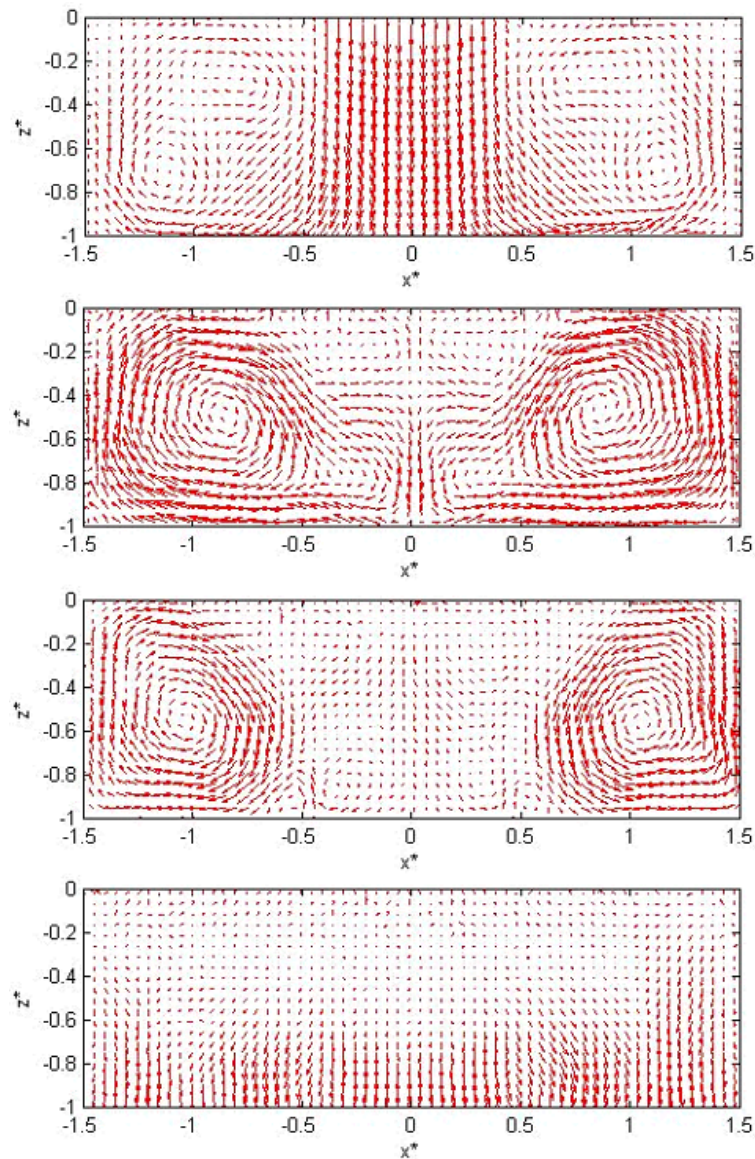
Figure 8.3: $Re = 300$ and $\Delta T= 10°$ C at plane (x^*, z^*) in the top channel of PCB model. Experimental mean velocity field for (up to down) $y^* = 0$, $y^* = 1.5$, $y^* = 3.5$ and $y^* = 5$. Vectors u and w component.

This is the case when comparing the vortical structures at $Re = 300$ and $\Delta T= 10$ ° C. Both numerically and experimentally results show important differences with the case where the temperature is homogeneous. Figure 8.3 show the experimental mean velocity field for $Re = 300$ and $\Delta T= 10°$ C in the top channel. In the plane $y^* = 1.5$ the pair of small quasi symmetry

counter rotating vortices situated in the center are still present (see Fig. 6.8) and are located at the $(x^*, z^*) = (-0.18, -0.18)$ and $(x^*, z^*) = (0.34, -0.20)$. While the bigger quasi symmetry counter rotating vortices appear somewhat
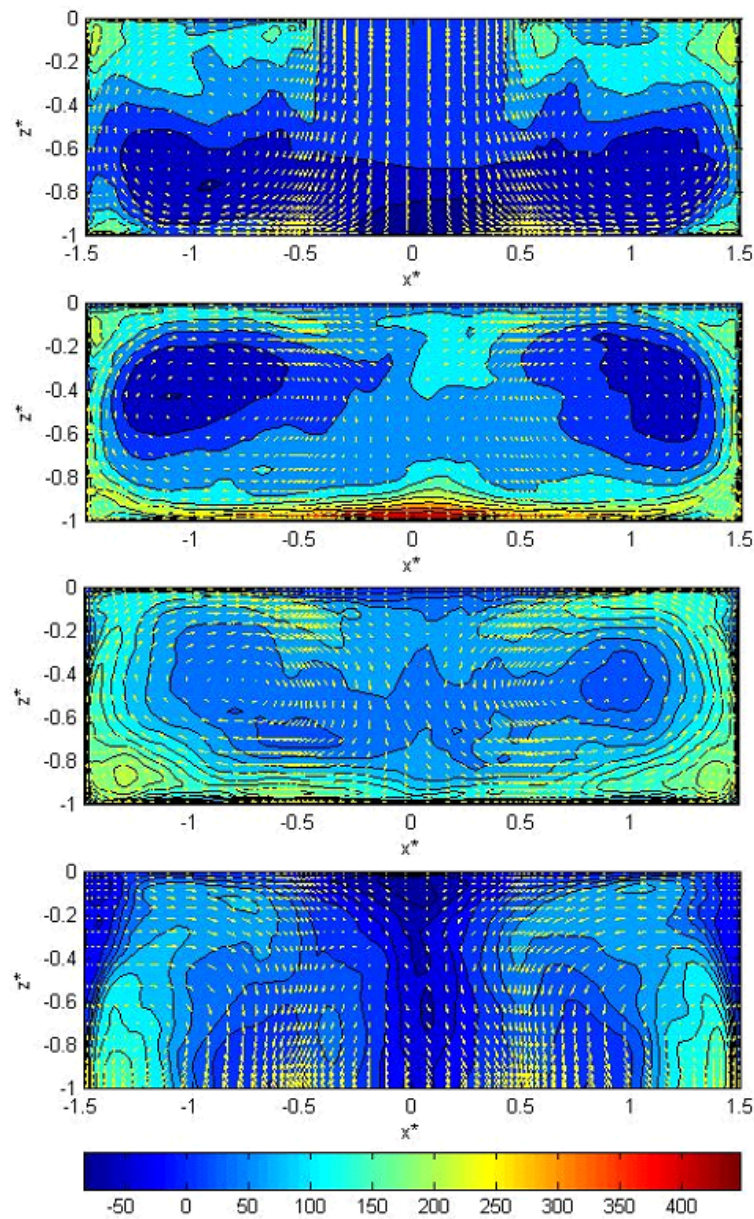

Figure 8.4: $Re = 300$ and $\Delta T = 10°$ C at plane (x^*, z^*) in the top channel of PCB model. Numerical mean velocity field for (up to down) $y^* = 0$, $y^* = 1.5$, $y^* = 3.5$ and $y^* = 5$. Vectors u and w component, contours v component.

distorted in the central zone of the cavity. The vortex structures present in the plane $y^* = 3.5$ are less defined than in the plane $y^* = 1.5$, these are spread

81

8. TEMPERATURE INFLUENCE IN THE SYSTEM

over the channel height and in turn concentrated in the central area of this ($x^* = [-0.5, 0.5]$). The large vortical structures have been displaced toward the side walls of the cavity. Their centers being found at $(x^*, z^*) = (-1.04, -0.55)$ and $(x^*, z^*) = (1.04, -0.57)$.

Numerical mean velocity fields for $Re = 300$ and $\Delta T = 10°$ C in the top channel are shown in Fig. 8.4. The structures obtained by numerical simulations in the plane $y^* = 1.5$ are similar than the ones obtained experimentally. In the plane $y^* = 3.5$, have been found that the structures present in the enclosure top channel have radically changed. Instead of a pair of quasi symmetry counter rotating vortices occupying all the top channel, have been observed two pairs of them. The pair of vortices which existed at the previous planes now occupies less space and their centers are displaced toward the cavity lateral walls, this behavior has also been observed experimentally. In the central area of the cavity ($x^* = [-0.5, 0.5]$), a pair of well-defined quasi symmetry counter rotating vortices are observed, unlike the one experimentally observed in the same zone the present vortex structures are more diffuse. From the
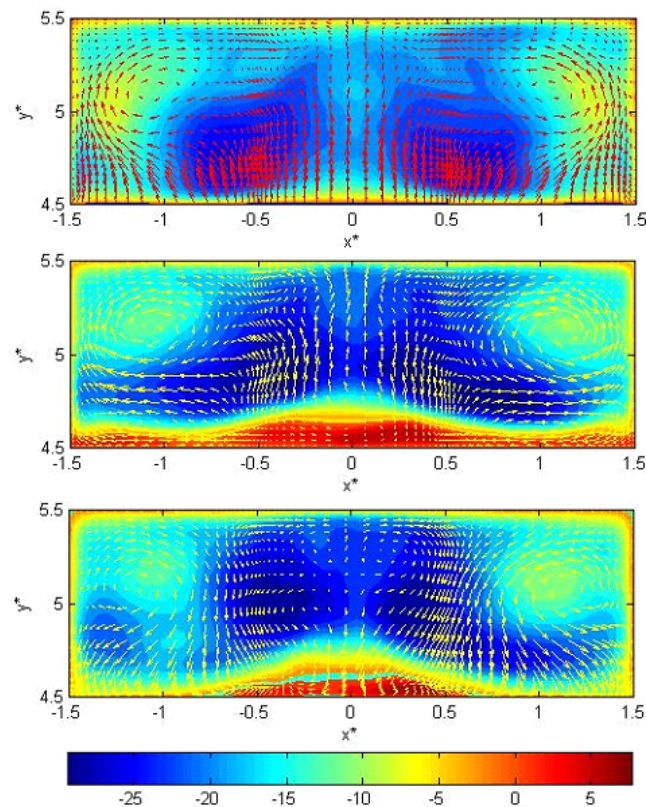
Figure 8.5: $Re = 1.16 \times 10^3$ at plane (x^*, y^*) in the passage channel of PCB model, open geometry. Numerical mean velocity field (mm/s) for **a** $z^* = -1$, **b** $z^* = -1.25$ and **c** $z^* = -1.5$. Vectors u and v component, contours w component.

82

results obtained for the open geometry in the top channel of the cavity can be seen that considering a temperature difference between the plate and the fluid has more influence on the structures that the Reynolds number (inlet velocity). Furthermore can be seen that the temperature influence on the structures shape and evolution is greater than the lower the Reynolds number.

Figure 8.5 shows the mean velocity field in the plane (x^*, y^*) for different values of z^* at the passage channel. Where the components u and v are vectors and the contours correspond to the component w. At planes $z^* = -1$ and $z^* = -1.25$ the structures do not exhibit significant differences compared to those obtained when no temperature difference is considered between the plate and the fluid. The most notable difference is present at $z^* = -1.25$ where the recirculation closed to the plate (component w sign change) is less localized. This also occurs at the end of the passage channel ($z^* = -1.5$) where besides the vortical structures located at $x^* = [-0.5, 0.5]$ are weaker and less defined than those obtained previously (Fig. 6.9).

Figure 8.6 show the numerical mean velocity patterns at the bottom channel for open geometry. The vector representation correspond to the components u and w while v component is represented by contours as in the top channel description. The large counter rotating vortices that exist along the top channel cannot survive the change in flow direction required for the flow to go from the top to the bottom channel. In the open geometry there are no means for the flow to re-organize itself resulting on only smaller, weaker, vortical structures created at the bottom channel (Fig. 8.6). It is also confirmed by the experimental results. Figure 8.7 show the experimental mean velocity field for $Re = 5735 \pm 630$. In this way, the structures present in the enclosure bottom channel when considering a temperature difference $\Delta T = 10°$ C are not different from those obtained for the case of $\Delta T = 0°$ C.

Another way to see the influence of temperature on the flow structures is through the mean velocity field modulus and the streamlines in the planes (y^*, z^*) at $x^* = 0$.

The experimental results presented in Figure 6.11 show the existence of a strong recirculation close to the plate in the bottom channel depends on the chosen Reynolds number. For $Re = 300$ in the case where there is no temperature difference between the plate and the fluid, a localized recirculation was observed in the passage channel while in the bottom channel no relevant structure was present.

For this Reynolds number the change in the flow structures is evident by introducing a temperature difference between the plate and the fluid, both for $\Delta T = 10°$ C and $\Delta T = 30°$ C. In both cases the mean velocity field modulus shows that in the passage channel has a high velocity zone that extends into the bottom channel like a tongue, leaving low velocities in the area near plate, as Fig. 8.8 shown. For the case with $\Delta T = 10°$ C we note that this area is among the regions $3.5 \geq y^* \geq 4.95$ and $-1 \geq z^* \geq -1.9$ presenting two
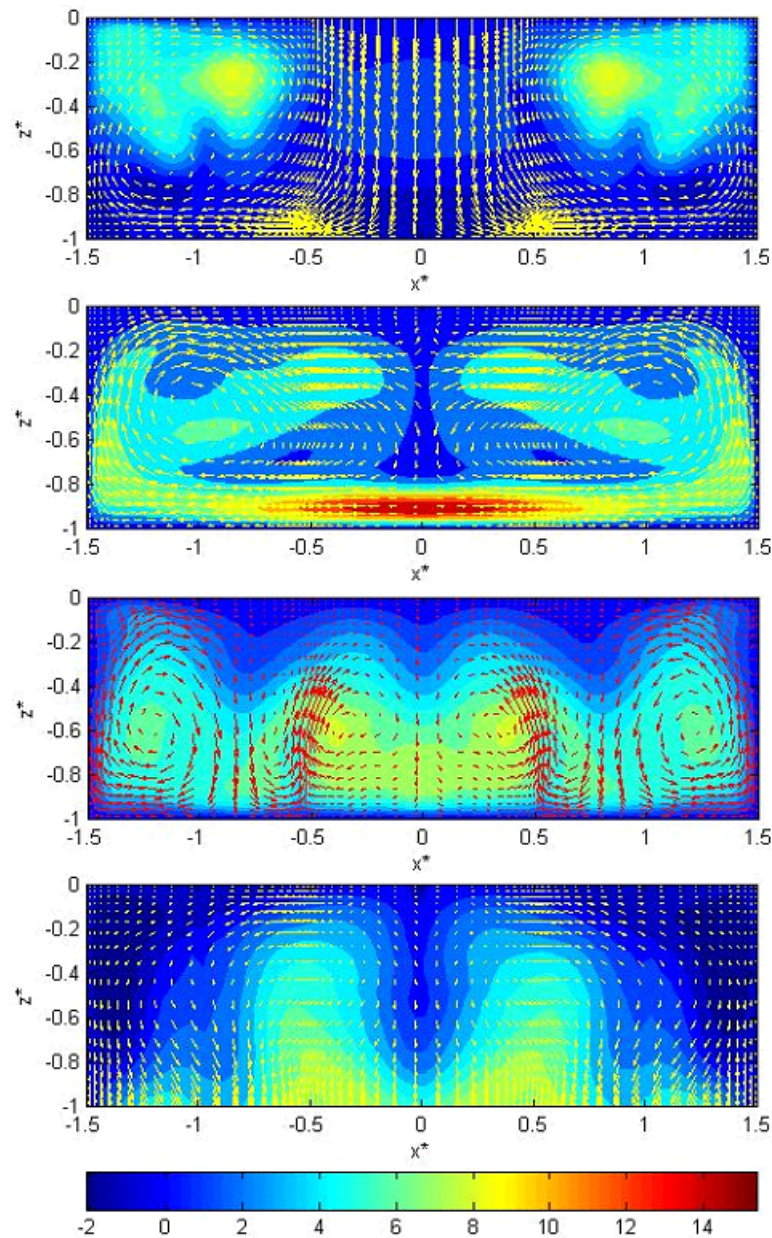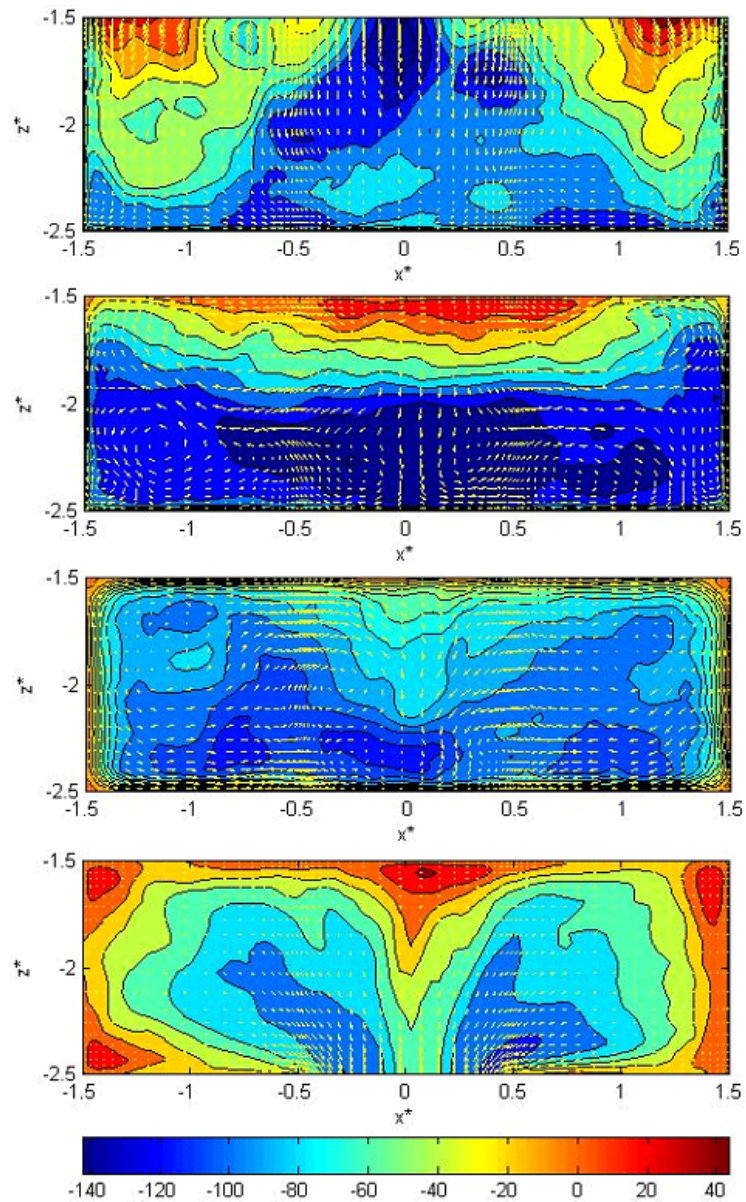
Figure 8.6: $Re = 5.79 \times 10^3$ and $\Delta T= 10°$ C at plane (x^*, z^*) in the top channel of PCB model. Numerical mean velocity field for (up to down) $y^* = 5$, $y^* = 3.5$, $y^* = 1.5$ and $y^* = 0$. Vectors u and w component, contours v component.

stagnation points. One of them is situated in the channel passage at $(y^*, z^*) = (4.64, -1.33)$, whereas the other is located in the bottom channel $(y^*, z^*) = (4.11, -1.8)$.

When the temperature difference is $\Delta T= 30°$ C the low velocities area is more extensive localized in $3.35 \geq y^* \geq 5.1$ and $-1 \geq z^* \geq -2.1$. Any stagnation point is observed in the passage channel while in the bottom channel
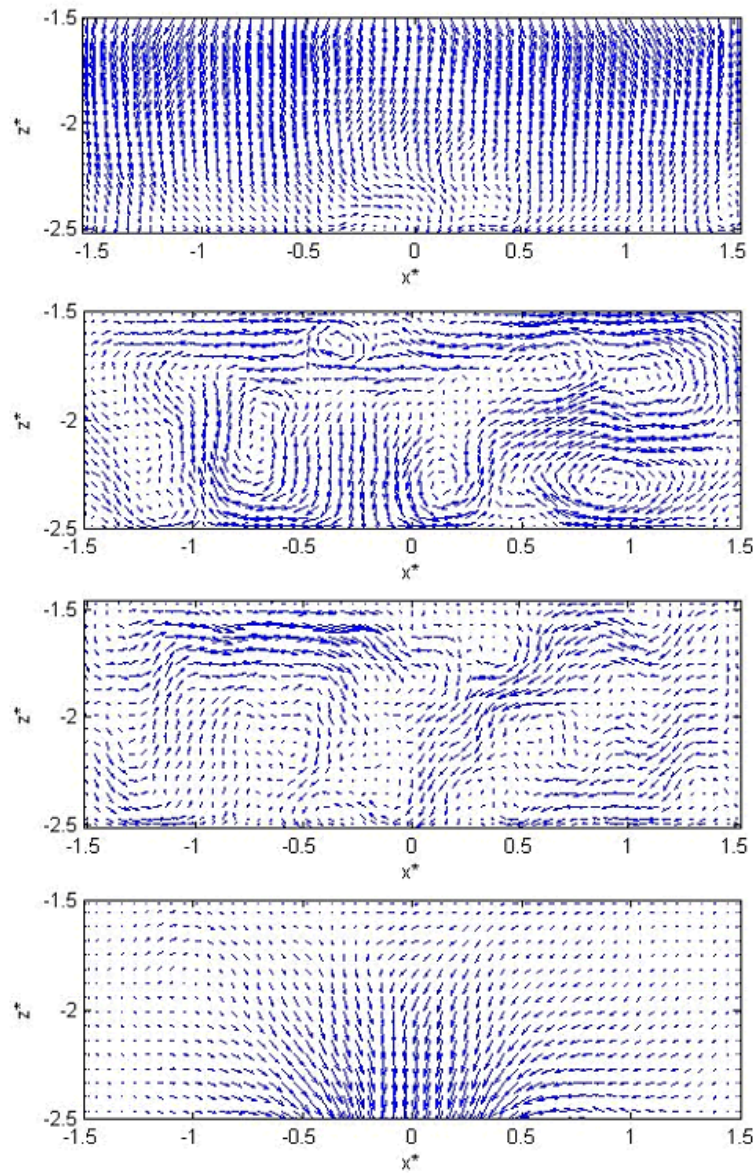
Figure 8.7: $Re = 5.79 \times 10^3$ and $\Delta T = 10°$ C at plane (x^*, z^*) in the top channel of PCB model. Experimental mean velocity field for (up to down) $y^* = 5$, $y^* = 3.5$, $y^* = 1.5$ and $y^* = 0$. Vectors u and w component.

a stagnation point at $(y^*, z^*) = (3.83, -1.80)$ and a recirculation at $(y^*, z^*) = (4.21, -1.98)$ are present. This recirculation is less important than those obtained for higher Reynolds numbers, e.i. Fig. 6.11, because it is not adjacent to the plate. The flow structures observed for $Re = 1.16 \times 10^3$ when no temperature difference between the plate and the fluid is regarded are the same as those obtained when temperature difference of $\Delta T = 10°$ C and $\Delta T = 30°$ C are taken into account, Fig. 8.9.

Figure 8.8: Experimental mean velocity field streamlines and modulus (mm/s) throughout the cavity, plane (y^*, z^*) at $x^* = 0$ for $Re = 300$ and $\Delta T = 10°$ C (up) and $\Delta T = 30°$ C (down).

The greatest difference is that the strong recirculation near the plate in the bottom channel is more concentrated for $\Delta T = 10°$ C ($y^* = [3.6, 4.4]$) while for $\Delta T = 30°$ C the structure in more extended ($y^* = [3.1, 4.5]$).

When considering $Re = 5.79 \times 10^3$ in the case where no temperature difference is introduced, the recirculation close to the plate in the bottom channel is more concentrated being located at $y^* = [3.3, 4.5]$, Fig. 6.11. As can be observed in Fig. 8.10, when considering the temperature differences the recirculation appears more widespread, but in the same region $y^* = [3, 4.5]$ for both temperature differences.

Practically the same structures were obtained for each Reynolds number of both experimental and numerically. The greatest difference is the passage channel recirculation that is not observed experimentally, however, numerically this recirculation is present for all Reynolds numbers studied. Figure 8.11 shows the numerical mean velocity field and the streamlines for $Re = 5.79 \times 10^3$

86

Figure 8.9: Experimental mean velocity field streamlines and modulus (mm/s) throughout the cavity, plane (y^*, z^*) at $x^* = 0$ for $Re = 1.16 \times 10^3$ and ΔT= 10° C (up) and ΔT=30° C (down).

Figure 8.10: Experimental mean velocity field streamlines and modulus (mm/s) throughout the cavity, plane (y^*, z^*) at $x^* = 0$ for $Re = 5.79 \times 10^3$ and ΔT= 10° C (up) and ΔT=30° C (down).
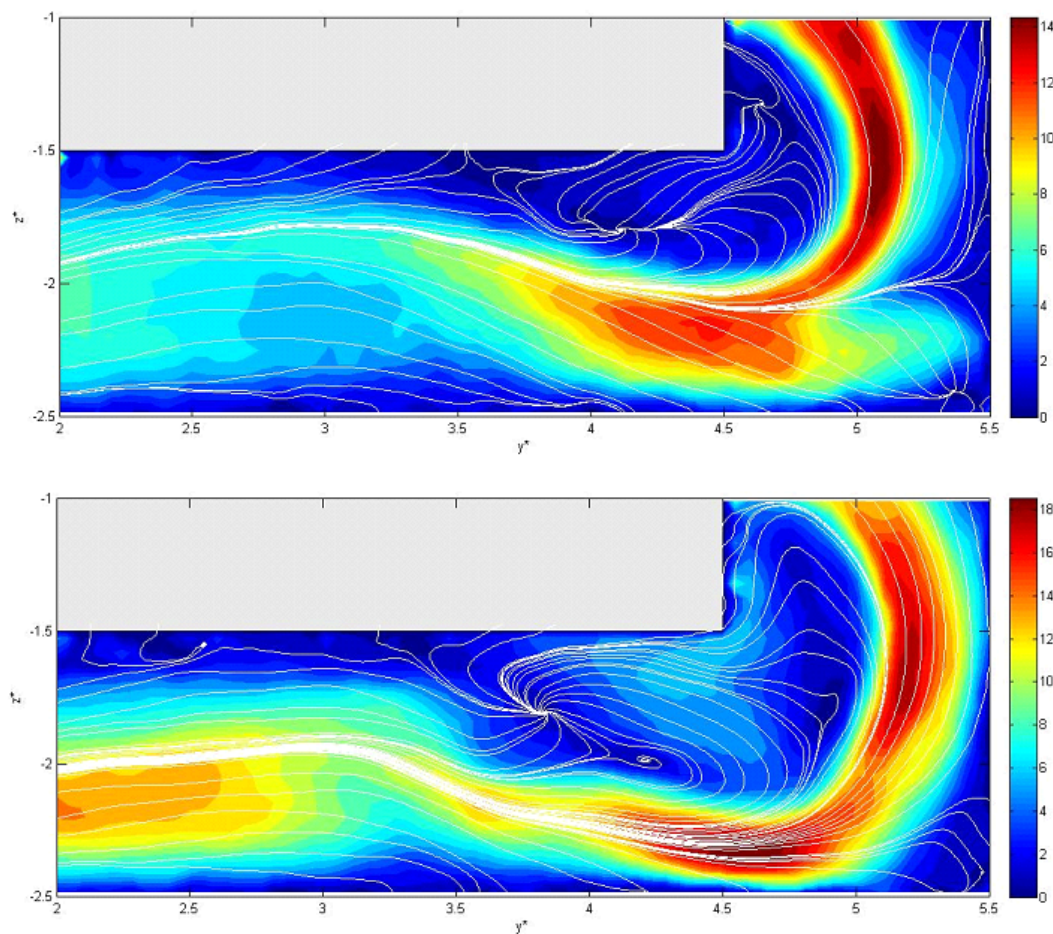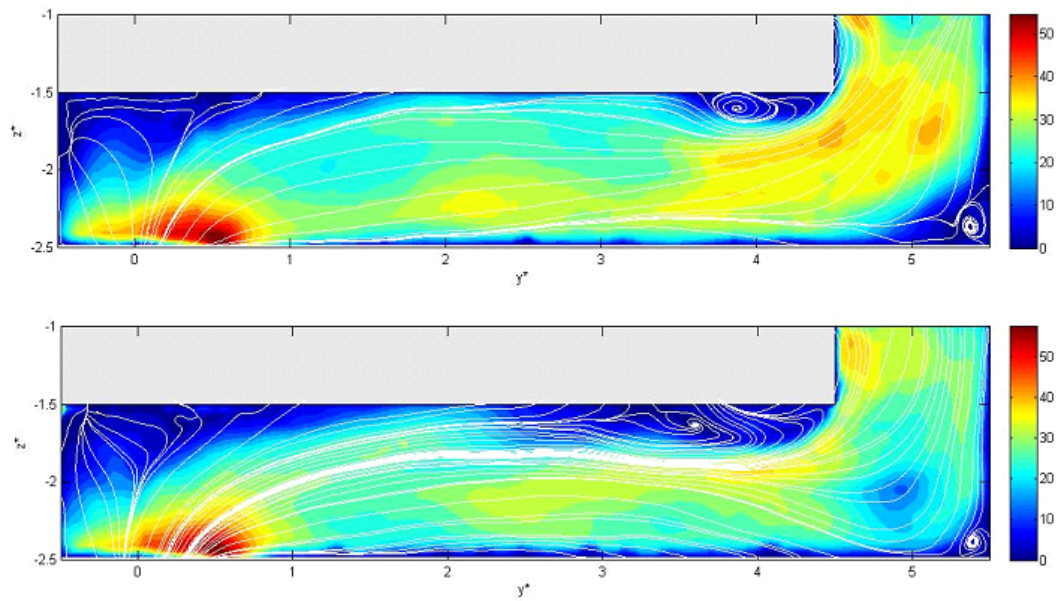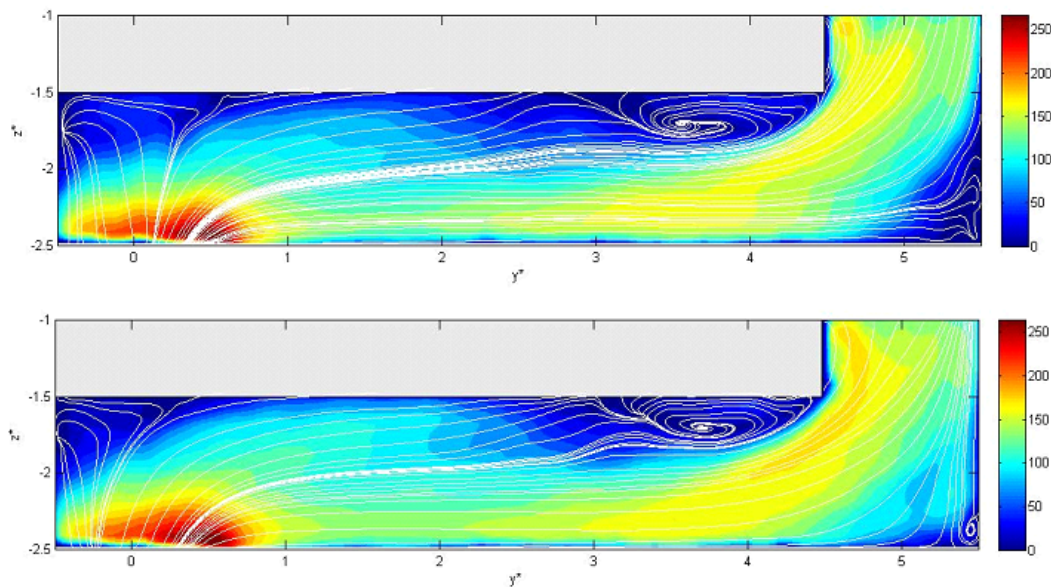
87
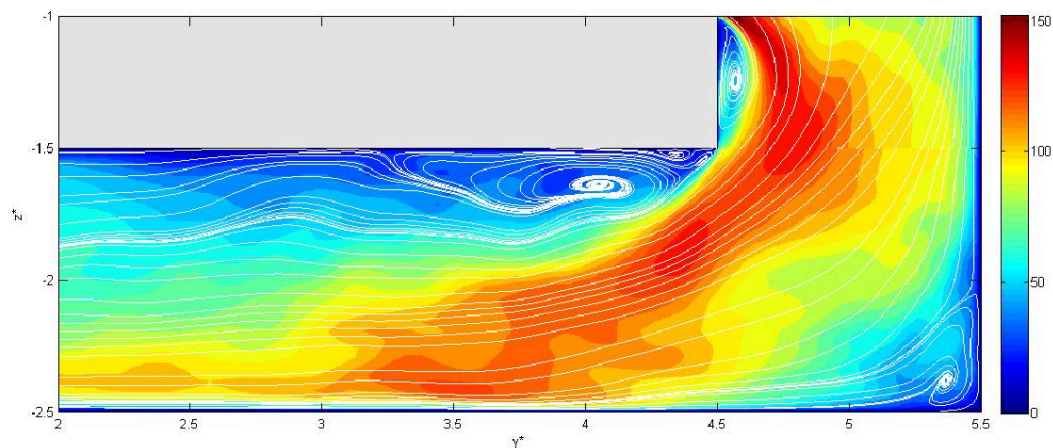
Figure 8.11: Numerical mean velocity field streamlines and modulus (mm/s) throughout the cavity, plane (y^*, z^*) at $x^* = 0$ for $Re = 5.79 \times 10^3$ and $\Delta T = 10°$ C.

and $\Delta T = 10$ ° C where the structures mentioned above can be observed. For this case also found two small recirculations in the bottom channel close to the edge of the plate, whose centers are located at $(y^*, z^*) = (4.34, -1.52)$ and $(y^*, z^*) = (4.448, -1.54)$. All recirculations can lower the heat transfer in those regions and they have to be avoided to prevent undesired localized mechanical wear.

8.1.2 Closed geometry

Figure 8.12 shows the numerical mean velocity field in the top channel at selected (x^*, z^*) planes at $Re = 5.79 \times 10^3$ and $\Delta T = 10°$ C for the closed geometry. The vector representation corresponds to the components u and w while the v component is represented by contours. As expected the flow behavior in the top channel is practically the same as for the open geometry (Fig. 8.1). Differences occur at $y^* = 5$, where the influence of the opening is important. Upstream of this location the large scale structures obtained are almost the same and the structures are located in the same place.

Some differences in flow structures are found in the passage channel for the $Re = 1.16 \times 10^3$ respect to the results obtained when no temperature difference is seen between the plate and the fluid. Figure 8.13 show the mean velocity field in the plane (x^*, y^*) for different values of z^*.

Considering $\Delta T = 10°$ C, in the passage channel entry $(z^* = -1)$ can be observed that the stagnation point moves towards the center of the channel $(x^*, y^*) = (0, 5)$. The w component distribution continues to be symmetric but is more homogeneous than the results observed in Fig. 7.5a.

At half height of the passage channel $(z^* = -1.25)$ the pair of small vor-

88
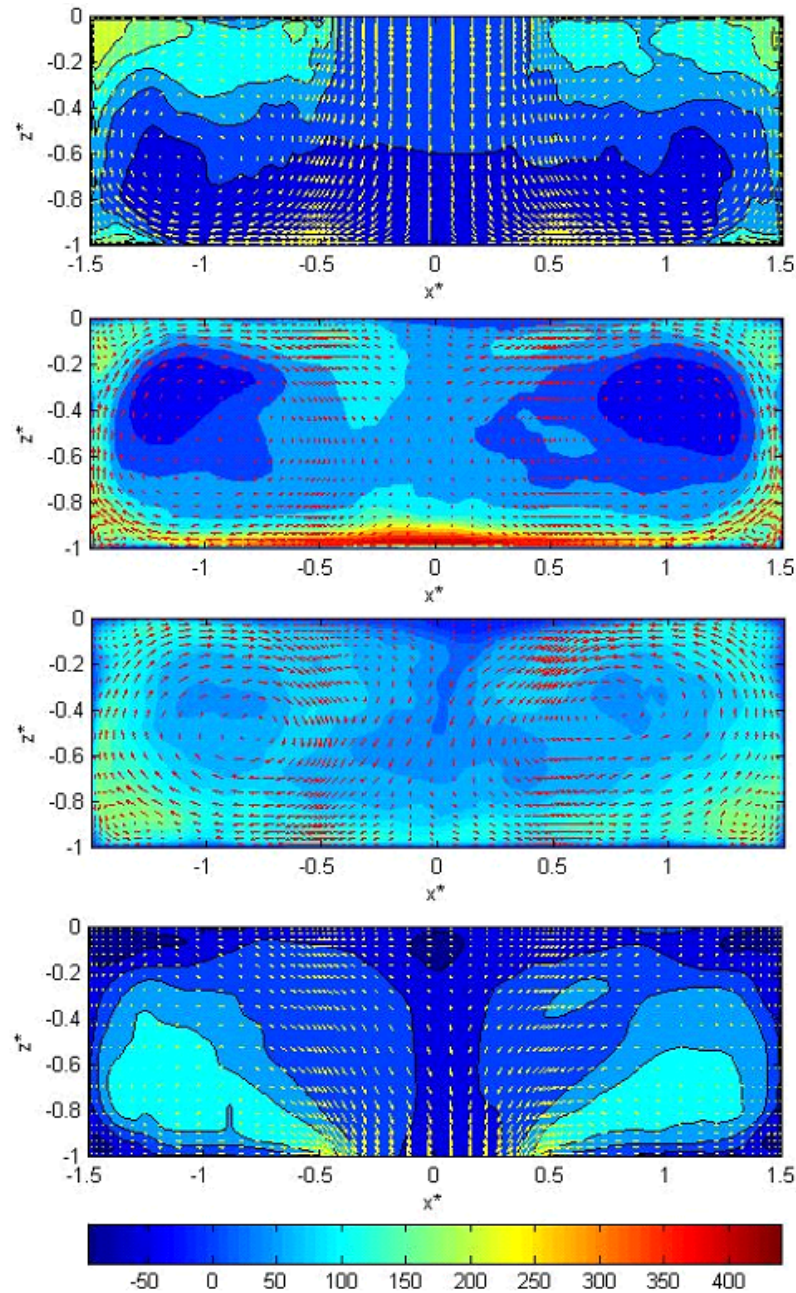
Figure 8.12: $Re = 5.79 \times 10^3$ and ΔT= 10° C at plane (x^*, z^*) in the top channel of PCB model. Numerical mean velocity field for (up to down) $y^* = 0$, $y^* = 1.5$, $y^* = 3.5$ and $y^* = 5$. Vectors u and w component, contours v component.

tices that appears in the corners are still present but are closer to the center of the passage channel at $(x^*, y^*) = (-0.28, 5.45)$ and $(x^*, y^*) = (0.28, 5.45)$. A pair of counter rotating vortices with centers in $(x^*, y^*) = (-0.12, 5.07)$ and $(x^*, y^*) = (0.12, 5.09)$ appear. Close to the plate the velocity component w
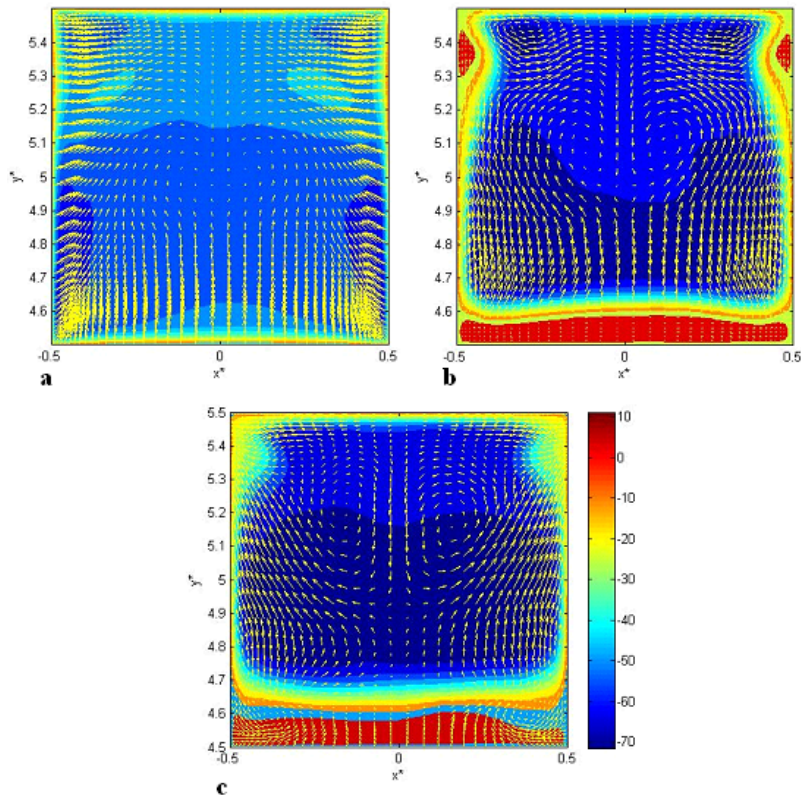
Figure 8.13: $Re = 1.16 \times 10^3$ and $\Delta T= 10°$ C at plane (x^*, y^*) in the passage channel of PCB model, closed geometry. Numerical mean velocity field (mm/s) for **a** $z^* = -1$, **b** $z^* = -1.25$ and **c** $z^* = -1.5$. Vectors u and v component, contours w component.

has a sign change implying that recirculation occurs as in the case considered previously, Fig. 7.5**b**. The two small symmetric recirculations on the side walls of the passage channel are placed a little closer to the wall of the cavity in the region $y^* = [5.25, 5.38]$, Fig. 8.13**b**. At the end of the passage channel ($z^* = -1.5$) the upper corner vortices disappear although a pair of vortices appears at the bottom corners, $(x^*, y^*) = (-0.38, 4.6)$ and $(x^*, y^*) = (-0.37, 4.6)$. The pair of quasi symmetric counter rotating vortices present in the central zone of the passage channel ($z = -1.25$) are more defined when arrive to the end of the channel ($z^* = -1.5$), maintaining its shape and being located somewhat closer to the wall of the cavity. In this plane is important to note that the recirculation zone (positive sign of the component w) near the plate occupies the entire width of the channel homogeneously. While in the case where no temperature difference is considered, this recirculation is more localized in the center of the entrance, see Fig. 8.13**c**. In the bottom channel the most relevant case to analyze is when $Re = 300$ and $\Delta T= 10°$ C are chosen. as we have seen in Fig. 8.4 structures along the top channel are different from those obtained

90
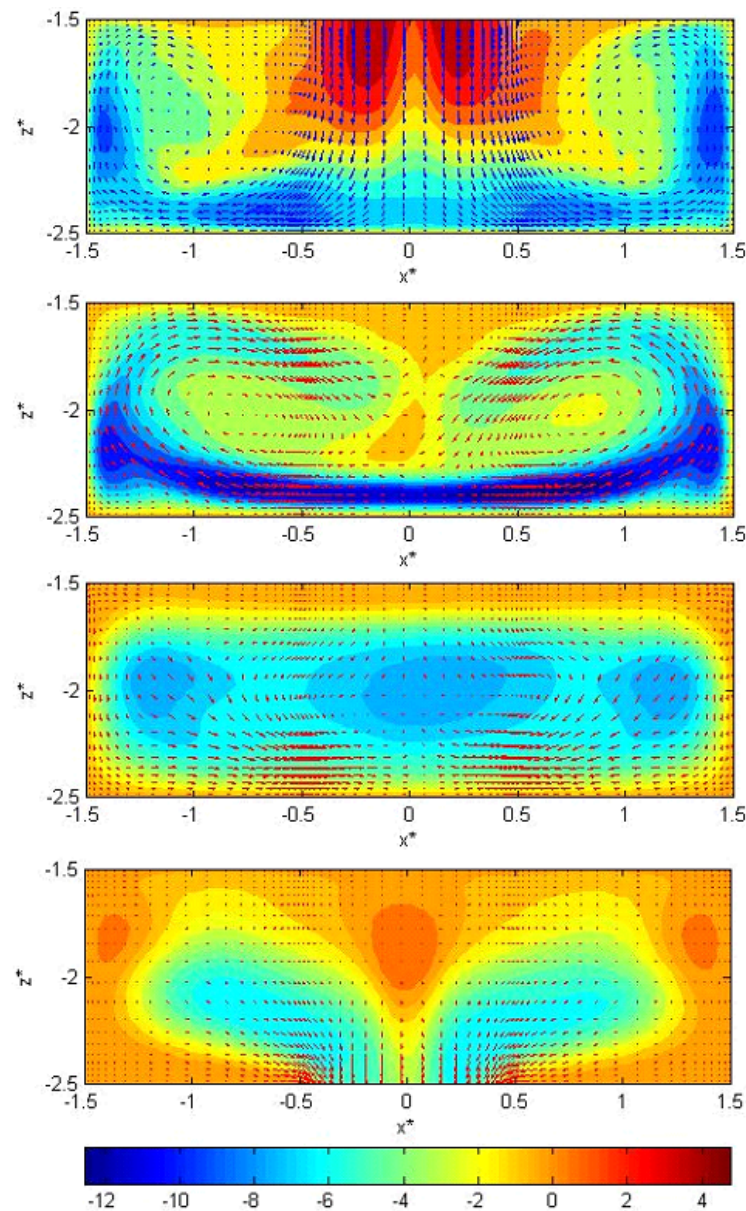
Figure 8.14: $Re = 300$ at plane (x^*, z^*) in the bottom channel of PCB model. Numerical mean velocity field for (up to down) $y^* = 5$, $y^* = 3.5$, $y^* = 1.5$ and $y^* = 0$. Vectors u and w component, contours v component.

for other Re. Figure 8.14 shows the numerical mean velocity patterns at the bottom channel for $Re = 300$ and $\Delta T = 10°$ C. The vector representation corresponds to the components u and w while the v component is represented by contours as in the top channel description. The flow contraction at the passage channel results in a jet impinging onto the bottom channel lower surface that leads to the creation of two new large counter rotating vortices as it can se in

the plane $y^* = 5$, Fig. 8.14. For other choices of Re and ΔT these counter rotating vortices are maintained throughout the bottom channel, but in this case can be seen that are present in the plane $y^* = 3.5$ and disappeared from the plane $y^* = 1.5$. Thereby obtaining the same behavior observed in the top channel.

Another way to visualize the flow behavior is plotting 3D streamlines. When no temperature difference was seen in the system, in the bottom channel could be observed that the fluid follows a quasi symmetric double spiral path (Fig. 7.1**b**) whereas in Fig. 8.15 shows that the double spiral path is present only up to about $y^* = 2$ and then transformed into straight lines similar to those obtained to the open geometry (Fig. 6.1**b**).
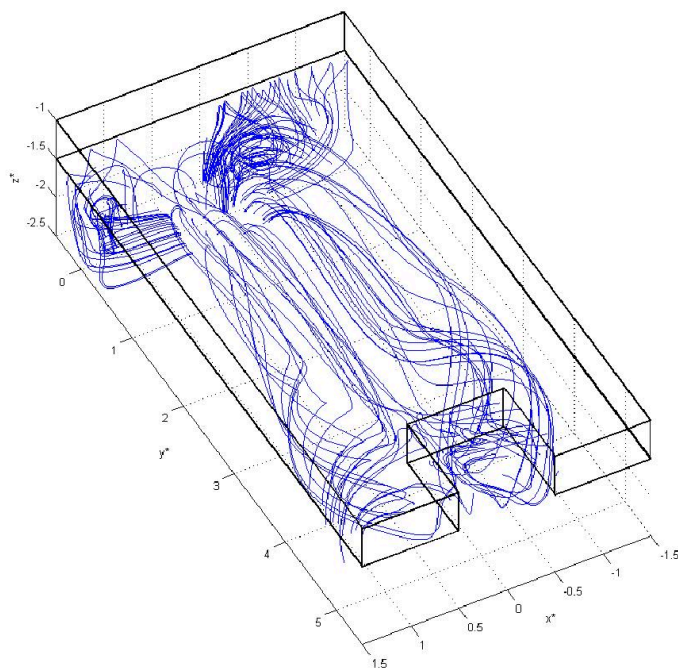
Figure 8.15: 3D streamlines, Re=300, bottom channel, closed geometry.

8.2   Temperature fields

In this section the mean temperature field in the case where the temperature difference between the plate and the fluid is $\Delta T = 10°$ C is discussed. Figure 8.16 shows the temperature contours in the open geometry for $Re = 1.16 \times 10^3$ where can be seen that in the top channel the fluid is scarcely influenced by the plate temperature except at very close distances to it.
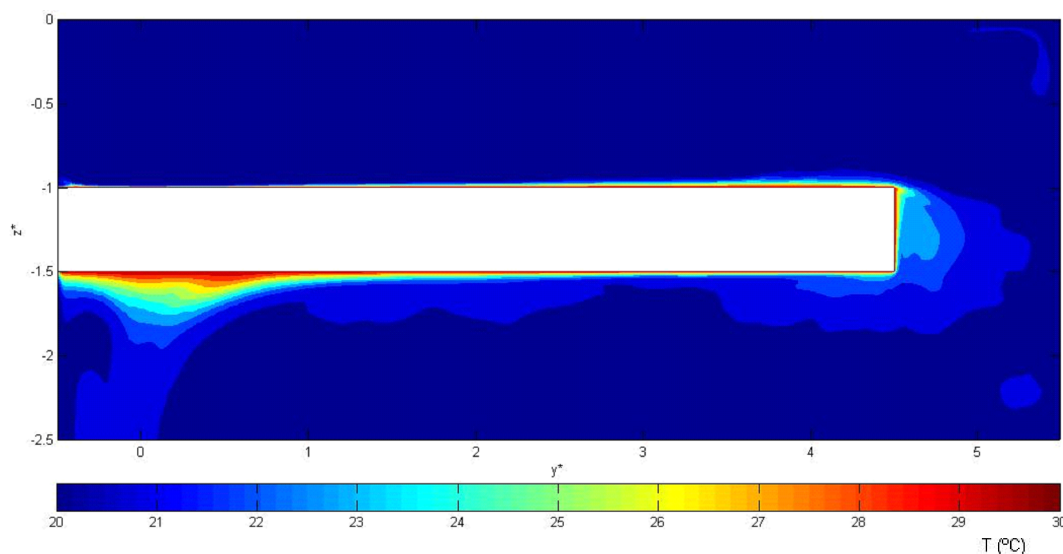
Figure 8.16: Mean temperature contours in plane (y^*, z^*) at $x^* = 0$, $Re = 1.16 \times 10^3$ and $\Delta T = 10°$ C.

Both in the passage and bottom channel the fluid is more influenced by the temperature of the plate, but this influence only represents a fluid temperature rise in $1°$ C in areas not close to the plate. This behavior is similar for different Re, having more fluid whose temperature rises at least $1°$ C for $Re = 300$ and less fluid for $Re = 5.79 \times 10^3$ but these variations are not really significant at the global level.

The greatest influence of the plate temperature in the fluid is presented very close to it so mean temperature fields in the plane (x^*, y^*) at the cell points in the z^* direction nearest to the plate are studied. These planes are located at $h/65$ of the plate, both in the top and the bottom channel (see Fig. 8.17).

The following sections will study the mean temperature fields in both geometries in top and bottom channels.

8. TEMPERATURE INFLUENCE IN THE SYSTEM
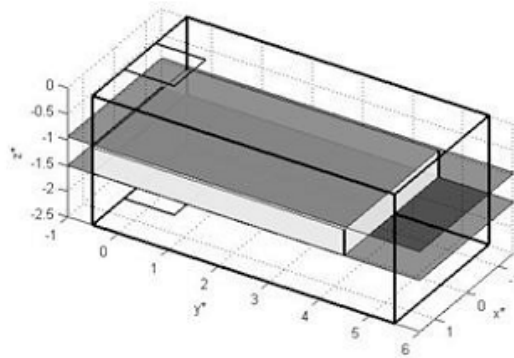
Figure 8.17: Location of relevant planes, three dimensional representation of (x^*, y^*) planes.

8.2.1 Top channel

Figure 8.18 shows the temperature contours in the upper part of the plate for open geometry for $Re = 300$, $Re = 1.16 \times 10^3$ and $Re = 5.79 \times 10^3$.

Figure 8.18: Mean temperature filed, open geometry. Plane (x^*, y^*) for $Re = 300$ (left), $Re = 1.16 \times 10^3$ (middle) and $Re = 5.79 \times 10^3$ (right) with temperature difference between the plate and the fluid of $\Delta T = 10°$ C.

For the all considered Reynolds numbers, the lower temperature zone coincides with the entrance area of the fluid in the cavity having a difference in temperature values for each Re.

94

For $Re = 300$, the fluid temperature is practically the same as the plate along the entire cavity having a little variation in the proximity of the passage channel. For $Re = 1.16 \times 10^3$ and $Re = 5.79 \times 10^3$ the areas with a higher temperature change match the location of the larger counter-rotating vortices (Fig. 6.1).

Figure 8.19: Mean temperature filed, closed geometry. Plane (x^*, y^*) for $Re = 300$ (left), $Re = 1.16 \times 10^3$ (middle) and $Re = 5.79 \times 10^3$ (right) with temperature difference between the plate and the fluid of $\Delta T = 10°$ C.

For the closed geometry, with the same setting described above, the mean temperature field is the same that obtained for the open geometry at least until the passage channel as Fig. 8.19 shows.

It could be seen that the heat transfer between the fluid and the plate is relative equivalent for both geometries for the selected Re.

8.2.2   Bottom channel

The biggest differences in the mean temperature distribution appear in the bottom side of the plate for both geometries.

The small, weaker, vortical structures present in the open geometry result in a higher values of temperature field along the channel (Fig. 8.20). For this geometrical configuration for $Re = 5.79 \times 10^3$ a hot region located near the passage channel at $y^* = 4.2$ is detected, matching with the recirculation region observed in Fig. 6.11. Moreover, a higher temperature spot near the output

region ($y^* = 0.6$) is observed. These hot spots increase the PCB's warming problems and therefore could reduce their efficiency and lifespan.
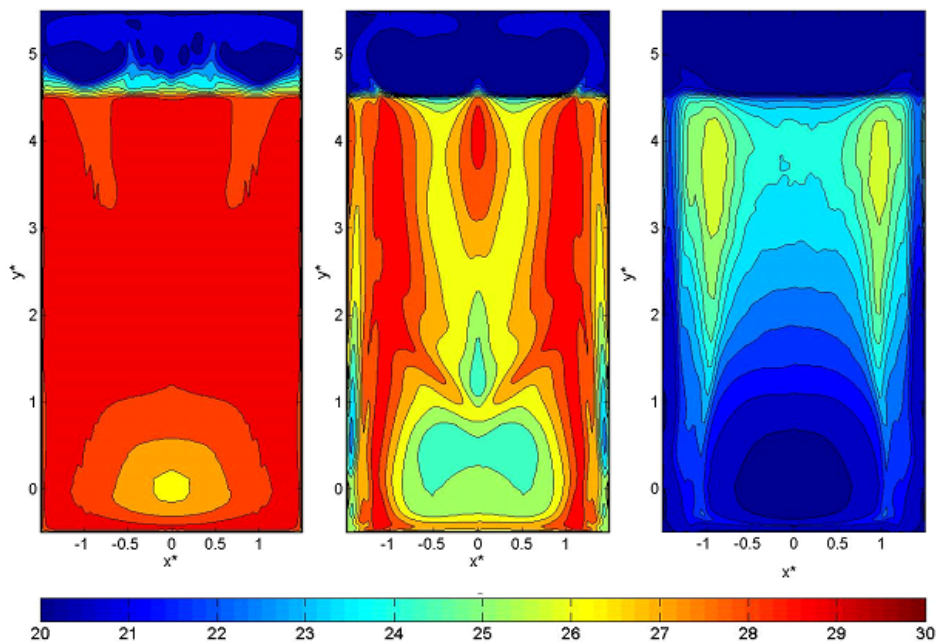

Figure 8.20: Mean temperature filed, open geometry. Plane (x^*, y^*) for $Re = 300$ (left), $Re = 1.16 \times 10^3$ (middle) and $Re = 5.79 \times 10^3$ (right) with temperature difference between the plate and the fluid of $\Delta T = 10°$ C.

For the closed geometry two large vortices (Fig. 7.1 and 7.7) are generated by the jet impinging onto the bottom channel, that has a lower temperature ($T_c = 20°$ C). These flow structures in the bottom channel are responsible for the decreasing of the temperature in some regions of the lower side of the plate (Fig. 8.21). For $Re = 1.16 \times 10^3$ and $Re = 5.79 \times 10^3$ the lower temperature coincides with the vortices location (about $x^* = \pm 1.25$) while the higher temperatures are located in the channel output zone ($y^* = 0.5$). As found for the open geometry, for $Re = 5.79 \times 10^3$ a higher temperature spot near the output region ($y^* = 0.6$) is observed though less localized.

From the temperature contours plotted in Fig. 8.20 and Fig. 8.21 it can be stated that the cooling of the PCB is more efficient for the closed geometry.

For both geometries the top channel shows a similar behavior, but for the bottom channel the open geometry depicts hot spots that could generate problems on the PCB´s operation.
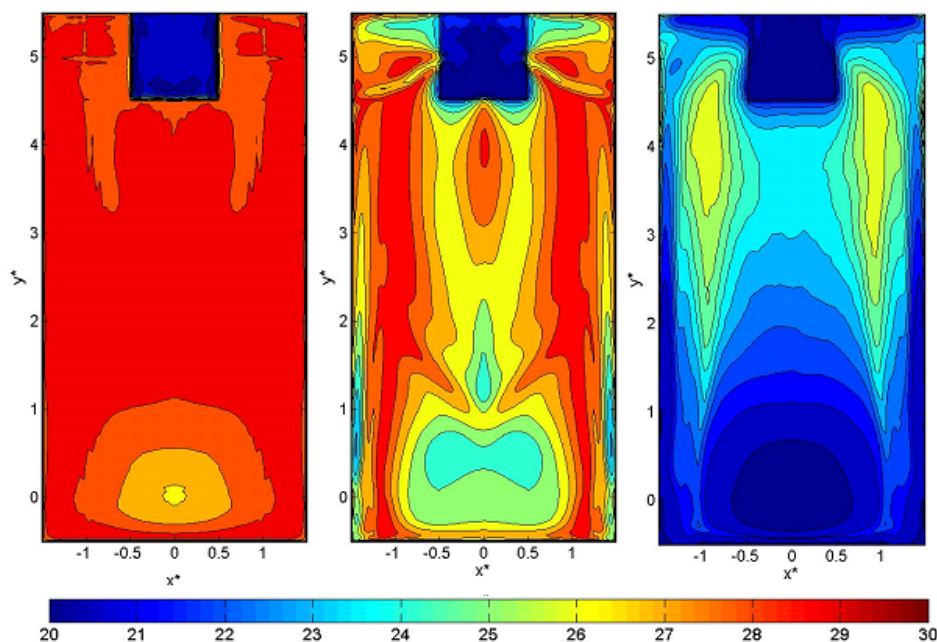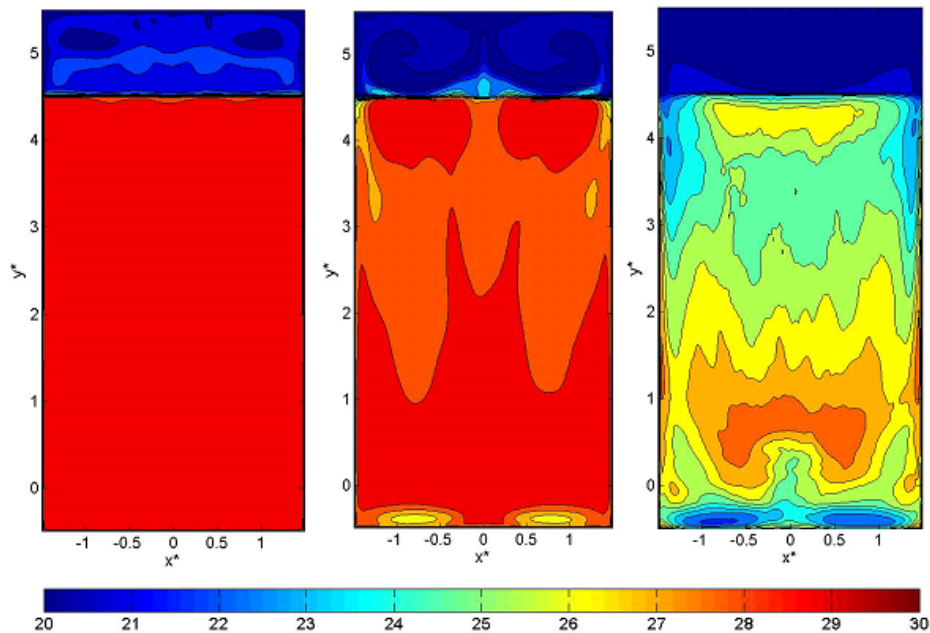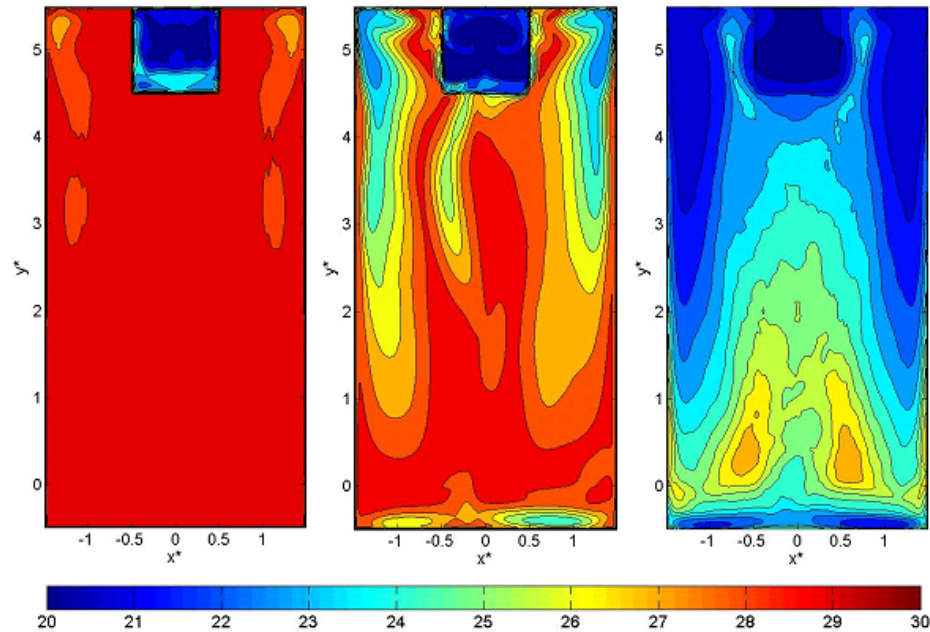
Figure 8.21: Mean temperature filed, closed geometry. Plane (x^*, y^*) for $Re = 300$ (left), $Re = 1.16 \times 10^3$ (middle) and $Re = 5.79 \times 10^3$ (right) with temperature difference between the plate and the fluid of $\Delta T = 10°$ C.

8.3 Heat transfer

8.3.1 Nusselt vs. Reynolds

The Nusselt number (defined in section 4.4) is one of the most important parameter in convective heat transfer problems. Convection intensity is determined by the value of Nusselt number. The mean Nusselt number of plate is calculated in order to realize the heat transfer phenomenon around the heat source. The Nusselt number values are obtained, as the temperature fields, in the plane (x^*, y^*) parallel to the plate at $h/65$ of this, both in the top and the bottom channel.

In this section we study the variation of mean Nusselt number (Nu) as a function of Reynolds number for both geometries. In all cases numerical results are presented, considering constant physical properties and the temperature difference between the plate and the fluid of $\Delta T = 10$ ° C. The mean Nusselt number is calculated through the averaging in two directions (x^* and y^*).In the closed geometry the area used to obtain such mean value is 13% higher than in the open geometry.
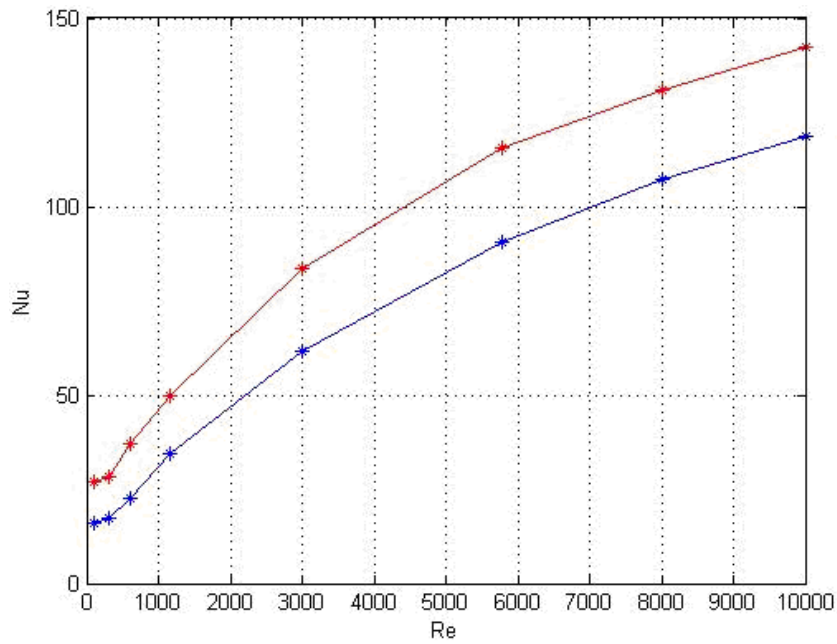
Figure 8.22: Mean Nusselt number vs. Re for the closed geometry with $\Delta T = 10°$ C in top (red) and bottom (blue) channel.
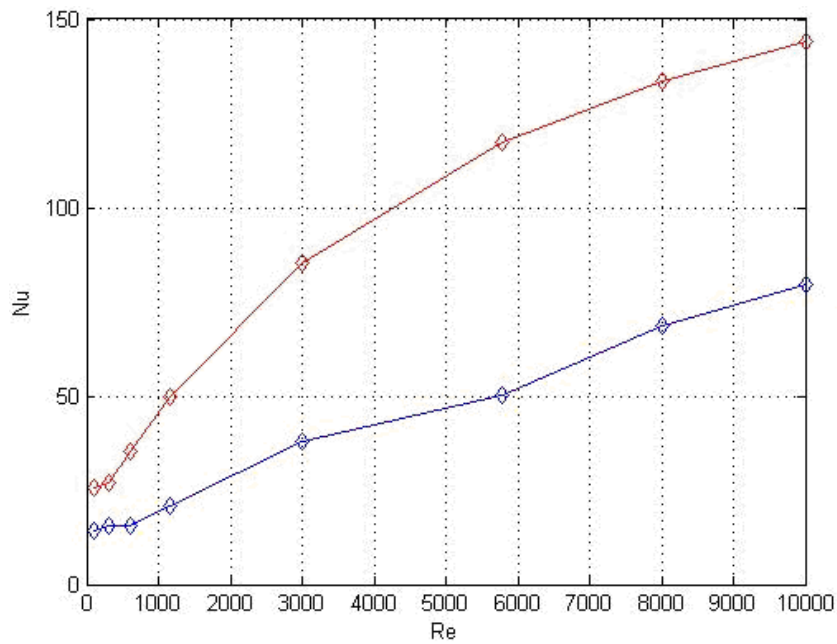
Figure 8.23: Mean Nusselt number vs. Re for the open geometry with $\Delta T = 10°$ C in top (red) and bottom (blue) channel.

98

Figure 8.22 shows the behavior of Nu as function of Re in the closed geometry, both in the top and the bottom channel. Where it can be seen that the heat transfer (Nu) is greater in the top channel than that in the bottom one, for all Re studied. Also having the same behavior. As observed for the closed geometry, heat transfer in the open geometry is greater in the top channel at the bottom. Although in this geometry the difference between the two channels is much greater as Fig. 8.23 shows.

Figure 8.24 shows the behavior of Nu as function of Re in the top channel for both geometries. For low Re the heat transfer into the top channel is 5% higher in the closed geometry than in the open one, for $Re = 1160$ the heat transfer is the same for both geometries while to higher Re, the heat transfer is 2% higher in the open geometry than in the closed one. In the bottom
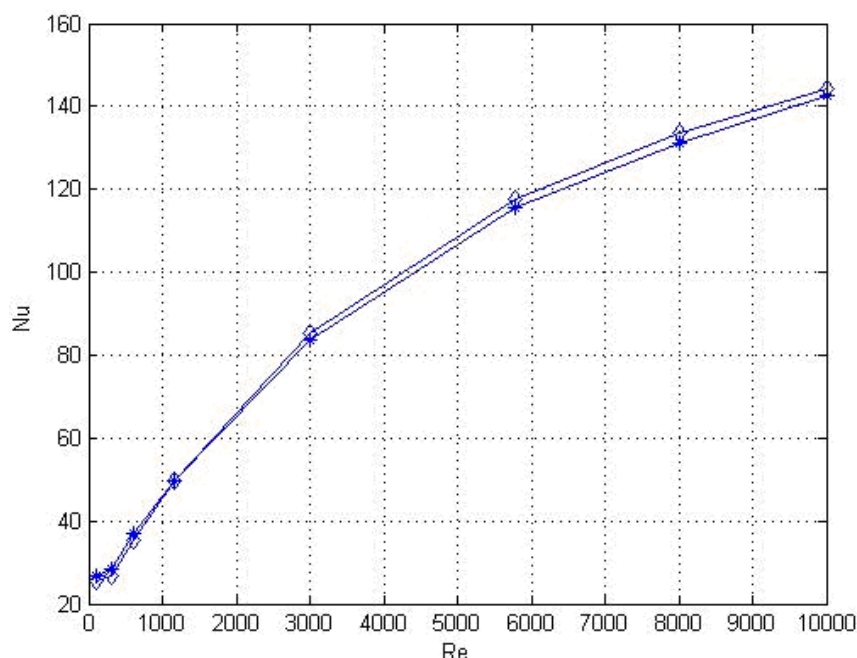
Figure 8.24: Mean Nusselt number vs. Re in the top channel of PCB model with $\Delta T = 10°$ C for closed (stars) and open (diamonds) geometries.

channel, for all values of Re the heat transfer is larger for the closed geometry than for the open one, which is was expected from the results presented in Figs. 8.20 and 8.21. Being these differnces higher by 10% for low values of Re up to 80% for higher Re ones, it can be seen in Fig. 8.23.

8. TEMPERATURE INFLUENCE IN THE SYSTEM
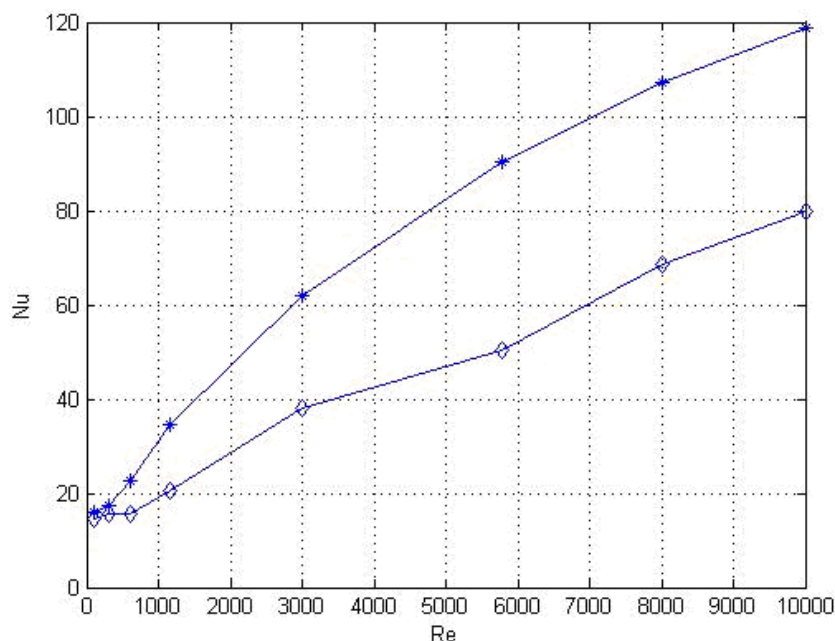
Figure 8.25: Mean Nusselt number vs. Re in the bottom channel of PCB model with $\Delta T = 10°$ C for closed (stars) and open (diamonds) geometries.

8.3.2 Nusselt vs. y*

In this section the behavior of mean Nusselt number as function of y^* position for different Reynolds numbers in the region of $-0.5 \geqq y^* \geqq 4.5$ will be analyzed, Fig. 8.28. In this region the behavior of Nu in the top channel is the same for both geometries. The mean Nusselt number is calculated through the averaging in the x^* direction.

In the top channel, both in closed and open geometry there is a strong Nu fluctuation in the region that matches the input channel at y* = [-0.5,0.5]. It should be noted that the Nu value in the rear wall of the cavity ($y* = -0.5$) is the same for all Reynolds numbers ($Nu = 200$) because the wall temperature is set at $T_c = T_{ref} = 20°$ C (boundary condition), independent of the inlet velocity. What it depends on the Re is the range of mean Nusselt number values, being higher the greater the Re. The aforementioned fluctuation has at least a sharp minimum followed by a maximum and coincides with the jet impinging onto the plate produced when the fluid enters to the cavity. From the maximum the Nu values decreases until $y^* = 4$ to increases near the passage channel ($y^* = 4.5$), this behavior is verified for Re greater than $Re = 1160$. For $Re = 100$, 300 and 600 the behavior described above is only maintained until $y^* = 1$.

For $Re = 100$, from $y^* = 1$, we see that the heat transfer increases to remain practically constant, with values higher than those obtained for $Re = 300$ for

100

Figure 8.26: Mean Nusselt number vs. y^* in the top channel for the closed geometry with $\Delta T = 10°$ C for $Re = 100$ (blue), $Re = 300$ (red), $Re = 600$ (magenta), $Re = 1160$ (cyan), $Re = 3000$ (green), $Re = 5790$ (black), $Re = 8000$ (blue, dash line), $Re = 10000$ (red).
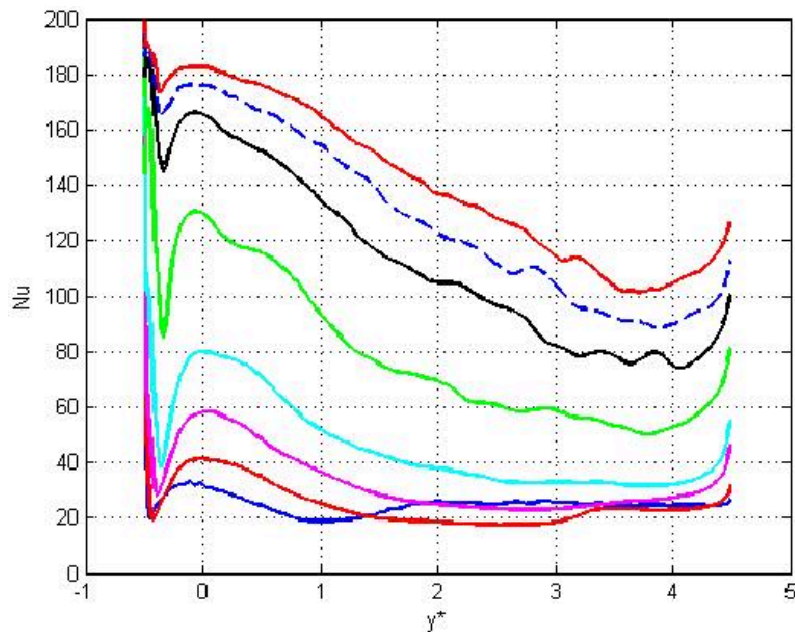
$1.4 \geqq y^* \geqq 4.5$ and higher than those obtained for $Re = 600$ in $1.86 \geqq y^* \geqq 3.31$.

Unlike what happens in the top channel, in the bottom channel are seen remarkable difference in the behavior of the Nusselt number between the geometrical configurations studied as Figs. 8.28 and 8.28 show. In the closed geometry can be seen that at y = 4.5 presents the maximum values of the Nusselt number to decrease until reach the area of the channel output $y^* = 0.5$. The decrease rate depends on Re, being greater for higher Reynolds numbers. This behavior is consistent with the temperature fields shown in Fig. 8.21.

For low Re $(100, 300 and 600)$ shows that from $y^* = 1$ different mean Nu converge to the same value $(Nu = 12)$ and in $y^* = -0.5$ presents a great growth because the wall boundary condition, as in the top channel. For $Re \geq 1160$ in the region $-0.5 \geqq y^* \geqq 0$ presents a fluctuation similar to that observed in the top channel, although it is even more sharp minimum and maximum is narrower. In the open geometry, the region $4 \geq y^* \geq 4.5$ shows a minimum for the Re greater than 1160. This minimum coincides with the recirculation zone seen in Fig. 6.12. Furthermore the Nu values at $y^* = 4.5$ are lower than those observed in the closed geometry. In region $1 \geqq y^* \geqq 4$ the mean Nu decreases and $1 \geqq y^* \geqq 0$ there is a new minimum sharper of the higher Re. This minimum coincides with the hot zone seen in Fig. 8.20. The behavior at $-0.5 \geqq y^* \geqq 1$ is similar to that obtained for the closed geometry.

8. TEMPERATURE INFLUENCE IN THE SYSTEM

Figure 8.27: Mean Nusselt number vs. y^* in the bottom channel for the closed geometry with $\Delta T = 10°$ C for $Re = 100$ (blue), $Re = 300$ (red), $Re = 600$ (magenta), $Re = 1160$ (cyan), $Re = 3000$ (green), $Re = 5790$ (black), $Re = 8000$ (blue, dash line), $Re = 10000$ (red).
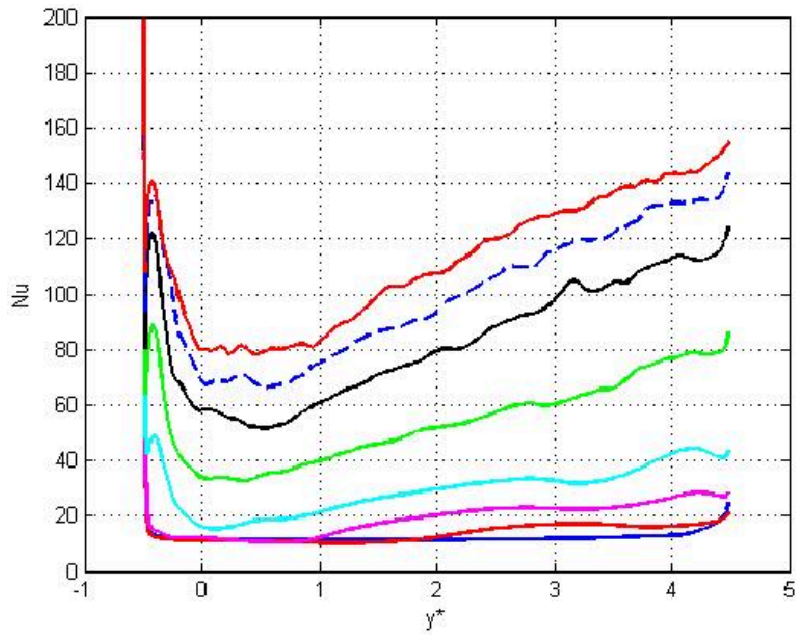

Figure 8.28: Mean Nusselt number vs. y^* in the top channel for the open geometry with $\Delta T = 10°$ C for $Re = 100$ (blue), $Re = 300$ (red), $Re = 600$ (magenta), $Re = 1160$ (cyan), $Re = 3000$ (green), $Re = 5790$ (black), $Re = 8000$ (blue, dash line), $Re = 10000$ (red).
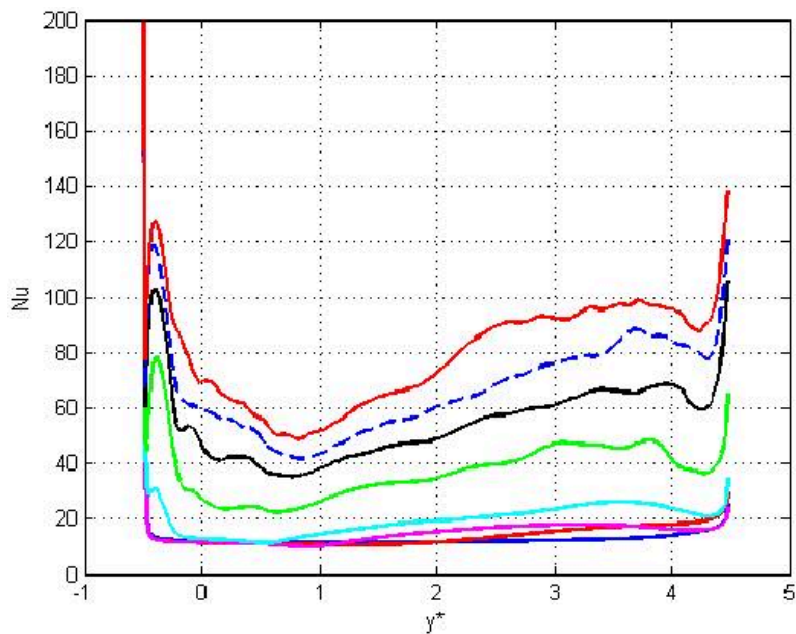
102

Chapter 9

Conclusions

The flow within a simplified model of a printed circuit board enclosure has been analyzed experimentally and numerically. The LFC-PIV technique has been used to obtain the velocity fields from the recorded instantaneous images. In addition, an experimental technique that allows the measurement of two simultaneous velocity planes has been designed and implemented. The numerical simulation has been done using the caffa3d software. This allows obtaining instantaneous $3D$ information of dynamic field in the PCB model. Two geometrical configurations of the PCB plate have been analyzed for different inlet velocity cases. Numerical and experimental results have been compared finding the similar flow structures at the same locations. All the techniques implemented have been shown to be very useful in the analysis of the turbulent flows in complex domains.

The results obtained show that the flow structures present in the top channel are a pair of quasi-symmetric counter rotating vortices for both geometries. In the bottom channel the flow behavior depends on the geometry, for the closed one it remains the pair of quasi-symmetric counter rotating vortices while in the open geometry these structures disappear giving way to smaller ones.

Through the measurement of two simultaneous velocity planes can be seen, by the auto and cross correlations, that the pair of quasi-symmetric counter rotating vortices have periodicity which is maintained in time.

The flow behavior is also sensitive to the Re, meaning that it depends on the inlet fluid velocity. Although for both geometries the large vortex structures in the top channel are not very concerned.

The existence of a recirculation region beneath the plate at the entrance of the bottom channel obtained previously [1] for the open geometry was verified. It has been stated that this flow recirculation changes with Re. It has been clearly established that it exits for $Re = 1160$, but there is not any evidence that it exist at lower Re numbers.

This structure also has the influence of the geometry, since it is present

103

only in the open geometry and is of great importance as it has associated a hot spot in the plate that could increase the warming problems and a reduction of the PCB's efficiency and lifespan.

A small recirculation is observed in the passage channel near the plate, this recirculation is observed for all Re in both geometries when the temperature difference between the plate and the fluid is not considered. For temperature differences of $\Delta T = 10°$ C and $\Delta T = 30°$ C, the recirculation in passage channel is only present for high Re.

The temperature fields in both geometries show the influence on the choice of Re. In the top channel, the mean temperature field is the same for both geometries at least until the passage channel for all Re studied. In the bottom channel, for the closed geometry, the presented flow structures are responsible for the decreasing of the temperature in some regions of the lower side of the plate. The lower temperature coincides with the vortices location while the higher temperatures are located in the channel output zone. While in the open geometry the small, weaker, vortical structures presented result in a higher values of temperature field along the channel.

The heat transfer between the PCB and the fluid has been studied by means of the computation of the Nu number. The behavior of the mean Nusselt numbers as function of y^* position for different Re is the same for both geometries in the top channel. In the bottom channel this behavior is different depending on the geometry and the variations are consistent with the flow structures present in each case.

The greater heat transfer is obtained in the top channel for both geometries. In turn in the bottom channel the heat transfer is greater (up to 80% more) in the closed geometry than in the open one.

The results obtained indicate that the cooling of the PCB is more efficient for the closed geometry. Small changes in the PCB geometry modify the velocity flow field allowing the formation of new vortical structures in the bottom channel of the PCB that enhance the heat transfer between the fluid and the plate

During the work it has also been stat the important of considering fluid physical properties in the numerical simulation when the ΔT is greater than $10°$ C.

Bibliography

[1] G. Usera, A. Vernet, J.A. Ferrè, Use of time resolved PIV for validating LES/DNS of the turbulent flow within a PCB enclosure model, Flow Turbulent Combust. 77 (2006) 77-95.

[2] F.P. Incropera, Convection heat transfer in electronic equipment cooling. Journal ofHeat Transfer, 110 (1988) 1097-1111.

[3] Y. Asako and M. Faghri, Parametric study of turbulent three-dimensional heat transfer of arrays of heated blocks encountered in electronic equipment. Int. J. Heat Mass Transfer, 37(3)(1994) 469-478.

[4] K. Fushinobu, K. Hijikata and Y. Kurosaki, Heat transfer regime mao for electronic devices cooling. Int. J. Heat Mass Transfer, 39(15) (1996) 3139-3145.

[5] B.A. Jubran, S.A. Swiety and M.A.Hamdan, Convective heat transfer and pressure drop characteristics of various array configurations to simulate the cooling of eleetronic modules. Int. J. Heat Mass Transfer, 39(16) (1996) 3519-3529.

[6] T.J. Heindel, S. Ramadhyani and F.P. Incropera, Conjugate natural convection from an array of discrete heat sources: part 1 - two and threedimensional model validation.Int. J. Heat and Fluid Flow, 16 (1995) 501-510.

[7] Chiang, J.S., Chuang, S.H., Wu, Y.K., Lee, H.J.: Numerical simulation of heat transfer in a desktop computer with heat-generating components. International Communications in Heat and Mass Transfer, 32 (2005) 184-191.

[8] Protocase Designer® v3.0 - Mounting PCB's tutorial. www.protocasedesigner.com

[9] J. Bigorra, F.J. Sanchez, I. Cuesta, J. Herrero, J. Giralt and F.X. Grau, ESTIMA: A thermal simulation software for the optimal design of printed circuit board in the automotive industry, Advanced Computational Methods in Heat Transfer VI, (2000).

BIBLIOGRAPHY

[10] Raffel M., Willert C., Kompenhans J., Particle Image Velocimetry. A Practical Guide, 3th edn., Springer, (1998).

[11] G. Usera, A. Vernet, J.A. Ferrè, A Parallel Block-Structured Finite Volume Method for Flows in Complex Geometry with Sliding Interfaces, Flow Turbulent Combust. 81 (2008) 471-495.

[12] Ferziger J. Pèric M, Computational methods for fluid dynamics, Springer-Verlag, (2002).

[13] T. Lehnhauser, M. Schafer, Improve linear interpolation pratice for finite-volume schemes on complex grids. Int. J. Numer. Methods Fluids 38 (2002) 625-645.

[14] PolyScience 6000 Series Chillers specifications http://www.polyscience.com/indust/14to1chill.html

[15] Derek Ford and Paul Willims, Karst Hydrogeology andd Geomorphology, John Wiley & Sons. (2007).

[16] Spandre R., Batisit G., Rosa Filho E. F., Hindi E.C., Giusti D. A., Empleo de esporas de Lycopodium clavatum como marcadores de aguas subterraneas en acuíferos karsicos, Revista Latino-Americana de Hidrogeologia **3**, 43-47 (2003).

[17] Adrian, R.J., Scattering particle characteristics and their effect on pulsed laser measurements of fluid flow: speckle velocimetry vs. particle image velocimetry, Appl. Optics **23**, (1984), 1690-91.

[18] Westerweel J., Digital Particle Image Velocimetry - Theory and Application, (Delft: Delft University Press),(1993a).

[19] Westerweel J., 'Optical diagnostics in fluid and thermal flow', SPIE *2005* 624-635 (1993b).

[20] Westerweel J., Fundamentals of digital particle image velocimetry, Meas. Sci. Technol. **8** 1379-1392 (1997).

[21] Westerweel J., Draad A.A., van der Hoeven,J.G.Th and van Oord J. Measurement of fully-developed turbulent pipe flow with digital particle image velocimetry, Exp. Fluids 20 165 (1996).

[22] Nogueira J., Lecuona A., Rodríguez P. A., Local field correction PIV : on the increase of accuracy of digital PIV systems. Experiments in fluids, 27, 107-116 (1999).

[23] Usera, G., Vernet, A., Ferré, J.A.,Considerations and improvements of the analysing algorithms used for time resolved PIV of wall bounded flows, 12th International Symposium on Applications of Laser Techniques to Fluid Mechanics (2004).

[24] Usera, G., Vernet, A., Ferré, J.A., Boundary treatment in PIV image analysis. Models, Experiments and Computation in Turbulence ©CIMNE, Barcelona, Spain (2004).

[25] Nogueira, J., Lecuona, A., Rodríguez, P.A., Local field correction PIV, implemented by means of simple algorithms and multigrid versions. Meas. Sci. Technol. 12, 1911-1921 (2001).

[26] Lobera, J., Andrés, N., Arroyo, M.P. and Quintanilla, M., Dual Holographic Interferometry for measuring the three velocity components in a fluid plane. Appl Opt; 43 17: 3535-3542 (2004).

[27] Cabeza, C., Sarasúa G., Martí, A., Bove, I., Varela, S., Usera, G., Vernet, A.:Influence of coaxial cylinders on the vortex breakdown in a closed flow, European Journal of Mechanics - B/Fluids, 29 (3) (2010) 201-207.

[28] Cabeza, C., Varela, J., Bove, I., Freire, D., Martí, A., Sarasúa L.G., Usera, G., Montagne, R., Araujo, M.: Two-layer stratified flows over pronounced obstacles at low-to-intermediate Froude numbers. Phys. Fluids, 21 (4) (2009) 102-112.

[29] U. Bückle, M. Pèric, Numerical simulation of buoyant and thermocapillary convection in a square cavity, Numerical Heat Transfer, Part A, vol. 21 (1992) 121-141.

[30] $http : //www.engineeringtoolbox.com/water - thermal - properties - d_162.html$

[31] G. Usera, Master Thesis, L.E.S. Simulación numérica de grandes vórtices Aplicación al flujo en torno a un cilindro cuadrado. Montevideo (2001).

[32] Born M., Wolf E., Principles of optics, 6th edn. Pergamon Press, Oxford, (1985).

[33] Kähler C. J., Kompenhans J.: Fundamentasl of multiple plane stereo particle image velocimetry, Experiments in Fluids vol. 29, Supplement 1, S070-S077 (2000).

[34] J.Jeong and F. Hussain, On the indentification of a vortex, J. Fluid Mech, 285, 69-94, (1995) .